The Numerical Investigation and Parametric Study of Cooling an Array of Heated Blocks by a Turbulent Air Jet in a Three-Dimensional Domain

by

Richard Lozowy

A Thesis submitted to the Faculty of Graduate Studies of

The University of Manitoba

in partial fulfilment of the requirements of the degree of

Master of Science

Department of Mechanical Engineering

University of Manitoba

Winnipeg

THE UNIVERSITY OF MANITOBA

FACULTY OF GRADUATE STUDIES
*****
COPYRIGHT PERMISSION

The Numerical Investigation and Parametric Study of Cooling an Array of Heated Blocks by a Turbulent Air Jet in a Three-Dimensional Domain

By

Richard Lozowy

A Thesis/Practicum submitted to the Faculty of Graduate Studies of The University of Manitoba in partial fulfillment of the requirement of the degree

Of

Master of Science

ACKNOWLEDGEMENTS

For funding:

- Natural Sciences and Engineering Research Council of Canada (NSERC)
- Manitoba Hydro

For Technical Support:

- Dr. Hassan Soliman and Dr. Scott Ormiston for giving me the opportunity to work on this project and for supporting me through the challenges that arose.
- Department of Mechanical and Manufacturing Engineering, University of Manitoba.
- Mr. Harkaran Jhinger for providing support during the project.
- The staff at Manitoba Hydro that took us on two tours of the Dorsey Converter Station.
- Dr. Ahmed El-Shaboury for assisting me in learning ANSYS CFX and other aspects of the project.
- Mark Levec, Gavin Joyce, Dean Ferley for giving me support in the lab.

For Life Support:

- My parents for giving me emotional and financial support during my education.
- Any other family members or friends that were there for me.

ABSTRACT

Manitoba Hydro generates approximately 5000 MW of power, out of which 3854 MW is transmitted through the Dorsey Converter Station to be converted from DC power to AC power. The conversion process takes place in valve halls that house DC/AC converter towers. A DC/AC converter tower consists of vertically stacked tiers of thyristor and reactor modules; there is a gap between each two tiers. The towers are supported above the ground on posts at two different elevations. A ventilation system is utilized to remove a portion of heat generated during the conversion process. Airflow from the ventilation system enters the valve hall through inlet grills located on the ground in front of the converter towers. The current ventilation system circulates enough airflow to remove all of the heat but elevated temperatures exist around the thyristor valves due to poor airflow circulation. The research presented in this thesis will numerically simulate the turbulent airflow and heat transfer in a valve hall for the two tower elevations. The commercial CFD code, ANSYS CFX-11 was used to generate a three-dimensional numerical model of the fluid flow and heat transfer around a DC/AC converter tower. The location of the inlet, the inlet size and aspect ratio, and the location on the tower that the airflow is aimed at were varied to improve the interaction between the ventilation system and the tower. It was determined that varying the above parameters can improve the cooling of a converter tower much beyond the ventilation design currently utilized by Manitoba Hydro. It was found that a different cooling strategy is required for each of the two tower elevations. A correlation was established between the amount of airflow entering the gap between two tiers and the maximum temperature within that gap. The results from this thesis demonstrate how careful consideration in the design of a ventilation system can improve the cooling of electrical components and the conclusions from this study can be valid for various industrial applications.

TABLE OF CONTENTS

LIST OF FIGURES

LIST OF TABLES

NOMENCLATURE

A	tower target location	m
$A_{s,g}$	gap surface area	m^2
C	wall roughness constant	
C_p	specific heat	$J\ kg^{-1}\ K^{-1}$
$C_{\varepsilon 1}$	k-ε turbulence model constant for the ε equation	
$C_{\varepsilon 2}$	k-ε turbulence model constant for the ε equation	
C_μ	k-ε turbulence model constant	
E	energy	J
F_{cal}	calibration factor used with scalable wall functions	
g	gravitational acceleration	$m\ s^{-2}$
Gr	Grashof number	
H_1	tower elevation above the ground	m
H_2	height of valve hall	m
I	turbulence intensity	
k	turbulence kinetic energy per unit mass	$m^2\ s^{-2}$
L_x	length of inlet in x-direction	m

L_y	length of inlet in y-direction	m
$\dot{m}$	mass flow rate	kg s^{-1}
n	normal distance from wall to first node	m
Nu	Nusselt number	
P_y	distance from symmetry plane S3 to the inlet centre in the y-direction	m
P	time averaged pressure	Pa
P_k	turbulence production due to viscous dissipation	kg m^{-1} s^{-3}
P^*	dynamic pressure	Pa
Pr	Prandtl number	
Pr_t	turbulent Prandtl number	
plcs	places	
q''	uniform heat flux	W m^{-2}
Q	quadrant	
R	viscosity ratio	
Ra	Rayleigh number	
Re	Reynolds number	
T	temperature	K

T_b	bulk temperature	K
u	time averaged velocity in the x-direction	m s^{-1}
u^*	velocity scale used with scalable wall function	m s^{-1}
u_τ	friction velocity	m s^{-1}
U_t	near wall tangential velocity	m s^{-1}
v	time averaged velocity in the y-direction	m s^{-1}
w	time averaged velocity in the z-direction	m s^{-1}
y^+	non-dimensional wall distance	
$\tilde{y}^+$	fixed non-dimensional wall distance	
Δy^+	non-dimensional distance from wall node to first interior node	
x, y, z	Cartesian coordinate system	m

Greek Symbols

β	dimensionless tower target location	
ε	turbulence dissipation rate	m^2 s^{-3}
ρ	density	kg m^{-3}
μ	dynamic viscosity	kg m^{-1} s^{-1}
μ_t	eddy viscosity	kg m^{-1} s^{-1}

λ	thermal conductivity	$W\ m^{-1}\ K^{-1}$
θ	jet inlet angle	deg
K	von-Karman constant	
σ_ε	turbulence model constant for the ε equation	
σ_k	turbulence model constant for the k equation	
τ_w	wall shear stress	$N\ m^{-2}$

Subscripts

av	average
g	gap
gen	generation
o	inlet
max	maximum
t	tower

Acronyms

AC	alternating current
CAD	computer aided design
DC	direct current

HVDC	high voltage direct current
VH	valve hall

CHAPTER 1: INTRODUCTION

1.1: Overview

Manitoba Hydro generates approximately 5000 MW of power, out of which 3854 MW is transmitted through the Dorsey Converter Station to be converted from direct current (DC) to alternating current (AC). A majority of the electricity producion in Manitoba is done at the Kettle, Long Spruce, and Limestone hydro generating stations, which are located on the Nelson River in northern Manitoba. The electricity generated at these sites is transported approximately 900 km to southern Manitoba. DC is used for long distance transmission because it offers the following advantages over AC:

- The transmission losses are significantly lower when the current is DC.
- The cost of a DC transmission system is lower than an equivalent AC transmission system.

In northern Manitoba, the AC power is converted to DC at the Radisson and Henday converter stations. These are located in the proximity of the hydro generating stations. The electric current is transmitted to the Dorsey converter station located in southern Manitoba by two high voltage direct current (HVDC) transmission lines: Bipole 1 and Bipole 2. At the Dorsey converter station the electricity is converted back to AC and is utilized in southern Manitoba, Saskatchewan, Ontario, and the United States (Manitoba Hydro, 2002). A map of Manitoba showing the route of the HVDC transmission lines and the relevant Manitoba Hydro sites is shown in Figure 1-1. An aerial view of Dorsey converter station is shown in Figure 1-2.

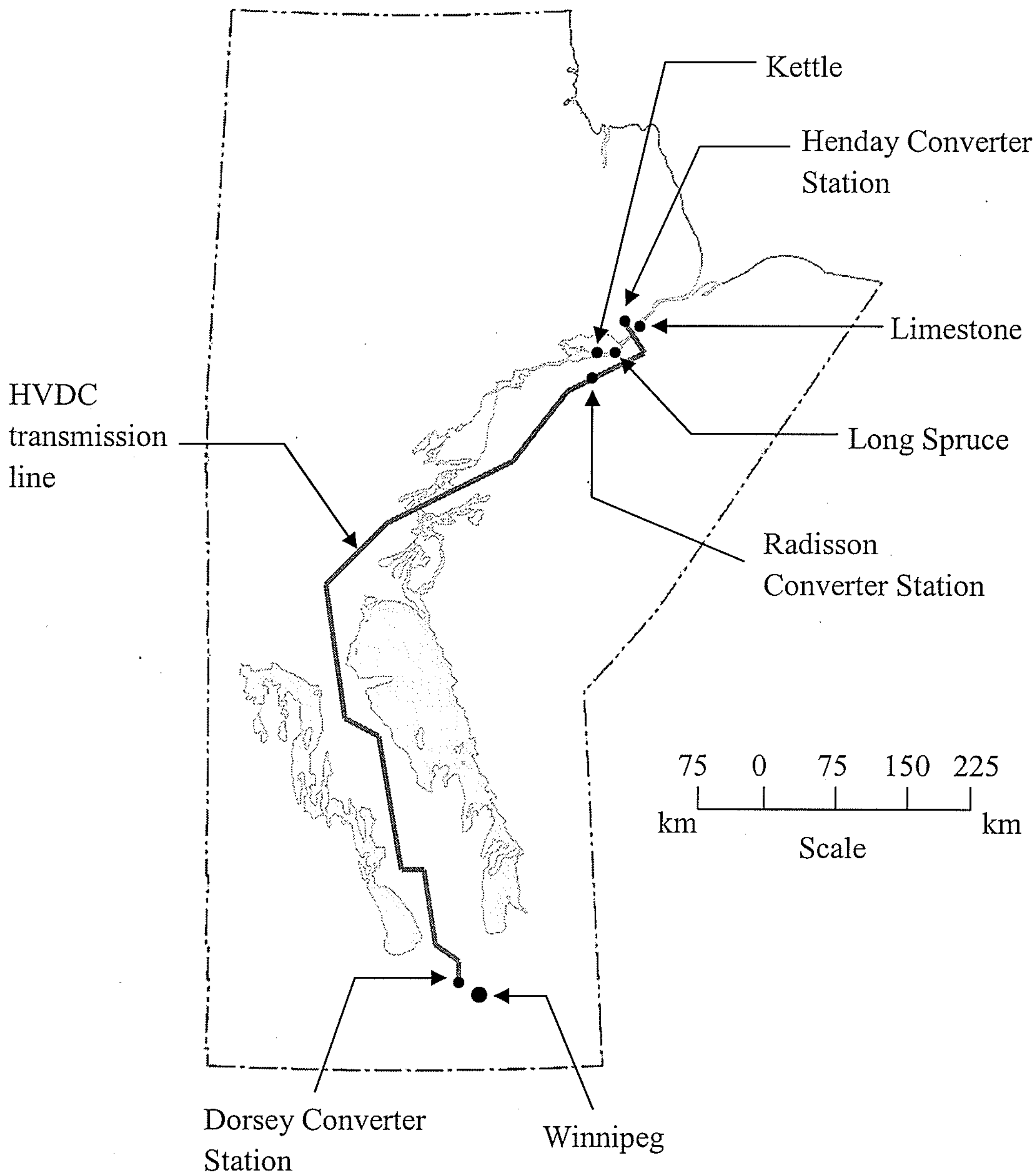

Figure 1-1: Map of Manitoba showing relevant Manitoba Hydro locations

At the Dorsey converter station the conversion process takes place in valve halls that store the thyristor valves which turn on and off in a controlled sequence to convert DC power to AC.

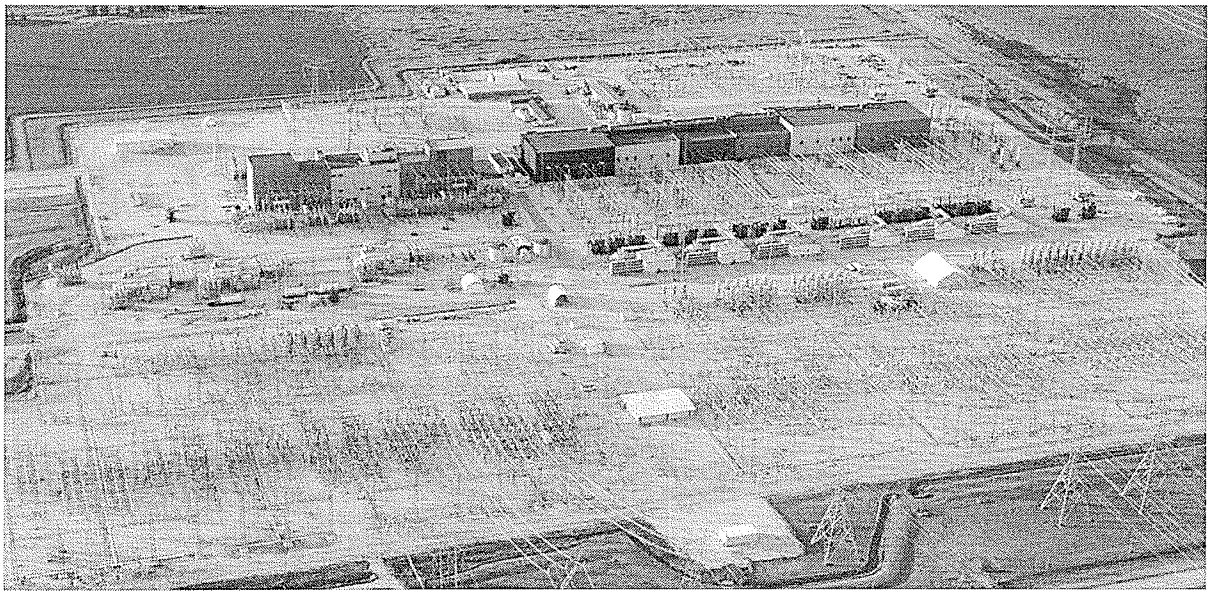

Figure 1-2: Aerial view of Dorsey Converter Station

Thyristor valves are solid state switches based on the silicon technology. Several different valve hall configurations are present at Dorsey. This thesis will focus on valve hall 41 (VH41) and valve hall 42 (VH42) that are part of Bipole 2. There are in total four valve halls that are part of Biopole 2 and each is capable of handling 500 MW of power. Stored within each valve hall are three DC/AC converter towers. A DC/AC converter tower consists of sixteen separate tiers that contain four thyristor modules and two reactor modules; there is a gap between each two tiers. Each four tiers make a single valve and therefore each tower has four valves. A typical DC/AC converter tower is shown in Figure 1-3. The towers are supported above the ground on posts, as shown in Figure 1-4. In VH41 and VH42 the posts elevate the towers 1.05 [m] and 3.52 [m], respectively, above the ground. Tower elevation is the most significant difference between these two valve halls.

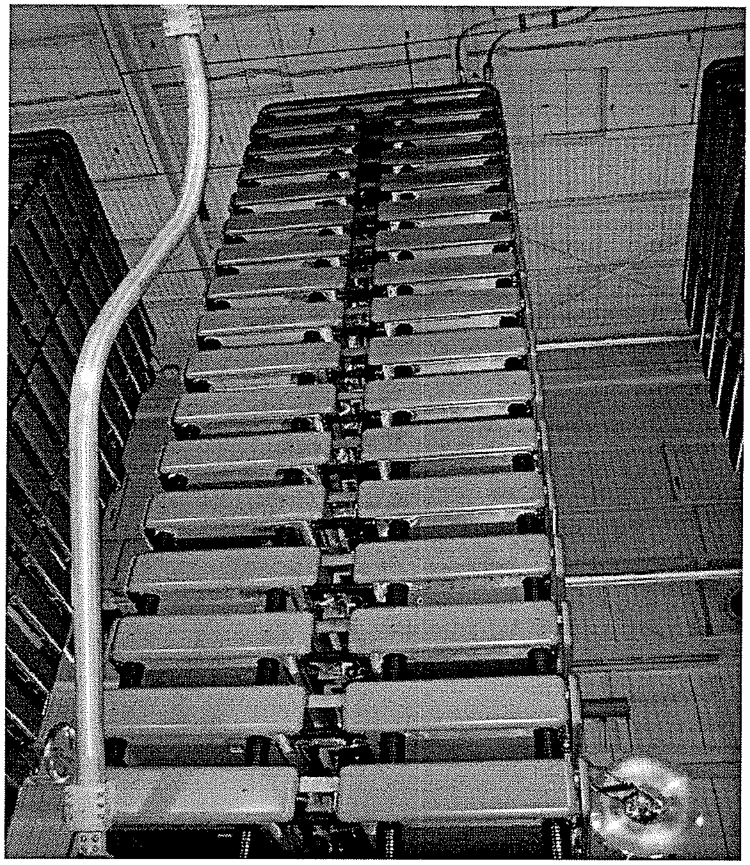

Figure 1-3: Typical DC/AC converter tower

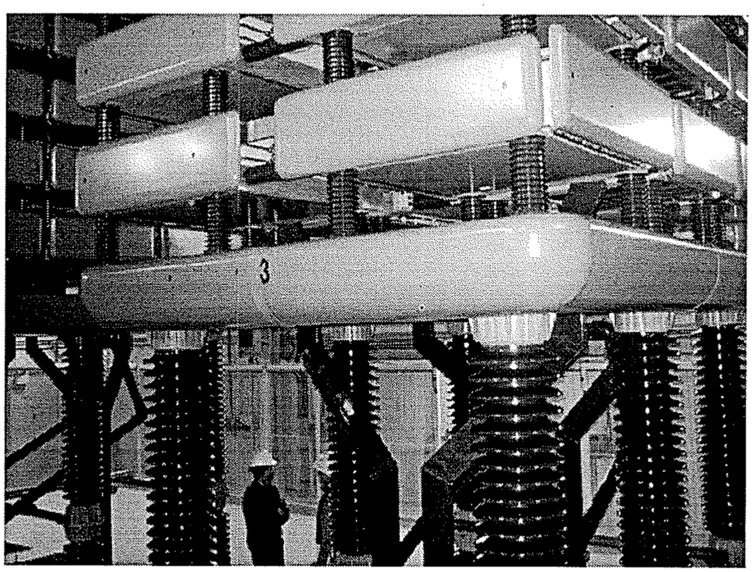

Figure 1-4: Posts that elevate a typical DC/AC converter tower above the ground (VH42 shown)

As a result of power losses during the conversion process, a significant amount of heat is generated in the DC/AC converter towers and a cooling system is utilized to maintain the thyristor valves at their recommended operating temperature. The heat is removed by a combination of a deionised water heat exchanger system and an air ventilation system.

The water heat exchanger system removes approximately 90% of the heat generated during the conversion process, while the remaining 10% is removed by the ventilation system. The ventilation system consists of inlet ports that are positioned in the floor in front and behind each tower. There is a grill over each inlet that angles the direction of the airflow. A typical inlet grill is shown in Figure 1-5. Due to the high voltage in the proximity of the thyristor valves, conductive material cannot be positioned in the general area of the converter towers. This limits the placement of the inlets. The return air is drawn from the highest point in the room and is mixed with fresh air in the return duct.

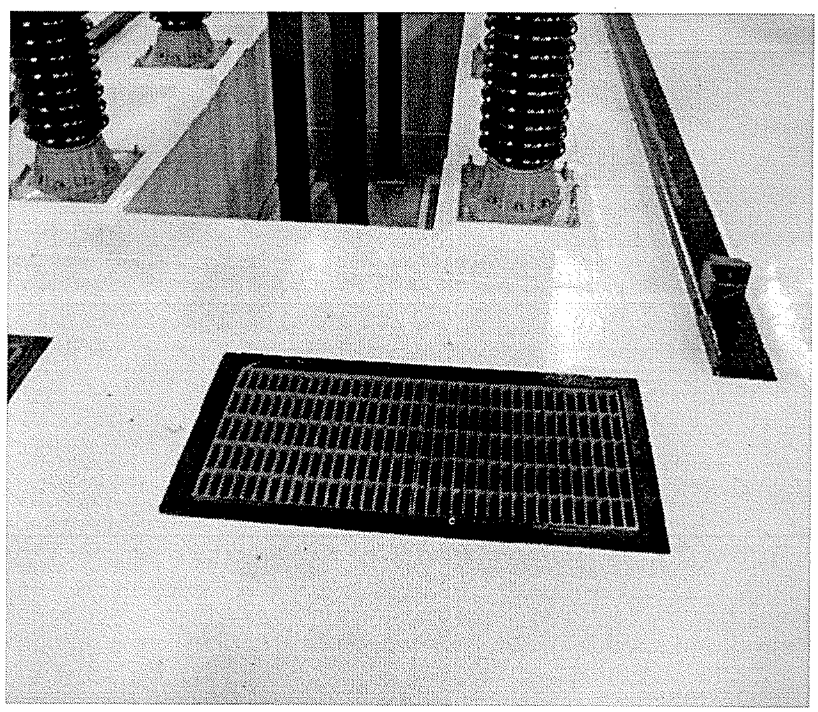

Figure 1-5: Typical ventilation system inlet grill

According to the design requirement, an environmental temperature of 5°C to 40°C is required for satisfactory operation of the converion equipment. However the enironmental temperature within a valve hall is not monitored. Overheating in the valves is monitored by a control system that gives an alarm when the heat exchanger outlet water temperature reaches 56°C . If the heat exchanger outlet water temperature reaches 59°C the control system will trip the power system. Current practice at Dorsey has been to reduce the power load by typically 20% when the alarm temperature is reached. Manitoba Hydro has concerns of thyristor overheating in the hotter climate during the summer.

The total air mass flow rate used in the existing ventilation system is adequate to remove the excess heat from the valve halls. However, the air temperature within the valve halls, particularly within the valves, is dependent on how the airflow circulates and interacts with the DC/AC converter tower.

1.2: Project Objectives

The goal of the present work is to numerically simulate the ventilation system that cools the DC/AC converter towers located within VH41 and VH42. An effective cooling strategy that reduces the temperature of the thyristor valves, relative to the existing industry design, will be determined for both valve halls. The geometry of the inlet air ports, location of the inlet air ports, and jet inlet angle will be varied to achieve this. It will also be determined if a particular tower elevation yields improved tower ventilation. The results from this study can serve as a guideline that Manitoba Hydro can use concerning upgrades to the ventilation system. Lowering the temperature of the thyristor valves is benefical to Manitoba Hydro because it will reduce the occurance of the contol system alarm being tripped. Operating the valve halls below full capacity is very costly to Manitoba Hydro because hydro power can be sold to other provinces and the U.S. Maintaining the thyristor valves at a lower operating temperature has the potential of extending their life span and improving performance.

Although this study is focused on a particular industry application, it is relevant to any industry that uses air ventilation to cool electrical components.

1.3: Previous Research on this Project

Previous M.Sc. research was conducted at the University of Manitoba by Ramirez-Iraheta (2004). Ramirez-Iraheta numerically simulated 2-D laminar airflow in a valve hall to determine the temperatue and velocity distributions for various inlet flow rates, tower locations in the domain, and the location of the inlet and outlet. The results from this study were summarized in Ramirez-Iraheta et al. (2006).

M.Sc. researcher Jeff Berg (2006) expanded on this work by simulating 3-D turbulent airflow in VH41. By using symmetry the size of the valve halls was reduced to both a quarter size and a half size. The size, location, and orientation of the inlet and outlet were varied as well as the jet inlet angle. The results from this study were summarized in two papers by Berg et al. (2008a, 2008b).

Post-Doctoral Fellow researcher Ahmed El-Shaboury (2009) further expanded on the modeling of VH41 by simlulating the quarter tower with open tiers and by simulating the full tower with staggered inlets. Both of these models were considerablly more computationally demanding relative to the previous simulations.

CHAPTER 2: LITERATURE REVIEW

2.1: Overview

In this chapter, a review of relevant numerical research will be presented. The work that was conducted in this thesis relates to turbulent mixed convection in a relatively large three-dimensional (3-D) domain with a turbulent air jet impinging on an array of heated blocks. There has been relatively little numerical research that would be comparable to this combination of phenomena. However, there has been considerable experimental and numerical research involving convection simulations that are similar to at least one, but not all aspects of the present study. The studies summarized in this chapter will be divided into 3 categories:

- In Section 2.2, research that produced results from experimental and numerical simulations for a two-dimensional (2-D) turbulent impinging jet on a heated surface is reviewed.
- In Section 2.3, research that produced results from experimental and numerical simulations from either 2-D laminar or turbulent channel flow over an array of heated blocks is reviewed.
- In Section 2.4, research that produced results from experimental and numerical simulations from ventilation cooling of electronics in either 2-D or 3-D domains is reviewed.

2.2: Turbulent Impinging Jet on a Heated Surface

Unless otherwise mentioned, the geometry for the work summarized in this section consists of a flat heated surface in a 2-D domain with an impinging turbulent jet directly above.

The height of the jet above the heated surface is defined as H and the length of the jet inlet is defined as W.

Merci et al. (2003) numerically investigated an impinging jet with different turbulence models. The standard k-ε model and a non-linear k-ε model with the Yap correction were compared to experimental results. The Yap correction decreases the turbulence length scale in the near wall region. The standard model failed to adequately predict the heat transfer, while the non-linear model yielded improved results. The authors illustrated that the energy equation can be simplified by neglecting the work done by the viscous and turbulent stresses, and the kinetic energy contribution in the total enthalpy without affecting the results.

Wang and Mujumdar (2004) conducted a comparative study of 5 low Reynolds number (LRN) k-ε turbulence models for impingement heat transfer. It was found that all models captured the shape of the Nusselt number (Nu) profile quite well, but overestimated the magnitude of Nu at both the stagnation points and the downstream points. All turbulence models preformed better when H/W was high. When the Yap correction was added, the prediction of Nu was improved significantly. When the turbulent intensity was increased from 1% to 6%, there was no change in the heat transfer or flow field except near the stagnation region.

Zurkerman and Lior (2005) described the relative strengths and drawbacks for the standard k-ε, standard k-ω, Re-Normalized Group (RNG) k-ε model, algebraic stress model (ASM), shear stress transport model (SST), and v^2f turbulence models for impinging jet flow and heat transfer. It was stated that the standard k-ε, standard k-ω, SST, and ASM models gave relatively large errors compared to experimental data sets. The computational time for the k-ε and k-ω model was stated to be the lowest. The SST and v^2f models were found to give better predictions but still failed to completely predict the behaviour of the jet over the entire domain. Direct numerical simulation (DNS) gave very accurate predictions but had extremely high computational time that limits its use. It was stated that the SST and v^2f models gave the best compromise between accuracy and computational time. The authors stated that the standard k-ε model gave accurate results in the free-jet region but poor results in the stagnation region and the wall jet region. It also gave poor predictions of the location of stagnation points in boundary layers. It was stated that the standard k-ε model is acknowledged to produce poor results for an impinging jet problem, but remains in use due to its common implementation and low computational costs. The standard k-ω predicted the flow in the wall jet region, but the model was sensitive to far-field boundary conditions to a greater extent than the standard k-ε model. It was concluded that the standard k-ω model is moderately better than the standard k-ε model, but has a higher computational cost. The RNG k-ε model provided improved performance over the standard model but required higher computational time. The RNG k-ε model had an additional term in the turbulent dissipation equation based on strain rates. Adding realizability constraints to the k-ε or k-ω model produced more accurate results. The RSM models calculated all six components of the Reynolds stress tensor. This model was computationally very demanding and although it eliminated the isotropy assumption that is used in the two-equation models it still used approximations to calculate the Reynolds stress tensor. It still gave large errors relative to experimental results

Ramezanpour et al. (2006) numerically investigated the heat transfer from a slot jet impinging on an inclined plane. The plane was inclined from 40° to 90°, where 90° was a horizontal plate. The RNG k-ε model and RSM were compared to experimental results for various cases. In general it was observed that by inclining the plane, the stagnation point was moved to the uphill side of the plate. This movement of the stagnation point increased by increasing *H*/*W* and by decreasing Reynolds number (Re) and the inclination angle. It was found that the local Nu was overall better predicted with the RNG k-ε model. But the RNG k-ε model underestimated the value for local Nu in the stagnation region. The RSM model more accurately predicted the streamlines from circulating flow. When the plane was horizontal, it was found that for both models the results were in better agreement with the experimental results, relative to when the plane was inclined.

Isman et al. (2007) numerically investigated a turbulent impinging jet. The standard k-ε, RNG k-ε, new k-ε, the Shih Zhu and Lumley (SZL), ASM, and the non-linear model of Girimaji (GIR) turbulence models were compared to experimental results. It was found in this study that for all turbulence models the numerical results for local Nu are lower at the impinging region but higher in the wall jet region relative to the experimental results. The ASM, SZL, and RNG models gave the most satisfactory results for heat transfer in the stagnation region, while the standard k-ε model predicted heat transfer better in the wall jet region. Both the RNG and standard k-ε model gave better agreement with the experimental results relative to the other models when the entire flow field was considered. The authors concluded that the results from the standard k-ε model have achieved notable success from an engineering point of view. The standard k-ε model has the advantage that it is the most widely used and validated turbulence model. In a parametric study using the standard k-ε model, it was shown that local Nu improved with increasing Re and decreasing nozzle-to-plate spacing. This was similar to what was observed from the experimental results. Increasing the turbulent intensity at the inlet from 1% to 6% improved the agreement with the experimental results.

Chang-geng and Jie-min (2007) conducted experimental and numerical simulations of heat transfer from a confined circular impinging jet. The standard k-ε, standard k-ω, SST k-ω, realizable k-ε, and RNG k-ε turbulent models were compared to the experimental results. The RNG k-ε model was found to accurately capture the experimental results, while the other models underestimated the local heat transfer coefficient in the wall jet region, especially in the stagnation region. The k-ω model failed to follow the typical saddle shape profile that was seen in the experimental results. The parameters Re and the ratio of height to diameter (*H*/*D*) were varied in the experiment. It was shown that the heat transfer had a strong dependence on Re. When *H*/*D* was 4 and Re was in the range of 600 to 8000 there was a flattening of the profile for Nu around the stagnation point. For all other cases, the profile for Nu was bell-shaped.

Hofmann et al. (2007) conducted an assessment of 13 widely used RANS turbulence models for impinging jets. The authors stated that when predicting wall jet heat transfer, nearly all models examined were found to be suitable. However, nearly all the models failed to accurately predict the local heat transfer near the stagnation region. The only model that gave agreeable predictions for this region was the SST k-ω model. This model was able to predict the secondary maximum correctly, which occurred when there was a small spacing between the inlet and the plate.

From the above discussion it was observed that for a jet impinging on a heated plane there is an inverse relation between the accuracy of a turbulence model and how computationally demanding that model is. Only the most computationally demanding model (DNS) can predict the entire flow field for an impinging jet. Some authors have stated that the standard k-ε model is inadequate, while other authors disagreed with this statement. Isman et al. (2007) stated that the standard k-ε model have achieved notable success from an engineering point of view in predicting the type of flow found in an impinging jet. Zurkerman and Lior (2005) stated that the k-ε model produces relatively poor results but remains in use due to its common implementation and low computational cost. It was found from the literature that turbulence models that are more computationally demanding relative to the standard k-ε model can still give poor predictions. Based on the wide use and the low computational time of the standard k-ε model, and the prediction errors that exist in most turbulence models for an impinging jet, the standard k-ε model was considered to be suitable to model an impinging jet for the work in this thesis.

2.3: Channel Flow Over an Array of Heated Blocks

Unless otherwise mentioned, the geometry for the work summarized below consists of a 2-D channel with one or more heated blocks protruding from a channel wall.

Desrayaud and Fichera (2003) analyzed numerically the natural convection in a 2-D vertical channel with a single protruding heat generating component. The parameters studied were the Rayleigh number (Ra), the Prandtl number (Pr), and the conductively ratio of the module and the fluid. The buoyancy driven flow along the horizontal surface inhibited the formation of a separate eddy at the lower corner. Along the vertical edge of the module, the flow accelerated but did not separate. On the upper horizontal face, flow separation occurred and an anti-clockwise eddy developed. In the channel area that is upstream of the module a plume-like behaviour was observed. The plume occupied less space as Ra was increased, and a large recirculation zone appeared downstream at the higher Ra values. The effect of module geometry for a fixed Ra value was also analyzed. Increasing the width of the module caused the downstream eddy to increase in size. Increasing the width also caused the eddy on the module's upper horizontal face to increase.

Majumdar and Deb (2003) numerically analyzed turbulent flow over an array of heated modules. The standard k-ε model, the LRN k-ε model based on the Lam and Bremhorst model, and the LRN k-ε model based on the Jones and Launder model were compared to experimental results. It was found that when Re was in the range of 2,000 to 5,000, the Jones and Launder model was the most accurate in predicting heat transfer and pressure drop. When Re was increased to 7,000, the standard k-ε model gave the most accurate predictions.

Arquis et al. (2006) numerically investigated a laminar impinging jet cooling an array of five protruding heat sources in a channel. The jet was positioned directly above the first block and the outlet was positioned downstream in the channel. The fluid flow and heat transfer characteristics were observed for various parameters such as: Re, channel height, slot width, spacing between blocks, and block height. By increasing Re, the rate of heat transfer on the blocks was found to increase. Small recirculation cells existed in the cavities between the blocks, and as the Re increased so did the strength of the vortices. In general, increasing the strength of the vortices led to greater cooling on the vertical faces of the blocks. At high Re, the vortices between the blocks rose above the top surface of the blocks. The effect of varying the width of the inlet slot on the flow structure was studied. For relatively large slot widths, circulation cells formed between the jet and the confining wall. For cases with relatively small slot widths, these circulations zones only appeared when the Re was also relatively high. It was also found that decreasing the width of the slot caused flow separation on the top surfaces of the blocks. For cases with a relatively high channel height, a circulation cell was formed between the impinging jet and the confining wall. The size of the circulation cell increased with increasing channel height. It was also observed that higher rates of cooling were achieved when the spacing between the blocks was increased.

Rao and Narasimham (2007) numerically investigated laminar mixed convection on protruding heat generating ribs in a vertical channel. A parametric study was performed by varying Grashof number (Gr) and Re. For a constant Gr, the velocity component resulting from natural convection decreased with increasing Re. This is a result of increasing the forced-convection component due to the increase in Re. As the value of Gr was lowered, the velocity from natural convection appeared to stabilize around a constant value and did not change as Re was increased. As Gr was increased, a higher Re was needed to reach free convection velocity stabilization. For the cases with no free convection, when Re was increased from a relatively small value to a large value, a vortex formed on the vertical face of the lowest component. When only free convection was present in the channel and a low Gr was used, the circulation cells between the components were relatively week and the stagnation point was closer to the upper horizontal surface. For a higher Gr, the circulation zones tended to be closer to the bottom horizontal faces.

Elsaadawy et al. (2008) numerically investigated turbulent flow through a channel with 6 protruding heat sources. The objective of their study was to determine the proper turbulence model to use in the thermal analysis of electronic systems. The results from the standard k-ε, RNG k-ε, SST, and RSM turbulence models were compared to results from both experiments and DNS simulations. The authors stated that the standard k-ε and RNG k-ε model are not the best suited for predicting the flow phenomena that occur in 2-D ribbed channel flow; which consists of separation, circulation, and reattachment. Both the RSM and the SST models reasonably predicted the results. Since the SST model is less computationally demanding, the authors determined that it was the most suitable model.

Eiamsa-ard and Promvonge (2008) numerically studied heat transfer from turbulent channel flow over periodic grooves. The results from the standard k-ε, RNG k-ε, standard k-ω, and the SST turbulence model were compared to experimental results. It was shown that both the standard k-ε and RNG k-ε models were suitable for this type of flow. The standard k-ε model was used in a parametric study. Different groove-width ratios were tested and it was found that the highest Nu values occurred when the ratio of the length of the groove and the spacing between the grooves was 0.75.

From the above discussion it was observed that channel flow over heated blocks has been simulated using laminar and turbulent flow conditions. Elsaadawy et al. (2008) stated that the standard k-ε model was not ideal for this type of flow. However, Eiamsa-ard and Promvonge (2008) used the standard k-ε model in a parametric study. Majumdar and Deb (2003) found that the standard k-ε model gave accurate predictions when Re was increased to 7,000. Based on the above findings, the standard k-ε model can be considered suitable for modeling flow over heated blocks.

2.4: Ventilation Cooling of Electronics in a Room

Lu et al. (2002) numerically investigated convection heat transfer in a heated room. The domain consisted of a 3-D room with one of the walls containing a heated surface and an opening. The results from the standard k-ε and the LRN k-ε turbulence model were compared to experimental results. It was observed that the LRN k-ε turbulence model produced airflow patterns that were closer to the experimental results. Both models were able to capture the main flow features. The temperature distribution predicted by both turbulence models were in agreement with the measured data.

Berg et al. (2007) numerically studied the flow structure of a turbulent rectangular free jet in a 3-D room. All surfaces in the domain were adiabatic. Experimental results were compared to the standard k-ε and the standard k-ω turbulence models. Two different inlet boundary conditions were tested for each model: a uniform velocity profile and a profile matching the experimental data. It was found that when the standard k-ε model was used with a velocity profile matching the experimental data, the main features of the flow field were captured, including the saddle shaped velocity profile in the near-field region and the rate of velocity decay in the far-field region.

Bilgen and Muftuoglu (2007) studied numerically the case of natural convection in an open 2-D square cavity with discrete heaters on the left wall. The right wall was open to the ambient air and all other walls were adiabatic. The goal of this work was to optimize the size and position of a various number of discrete heaters. It was observed that when a single heater was used, the heat transfer varied as the position of the heater was changed for all Ra values. The heat transfer was at its lowest when the heater was located at the bottom of the wall and increased as the heater was moved towards the midpoint of the wall. It was observed that heat transfer increased as the size of the heater was increased. In general, increasing Ra caused the optimal position of the heater to be located closer to the ground. This was explained by there being increased circulation in the lower half of the cavity. The optimal position also became closer to the ground as the heater size was increased. When Ra was low, the heat transfer in the domain was conduction based and Nu was the same irrespective of heater size or location. As tRa was increased, convection became the dominate means of heat transfer and Nu increased with heater size. The volume flow rate in the domain was an increasing function of both Ra and heater size.

Yilmaz and Fraser (2007) investigated turbulent natural convection in a vertical parallel-plate channel with asymmetric heating both numerically and experimentally. Variations of the LRN k-ε turbulence model were used in this study. All turbulence models tested were able to predict the average heat transfer and induced flow rate almost within the limits of experimental error. None of the LRN k-ε turbulence models could be singled out as the best model. The profiles for turbulent kinetic energy from the experimental data indicated that fully turbulent flow had been reached at the outlet, indicating that the assumption to use a turbulence model was valid.

Radhakrishnan et al. (2007) reported a study on an experimental and numerical investigation of mixed convection from a vertical heat generating plate in a ventilation cavity. The base geometry consisted of a thin rectangular heat generating element positioned vertically in the centre of a rectangular room. Air entered the room through an inlet located in the bottom left corner and exited through an outlet located at the top right corner. All walls of the cavity were insulated. From the experimental results it was shown that as Re increased, the maximum temperature on the heater decreased. It was found that Nu increased linearly with increases in Re. The Nu trend lines stayed clustered together as Re was increased, irrespective of the heaters output. For the numerical study, the RNG k-ε turbulence model was used and the geometry of the room was simplified to be 2-D. The results from experimental and numerical studies were compared and they were found to be in agreement. By analyzing streamlines in the domain it was shown that the flow was not uniformly distributed in the room. The majority of the flow from the inlet bypassed the heater and flowed vertically up the right wall without touching the heater. The zone to the left of the heater was stagnant. This demonstrated that the ideal place for positioning the heater was not in the centre. The heater was then moved to different locations in the domain and at different inclinations. It was found that the average temperature was highest when the heater was positioned at the far left of the room and the average temperature was lower when it was positioned to the right of the room. When the heater was positioned lower to the bottom, the average temperature was decreased. When the heated plate was positioned horizontally, the maximum temperature was lower relative to when the plate was positioned vertically. When the plate was inclined at 45°, the maximum temperature was higher than the horizontal position, but was still less than the vertical position.

Koca (2008) studied numerically laminar natural convection in a 2-D domain with a vertical heat generating plate mounted on the bottom plane at various locations. An opening was located on the top plane at various locations. Heat transfer was found to increase as Ra increased, as the size of the opening increased, and as the size of the plate increased. Both the location of the plate and the opening had an effect on the heat transfer.

Tsay and Cheng (2009) studied laminar natural convection cooling of 3 heat generating blocks mounted vertically on a board that is suspended in the centre of a 2-D cavity. The number of air vents was varied from 0 to 3 as was the location of the air vents. Airflow was simulated to be circulated on the outside of the cavity. When three vents were added to the cavity the maximum temperature reduced by up to 45% relative to the case with no vents. The maximum temperature from the case with two vents was only 6% higher than the case with three vents. It was found that increasing Ra increases Nu.

From the above discussion it was observed that the ventilation cooling of electronics in a room has been simulated using laminar and turbulent flow conditions. Turbulence was modeled using variations of the k-ε model. Berg et al. (2007) found that the standard k-ε model can accurately predict the velocity decay of a jet in a 3-D room. Since jet velocity decay is an important part of the flow phenomenon that was studied in this thesis, the standard k-ε model will be considered suitable for predicting the ventilation of electronics in a room.

2.5: Concluding Remarks

From the above review, it is clear that there has been a significant amount of research done comparing various turbulence models to experimental results for heat transfer from impinging jets, channel flow over heated blocks, and ventilation cooling of electronics in a room. A majority of this work was done with relatively simple 2-D geometries, which limits their applicability to real-life engineering applications. Certain industry applications contain flow fields that cannot be represented as a 2-D domain. The reason that previous research has been limited to a 2-D domain is that obtaining results from a 3-D domain is very computationally demanding.

This work will attempt to expand on the existing literature by analyzing the flow structure and heat transfer in a large 3-D domain with turbulence, mixed convection, an impinging jet, and flow over heated blocks. These conditions are relevant to various industrial applications such as the cooling of a DC/AC converter tower. To the author's knowledge, there has been no research conducted that would be comparable to this, aside from previous work that has been done by other researchers at the University of Manitoba.

CHAPTER 3: MODEL DESCRIPTION

3.1: Domain

The converter towers are arranged in a row of three towers within a valve hall. The towers are 7.98 [m] high, 2.57 [m] long, and 3.56 [m] wide. In VH41, the towers are elevated 1.05 [m] above the ground. In VH42, the towers are elevated 3.52 [m] above the ground. The elevation of the tower above the ground will be denoted as H_1. Each converter tower consists of a series of sixteen vertically stacked tiers. The tiers are 0.33 [m] in height and there is a 0.18 [m] vertical gap between each two tiers. An isometric view of a CAD model representing VH41 is shown in Figure 3-1.

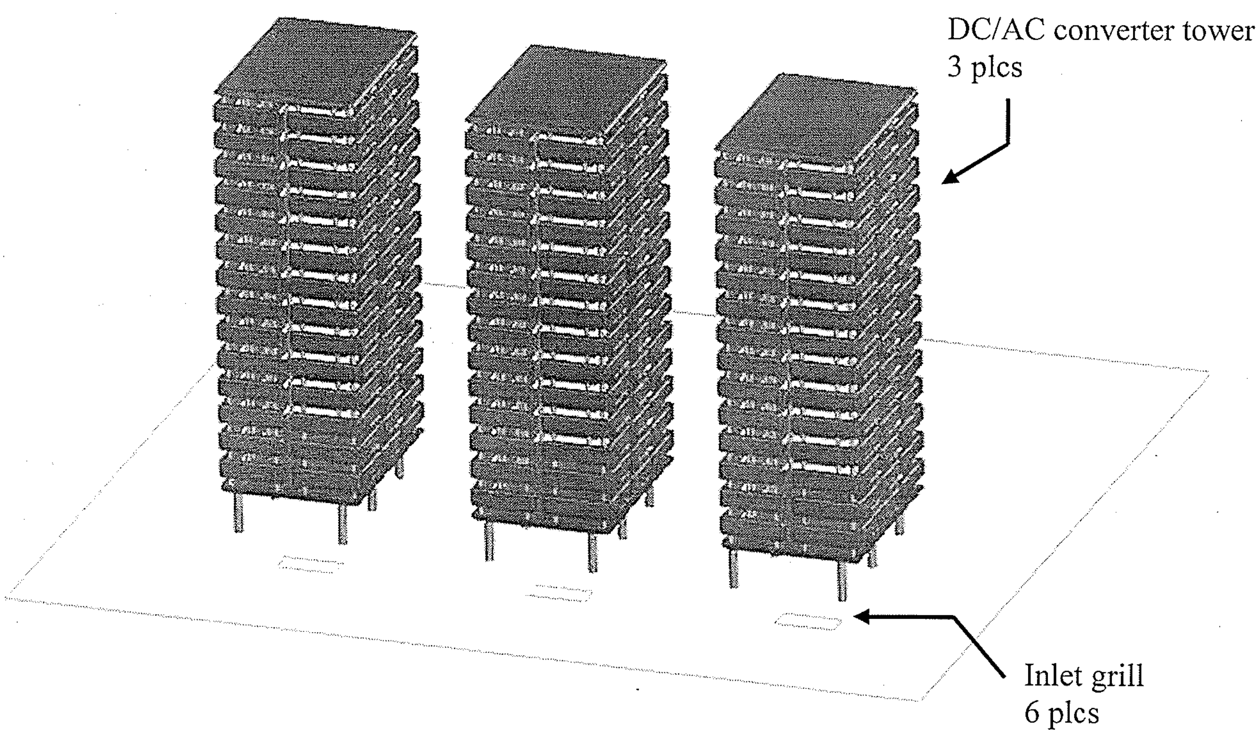

Figure 3-1: Isometric view of a CAD model representing VH41 (parts removed for clarity)

Each tier consists of four thyristor modules and two reactor modules. A cluster of internal pipes is located in the centre of each tier. Plastic plates are present on the outside of each tier to enclose the electrical components. The top and bottom of a tier are not enclosed by any panels. Detailed engineering drawings of the inside of a tier were not available. The internal arrangement of the tiers was determined through visual inspection when the valve hall was not in operation. A representative top view of the insides of a tier is shown in Figure 3-2. The dimensions of a tier were taken from the modules and do not include the plastic plates.

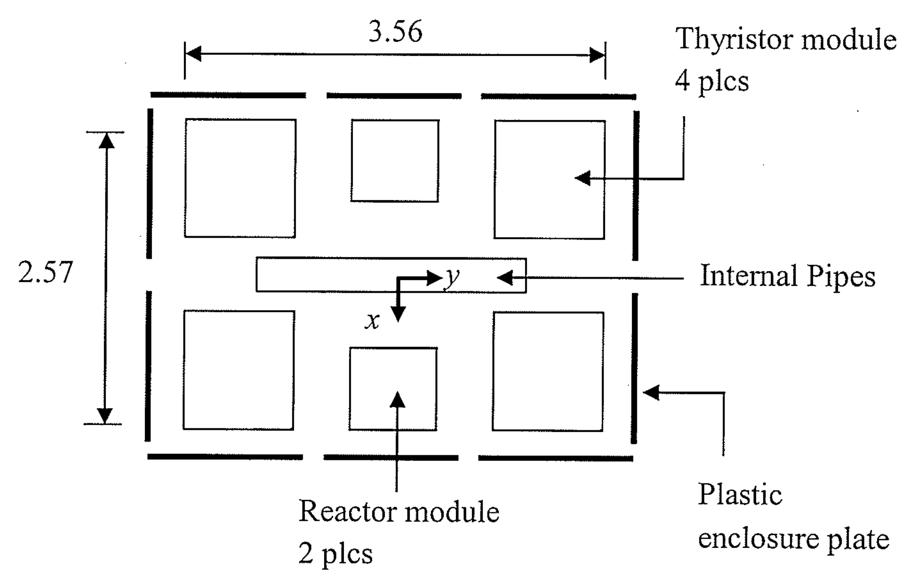

Figure 3-2: Representative top view of the inside of a tier.
Dimensions are in meters.

The valve hall ventilation system consists of six inlets located on the floor. Each converter tower has two inlets located at opposite sides in a staggered arrangement. A grill is present over each inlet. The angle that the inlet grill directs the airflow towards the tower will be defined as θ. In VH41 and VH42, θ is 60° and 90°, respectively. The airflow is removed from the valve hall through outlets located on the ceiling and distributed asymmetrically above the towers.

The valve halls that the converter towers occupy are 16.75 [m] in length and 15.60 [m] wide. In VH41 the ceiling is 13.35 [m] in height and in VH42 the ceiling is 18.89 [m] in height. The height of the valve hall will be denoted as H_2. The major difference between VH41 and VH42 is the tower elevation above the ground and the ceiling height. Any other differences are not considered in this study.

A 5-m high safety fence closes off the tower area to keep people out due to the high voltage present when the tower is in operation. The fence consists of a wire mesh and airflow can readily move through it. A side view and top view of the valve hall geometry is shown in Figures 3-3 and 3-4, respectively.

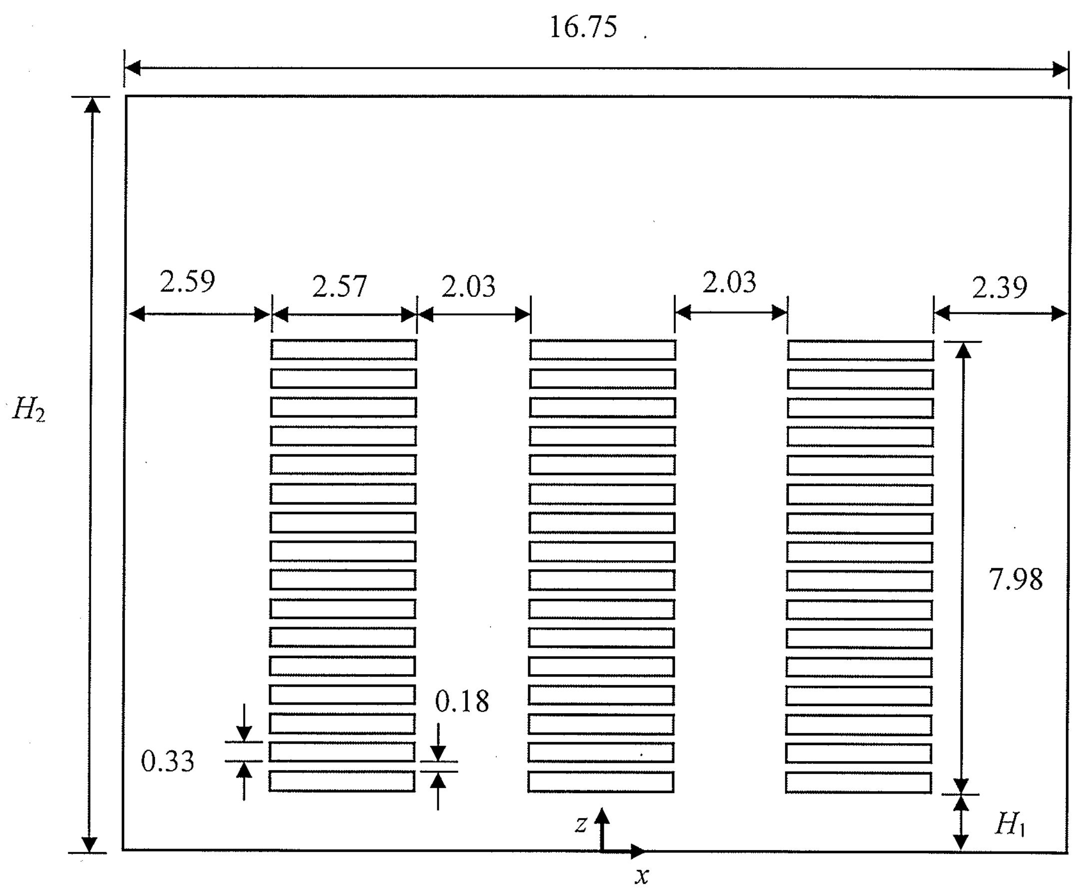

Figure 3-3: Side view of the valve hall. Dimensions are in meters.

The geometry of the valve halls is very complex, consisting of three towers, 6 inlets, outlets, a safety fence, and complex electrical components. If the domain was modeled completely, the computational time would be extremely high. To reduce the complexity of the domain the following modifications have been made.

Modification 1: Symmetry planes S2 have been placed between the middle tower and the outer towers, and the side walls were replaced by symmetry planes S2. This allows for the domain to be represented as a large array of towers. Since the towers are identical, the computational domain can be reduced to a single tower.

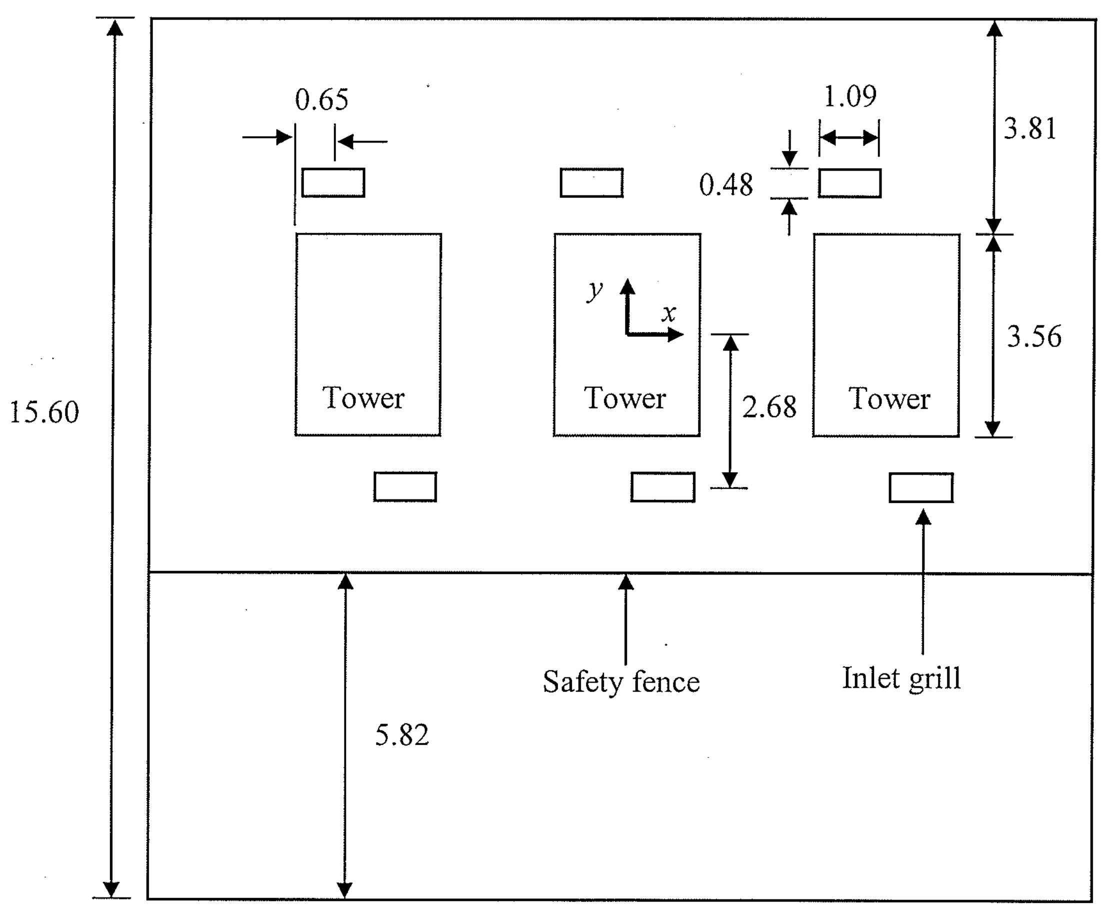

Figure 3-4: Top view of the valve hall. Dimensions are in meters.

Modification 2: The floor inlets were repositioned to so that the centre of each inlet was aligned with the centre of the tower. This allows for symmetry plane S1 to be placed in the centre of each tower. The domain can now be reduced from a single tower to a half tower.

A side view of the domain with symmetry planes S1 and S2 is shown in Figure 3-5. From now on, symmetry planes will be represented as dashed lines. The floor and ceiling are now defined as W1 and W3, respectively.

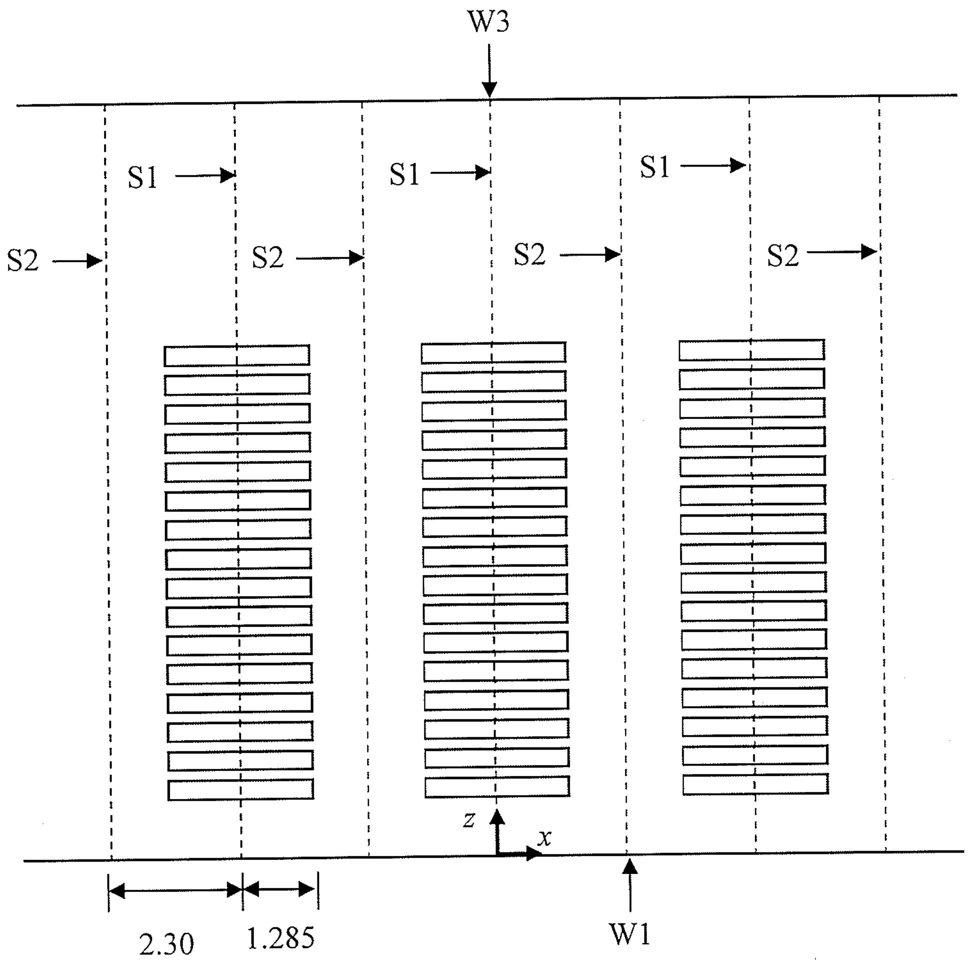

Figure 3-5: Side view of the valve hall with modifications 1 and 2. Dimensions are in meters.

Modification 3: The safety fence was removed and the wall beyond the safety fence was moved closer to the towers. This wall was placed at the same distance from the tower centre line as the wall on the opposite side of the tower. This allows for symmetry plane S3 to be placed in the centre of each tower. The domain can now be reduced to quarter the size of a single tower. A top view of the domain with the modified inlet locations and symmetry planes S1, S2, and S3 is shown in Figure 3-6. The side walls are now defined as W2.

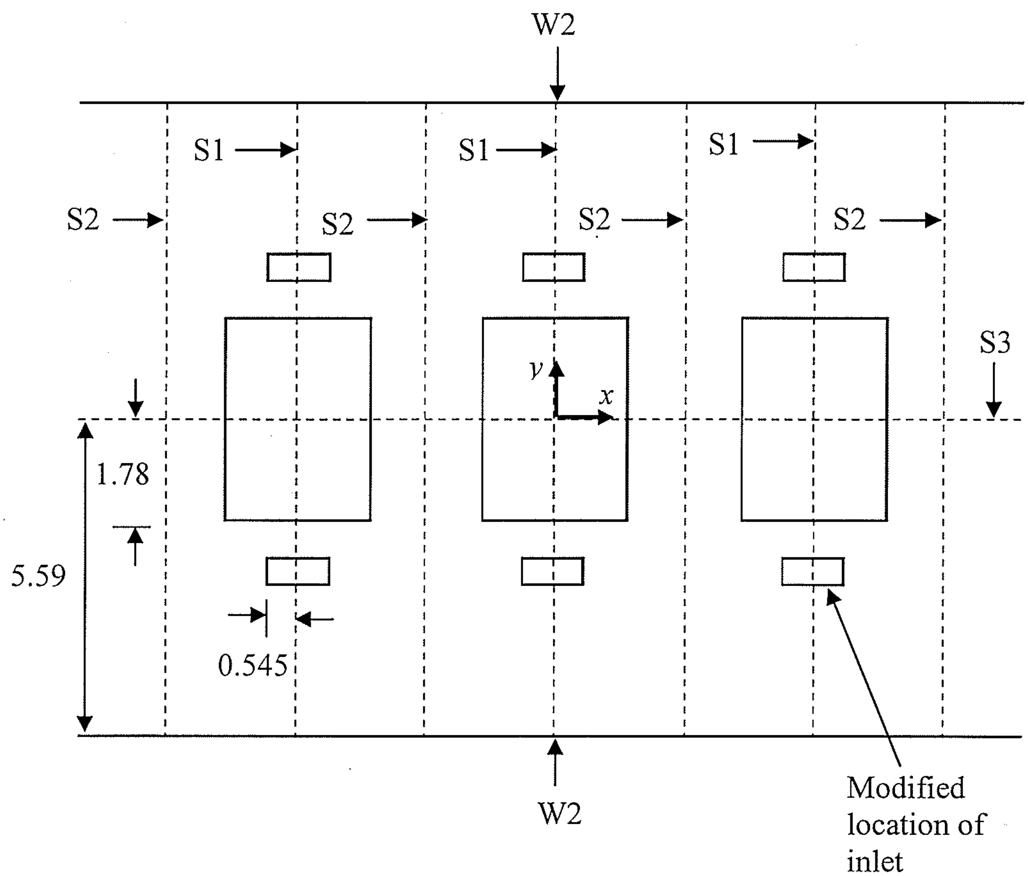

Figure 3-6: Top view of the valve hall with modifications 1 to 3. Dimensions are in meters.

Modification 4: The air outlets were modified and repositioned so that they were the same size as the inlets and were positioned directly above each inlet. The total area of the outlets has not been changed with this modification.

Modification 5: The tower tiers consist of a collection of four thyristor modules, two reactor modules, and internal pipes. The available computational resources imposed the modification to model the tier as a solid block that has the same overall dimensions of the modules. The solid block produces the same total rate of energy as the original set of thyristor and reactor modules. The top and bottom horizontal surfaces of each tier will be defined as T1 and T2, respectively. The vertical surfaces of each tier in the *x*-*z* and *y*-*z* directions will be defined as T3 and T4, respectively.

By implementing modifications 1 to 5, the quarter-tower domain was obtained, as shown in Figure 3-7.

The length of the inlet in the *x*-direction and *y*-direction will be defined as L_x and L_y, respectively. The distance between the centre of the inlet and symmetry plane S3 will be defined as P_y.

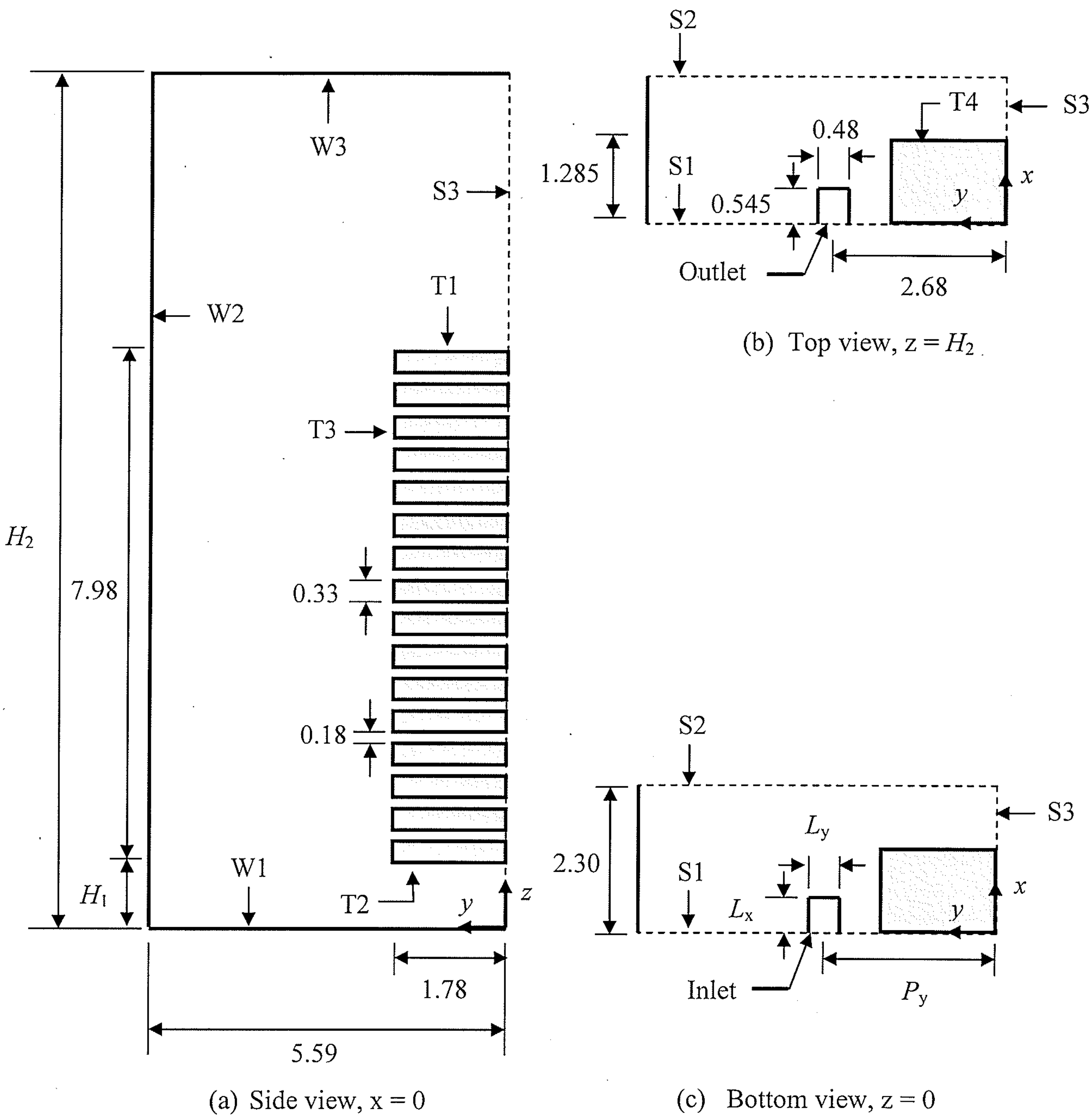

Figure 3-7: Quarter domain using modifications 1 to 5. Dimensions are in meters.

3.2: Assumptions

The following assumptions were made in formulating the mathematical model:

- The airflow was turbulent at medium intensity.
- The eddy-viscosity approximation was used to model the Reynolds stresses.
- Steady-state conditions were assumed.
- The air was assumed to be Newtonian and compressibility effects were assumed to be negligible.
- The properties of the air were constant, except for the density in the buoyancy term.
- Heat transfer by radiation was assumed to be negligible.
- The outer walls of the domain were assumed to be adiabatic.

3.3: Mathematical Model

3.3.1: Governing Equations

Using the assumptions discussed in Section 3.2, the time-averaged governing equations for the conservation of mass, momentum, and energy can be expressed in tensor form as:

Continuity:

$$\frac{\partial(\rho u_j)}{\partial x_j} = 0 \tag{3.1}$$

Momentum:

$$\left(u_j \frac{\partial(\rho u_i)}{\partial x_j}\right) = -\frac{\partial P}{\partial x_i} + \frac{\partial}{\partial x_j}\left((\mu + \mu_t)\frac{\partial u_i}{\partial x_j}\right) + \rho g_i, \quad i = 1, 2, 3 \tag{3.2}$$

Energy:

$$\frac{\partial(\rho u_j T)}{\partial x_j} = \frac{\partial}{\partial x_j}\left(\left(\frac{\lambda}{C_p} + \frac{\mu_t}{Pr_t}\right)\frac{\partial T}{\partial x_j}\right) \tag{3.3}$$

where x_j is the position vector (x, y, z), u_i is the Cartesian time-average velocity components ($u_1 = u$, $u_2 = v$, $u_3 = w$), P is the time-averaged pressure, Pr_t is the turbulent Prandtl number ($Pr_t = 0.9$), μ_t is the eddy viscosity, $g_i = -9.8$ [m/s^2] for $i = 3$, and $g_i = 0$ for $i = 1$ and 2.

Splitting the pressure into dynamic (P^*) and hydrostatic components:

$$P^* = P - \rho_o g_i x_i \tag{3.4}$$

the resulting momentum equation can be written as:

$$\left(u_j \frac{\partial(\rho u_i)}{\partial x_j}\right) = -\frac{\partial P^*}{\partial x_i} + \frac{\partial}{\partial x_j}\left((\mu + \mu_t)\frac{\partial u_i}{\partial x_j}\right) + (\rho - \rho_o) g_i, \qquad i = 1, 2, 3 \tag{3.5}$$

where ρ_o is the density of the air at the inlet.

The above equations form a mathematical model that can represent the flow field and heat transfer that occurs within the valve halls. However, additional equations need to be introduced to solve for the μ_t term in the momentum and energy equations.

3.3.2: Turbulence Closure

A turbulence model is required to solve μ_t in Eq. (3.3) and Eq. (3.5) for turbulent flows. The two equation turbulence model, the standard k- ε model with a scalable wall-function was used to solve this term.

3.3.2.1: The Standard k-ε Turbulence Model

In the standard k- ε model, the eddy viscosity is computed using the relation:

$$\mu_t = C_\mu \rho \frac{k^2}{\varepsilon} \tag{3.6}$$

where C_μ is a constant and the values of turbulent kinetic energy, k, and the dissipation, ε, come from the solution to the following transport equations:

$$u_i \frac{\partial(\rho k)}{\partial x_i} = \frac{\partial}{\partial x_i}\left[\left(\mu + \frac{\mu_t}{\sigma_k}\right)\frac{\partial k}{\partial x_i}\right] + P_k - \rho\varepsilon \tag{3.7}$$

$$u_i \frac{\partial(\rho \varepsilon)}{\partial x_i} = \left[\frac{\partial}{\partial x_i}\left(\mu + \frac{\mu_t}{\sigma_\varepsilon}\right)\frac{\partial \varepsilon}{\partial x_i}\right] + \frac{\varepsilon}{k}\left(C_{\varepsilon 1} P_k - C_{\varepsilon 2}\rho\varepsilon\right) \tag{3.8}$$

Where the turbulence production term, P_k, is modeled using:

$$P_k = \mu_t \frac{\partial u_i}{\partial x_j}\left(\frac{\partial u_i}{\partial x_j} + \frac{\partial u_j}{\partial x_i}\right) \tag{3.9}$$

The values for the standard k- ε equation constants used in this work are: $C_\mu = 0.09$, $C_{\varepsilon 1} = 1.44$, $C_{\varepsilon 2} = 1.92$, $\sigma_k = 1.0$, and $\sigma_\varepsilon = 1.3$.

The scalable wall function approach of Grotjans and Menter (1998) was used for modeling the flow near the wall. This approach is an extension of the standard wall function approach of Launder and Spalding (1974). In the log-law region, the near wall tangential velocity U_t is related to the wall shear stress τ_w by means of a logarithmic relation. In the wall function approach, are applied which correct the wall condition with the dependent variables at the first near-wall mesh node which is assumed to lie in the logarithmic region of the boundary layer. The relation for the near wall velocity in the logarithmic region is given by:

$$U_t = \left({}^{u_\tau}/_{K}\right) log(y^+) + C \tag{3.10}$$

where the non-dimensional wall distance y^+, is defined as:

$$y^+ = \frac{\rho u_\tau n}{\mu} \tag{3.11}$$

The friction velocity, u_τ, is given by:

$$u_\tau = \left(\frac{\tau_W}{\rho}\right)^{1/2} \tag{3.12}$$

n is the normal distance to the wall, ($K = 0.41$) is the von Karman constant, and C is a constant that depends on the wall roughness ($C = 5.2$ for a smooth wall).

Using the wall function approach, the near wall turbulence quantities, k, ε, and μ_t in the logarithmic region were calculated from:

$$k = \frac{u_\tau^2}{\sqrt{C_\mu}} \tag{3.13}$$

$$\varepsilon = \frac{u_\tau^3}{(Kn)} \tag{3.14}$$

$$\mu_t = \rho K u_\tau n \tag{3.15}$$

The fundamental principle of the scalable wall function approach of Grotjans and Menter (1998) is to limit the value of y^+, near the wall, $\tilde{y}^+$, used in the logarithmic formulation to a value of 11.0. The value of $\tilde{y}^+$ was determined from the intersection of the logarithmic and linear profiles near the wall using: $\tilde{y}^+ = max(y^+, 11.06)$. The computed $\tilde{y}^+$ value was not allowed to fall below this limit and therefore all mesh points were outside the viscous sub-layer. As a result, mesh inconsistencies associated with applying the k and ε equations in this region are avoided. The flux boundary conditions applied at the wall for the scalable wall function approach are as follows:

$$\mu_t \frac{\partial U_t}{\partial n} = -\rho u_\tau max(|u_\tau|, u^*) \tag{3.16}$$

$$\frac{\partial k}{\partial n} = 0 \tag{3.17}$$

$$\frac{\mu_t}{\sigma_\varepsilon}\frac{\partial \varepsilon}{\partial n} = -\frac{1}{\sigma_\varepsilon}\frac{(u^*)^5 \rho^2}{\tilde{y}^+ \mu} \times \left[\frac{2+e}{2+2e} + F_{cal}\frac{e}{2}\frac{\sigma_\varepsilon \sqrt{C_\mu}}{k^2}(C_{\varepsilon 2} - C_{\varepsilon 1})\right] \tag{3.18}$$

with:

$$e = {\Delta y^+}/{\tilde{y}^+} \tag{3.19}$$

and

$$u^* = C_\mu^{1/4} k^{1/2} \tag{3.20}$$

In Eqs. (3.16) to (3.20), Δy^+ is the actual y^+ value from the wall to the first interior node, F_{cal} is a calibration function based on the coarseness of the mesh, and u^* is the alternative velocity scale used to prevent the flux from going to zero at separation points.

3.3.3: Boundary Conditions

The following conditions were used at the domain boundaries. Refer to Figure 3-6 for the location of the boundaries.

The location of the inlet port is given by,

$$0 \leq x < L_x, \qquad \left(P_y - \frac{L_y}{2}\right) \leq y < \left(P_y + \frac{L_y}{2}\right), \qquad \text{and } z = 0$$

The velocity components at the inlet were calculated using:

$$u_o = 0 \tag{3.21}$$

$$v_o = \frac{-w_o}{tan\,\theta} \tag{3.22}$$

$$w_o = \frac{\dot{m}_o}{\rho_o L_x L_y} \tag{3.23}$$

The air entering the domain through the inlet is at a uniform temperature T_o.

The inlet turbulent kinetic energy, k_o, was calculated using:

$$k_o = \frac{3}{2} I_o^2 \left(\sqrt{v_o^2 + w_o^2}\right)^2 \tag{3.24}$$

where I_o is the inlet turbulence intensity. The inlet dissipation ε_o was calculated using:

$$\varepsilon_o = C_\mu \rho_o \frac{k_o^2}{R_o \mu} \tag{3.25}$$

where R_o is the inlet viscosity ratio $\left({}^{\mu_t}/_{\mu}\right)$.

The location of the outlet port is given by,

$0 \leq x < 0.545\ [m], \qquad 2.44\ [m] \leq y < 2.93\ [m], \qquad \text{and } z = H_2$

A specified average pressure was applied at the outlet area:

$$\bar{P}^* = 0 \text{ over the outlet opening} \tag{3.26}$$

Symmetry conditions were defined along planes S1, S2, S3:

$$u = \frac{\partial v}{\partial x} = \frac{\partial w}{\partial x} = \frac{\partial T}{\partial x} = 0 \quad \text{on S1 and S2} \tag{3.27}$$

$$v = \frac{\partial u}{\partial y} = \frac{\partial w}{\partial y} = \frac{\partial T}{\partial y} = 0 \quad \text{on S3} \tag{3.28}$$

Wall boundary conditions were defined along planes W1, W2, W3, T1, T2, T3, and T4:

$$u = v = w = 0 \quad \text{all walls} \tag{3.29}$$

$$\frac{\partial T}{\partial z} = 0 \qquad \text{on W1 and W3} \tag{3.30}$$

$$\frac{\partial T}{\partial y} = 0 \qquad \text{on W2} \tag{3.31}$$

$$\frac{\partial T}{\partial z} = -\frac{q''}{\lambda} \qquad \text{on T1} \tag{3.32}$$

$$\frac{\partial T}{\partial z} = \frac{q''}{\lambda} \qquad \text{on T2} \tag{3.33}$$

$$\frac{\partial T}{\partial y} = -\frac{q''}{\lambda} \qquad \text{on T3} \tag{3.34}$$

$$\frac{\partial T}{\partial x} = -\frac{q''}{\lambda} \qquad \text{on T4} \tag{3.35}$$

The domain parameters that were held constant for all cases are summarized in Table 3-1. The constant parameters were determined by researcher Jeff Berg in VH41.

Table 3-1: Constant domain parameters

$\dot{m}_o$ [kg/s]	T_o [°C]	q'' [W/m^2]	I_o	R_o
0.684	21.2	60.6	0.05	10

CHAPTER 4: NUMERICAL SOLUTION

4.1: Introduction

This chapter outlines the numerical procedure that was used to obtain a solution to the governing equations that were discussed in Chapter 3. The domain was divided into small control volumes with a node at the centre of each control volume. The governing equations were integrated over each control volume to derive coupled algebraic equations for the velocity components, pressure, temperature, and the turbulence quantities k and ε. At each node, the solution was obtained for all of the quantities by iteratively solving the algebraic equations.

4.2: Grid Generation

To generate the computational grid for the solution domain the software package ANSYS ICEM CFD was used. This program is capable of generating CAD models and hexahedral unstructured meshes.

A CAD model was used to define the geometry of the computational domain and a hexahedral mesh divides the domain into smaller rectangular control volumes. At the centre of each control volume is a node. The mesh was analyzed to ensure that the control volume edges were always at 90°.

A relatively high nodal density was required around the tower to capture the complexity of the flow within the gaps. Away from the tower, the nodal density was reduced significantly. Since the control volume edges are always at 90°, the high nodal density around the tower was projected into the outer region of the domain. This resulted in the nodal density being excessively high where it was not required. To overcome this, the mesh was divided into two separate meshes: an inner mesh that had a relatively high nodal density and an outer mesh that had a relatively low nodal density. The origin was located at the same position for both meshes. The outer surfaces of the two meshes where the domains connected are defined as domain interfaces. The locations of the interfaces between the inner and outer domains were selected such that the impact on the computed fields was negligible. The geometry for the meshes is shown in Figure 4-1. Sample images of the meshes are found in Appendix A.

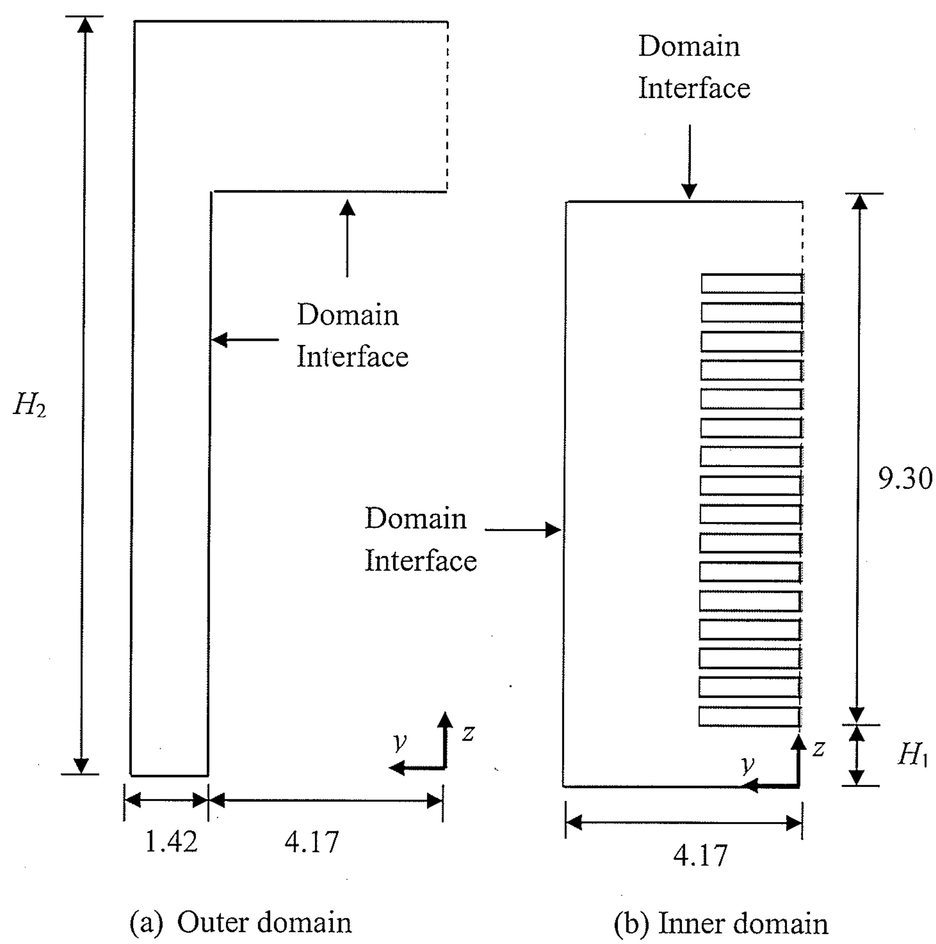

Figure 4-1: Inner and outer domain geometry.
Dimensions are in meters.

4.3: Overview of the Commercial Code Used

The commercial CFD code CFX-11 was used to solve the governing equations. The software is divided into Pre, Solve, and Post component programs.

CFX-Pre:

- Import the inner and outer mesh files from ANSYS ICEM CFD.
- Define the domain properties and boundary conditions.
- Define a domain interface between the inner mesh and the outer mesh.
- Define the initial solver parameters.
- Generate the definition file that is used by CFX-Solve.

CFX-Solve:

- Can interpolate an existing results file onto the definition file.
- Iteratively solves the governing equations at each node.
- GUI interface allows for the monitoring of the residuals and domain imbalances.
- The solver parameters can be modified at any point during the iterative process to improve convergence.

CFX-Post:

- GUI interface displays contours and streamlines.
- Data can be extracted from any location in the domain.

4.4: Numerical Method

The quantities at each node were solved iteratively until the maximum residuals for mass, *u*-momentum, *v*-momentum, *w*-momentum, and temperature were below 1.0E-05 at each node. Once this was achieved, the results were considered to be converged.

The values at each node were set by default to zero at the start of a numerical run. An existing results file can be interpolated onto a definition file and the results from the previous run can be used as an initial guess. This was done when the boundary conditions and geometry were relatively similar between the cases and this technique would in general reduce the time required to reach convergence.

A typical numerical run would take approximately two days to reach convergence using 8 CPUs. This execution time varied from one case to another. It was found that there was no trend that could be used to predict the time required for convergence. During a typical numerical run, the residuals may oscillate or become relatively constant. To overcome this poor convergence behaviour, two solver parameters (model relaxation coefficient and relaxation factor) were varied. The model relaxation coefficient has a default value of 1.0, and it was reduced successively to a value as low as 1.0×10^{-3}. The relaxation factor has a default value if 0.75, and it was reduced successively to a value as low as 1.0×10^{-5}. All converged solutions satisfied the overall mass and energy balances to close tolerances. The time step was fixed at 0.5 [s]. Plots of the convergence of the max residuals are presented in Appendix B for a typical numerical run.

4.5: Grid Independence Tests

In general, the accuracy of the results obtained from a converged numerical solution is dependent on the nodal density of the mesh. Grid independence tests were performed by comparing meshes of increasing nodal density. The purpose of these tests was to determine the nodal density required so that the converged results would not significantly change if the number of nodes was increased further. In this section, the grid independence tests from the mesh used to represent the domain for VH42 will be presented. Researcher Ahmed El-Shaboury conducted extensive grid independence tests on the mesh that will be used in this thesis for the domain in VH41.

Coarse, medium, and fine meshes were compared. The total number of nodes in each grid is summarized in Table 4-1. Significantly more nodes were located in the core mesh region relative to the outer mesh region.

Table 4-1: Number of nodes for coarse, medium, and fine meshes (VH42)

	Coarse	Medium	Fine
Outer	161,490	445,499	683,109
Core	901,000	2,251,108	3,720,208
Total	1,062,490	2,706,607	4,403,317

When conducting grid independence tests, aside from nodal density, all other parameters were held constant. The parameters L_x, L_y, P_y, and θ were set at 0.545 [m], 0.48 [m], 2.68 [m], and 83.5°, respectively. To compare the differences between two separate meshes, a result file from a low density mesh was interpolated, using CFX-solve, onto a result file from a higher density mesh. The difference at each spatial point for all variables was generated. The interpolated differences between the coarse and medium meshes will be referred to as coarse/med. The interpolated differences between the medium and fine meshes will be referred to as med/fine. In general, increasing the nodal density of a mesh will increase the time required to obtain converged results. The computational time required for the coarse, medium, and fine meshes summarized in Table 4-1 to converge was 19.43, 41.13, and 97.22 hrs, respectively.

The absolute maximum domain differences for the temperature and the velocity components between the coarse/med meshes and the med/fine meshes are shown in Table 4-2.

Table 4-2: Maximum domain differences between meshes

	coarse/med	med/fine
Max ΔT [°C]	28.41	5.17
Max Δu [m/s]	0.521	0.044
Max Δv [m/s]	0.455	0.166
Max Δw [m/s]	0.286	0.064

Increasing the nodal density significantly reduced the maximum domain differences between the meshes. The maximum difference in temperature between the med/fine meshes is relatively large at 5.17°C and by itself this value would indicate that grid independence has not been achieved with the medium mesh.

The percentage of the domain volume that contains all nodes with a certain temperature difference is shown in Table 4-3 and Figure 4-2. The nodes that have an interpolated temperature difference between the med/ fine mesh that is greater than 0.1°C occupy 1.31% of the domain volume. This volume is shown in Figure 4-3 and is located only in the proximity of the tower and within the gaps.

Table 4-3: Percentage of the total volume of the domain occupied by a certain temperature difference (comparing coarse/med and med/fine meshes)

	% of total domain volume	
	coarse/med	med/fine
$\lvert\Delta T\rvert > 0.1°C$	$3.48x10^{-1}$	$1.31x10^{-2}$
$\lvert\Delta T\rvert > 0.5°C$	$2.32x10^{-2}$	$1.63x10^{-3}$
$\lvert\Delta T\rvert > 1°C$	$1.40 x10^{-2}$	$4.76x10^{-4}$
$\lvert\Delta T\rvert > 3°C$	$4.55x10^{-3}$	$1.88x10^{-5}$
$\lvert\Delta T\rvert > 5°C$	$2.96x10^{-3}$	$2.20x10^{-7}$
$\lvert\Delta T\rvert > 10°C$	$2.08x10^{-3}$	0
$\lvert\Delta T\rvert > 20°C$	$5.63x10^{-4}$	0
$\lvert\Delta T\rvert > 28 °C$	$9.92x10^{-8}$	0

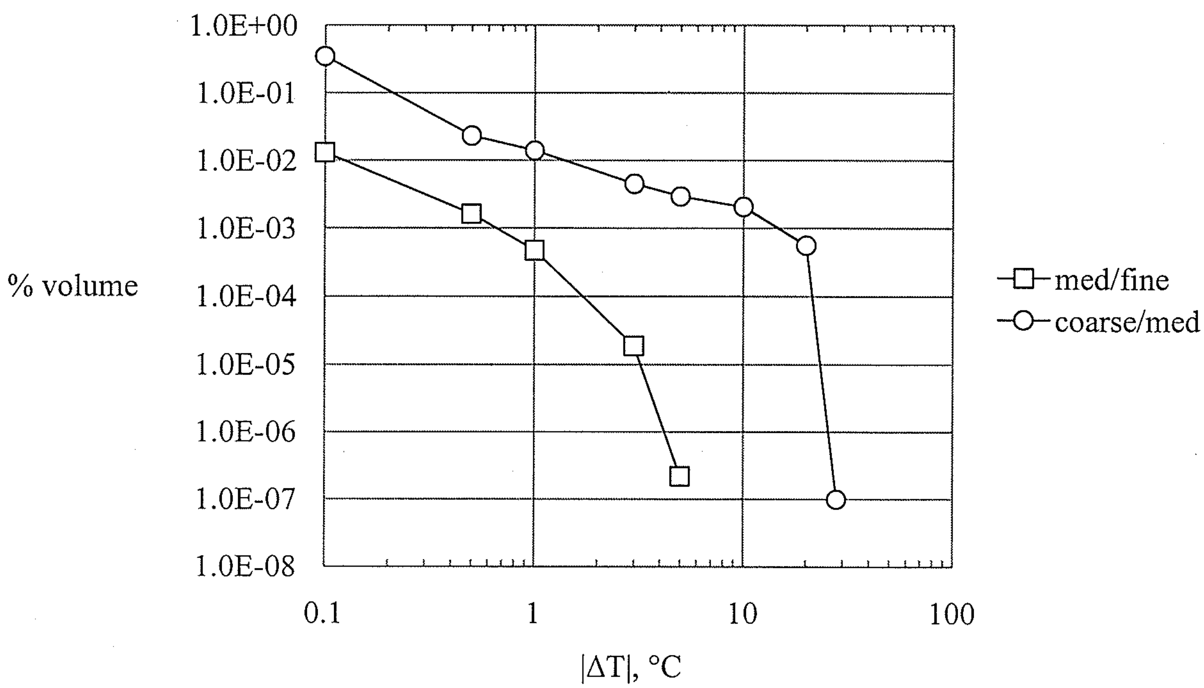

Figure 4-2: Percentage of the total volume of the domain occupied by a certain temperature difference (comparing coarse/med and med/fine meshes)

The volume that contains an interpolated temperature difference greater than 5°C between the med/fine mesh is 2.20×10^{-7} percent of the total volume. Since the volume with the large temperature difference is very small relative to the actual size of the domain, having a maximum temperature difference of 5.17°C between the med/fine mesh was considered to be acceptable. Similar trends were observed for the velocity components.

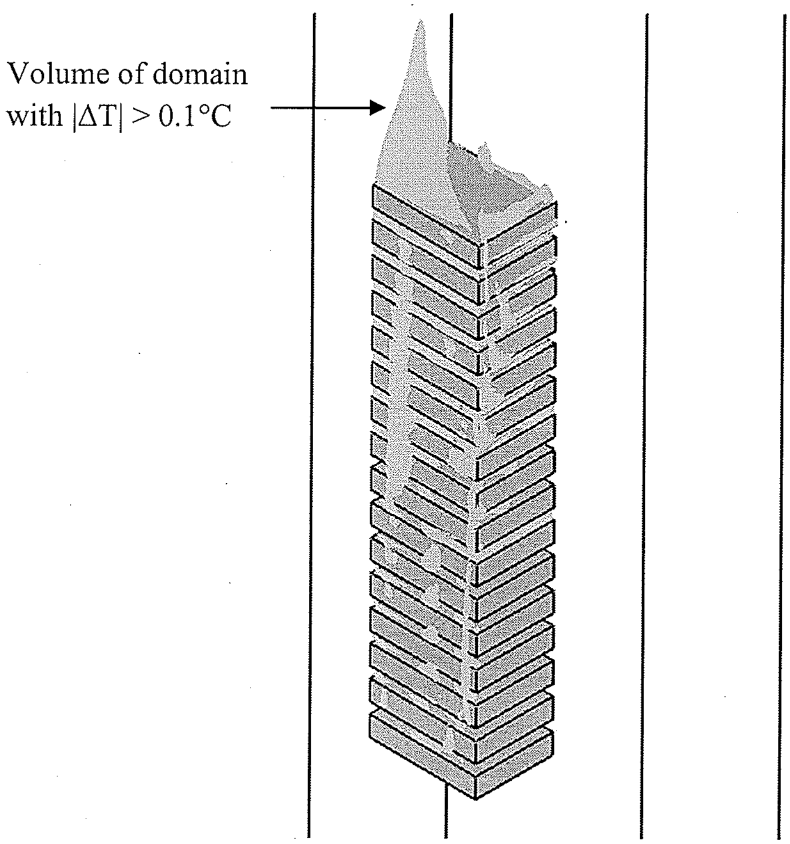

Figure 4-3: Volume of domain occupied by a temperature difference greater than 0.1°C (med/fine meshes)

Since a majority of the difference in temperature between the meshes occurs within the tower gaps, the maximum difference in the temperature within the volume of a tower gap, $\Delta T_{g,max}$ will be compared. In total there are fifteen gaps and $\Delta T_{g,max}$ is shown for each gap in Figure 4-4 for the coarse/med meshes and a med/fine meshes. For the coarse/med meshes, thirteen gaps had $\Delta T_{g,max}$ values greater than 1°C and three gaps have $\Delta T_{g,max}$ values greater than 10°C. For the interpolated med/fine results all fifteen gaps have a maximum temperature difference less than 0.42°C and eight gaps have a maximum temperature difference less than 0.07°C.

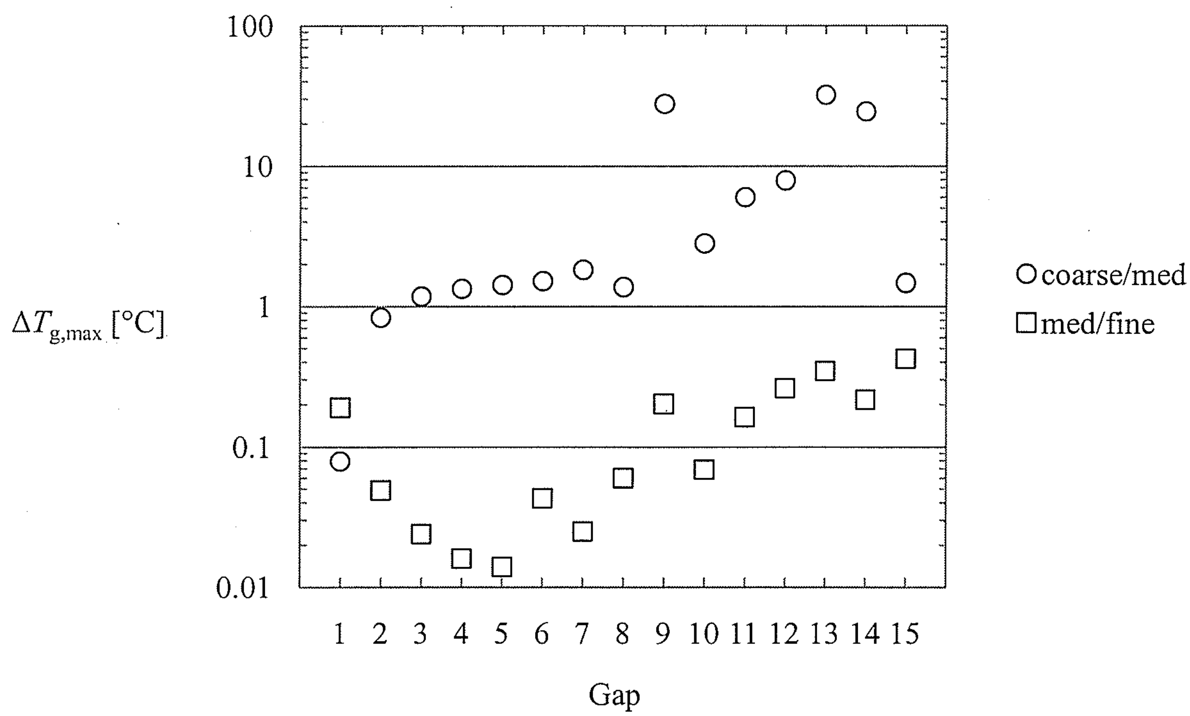

Figure 4-4: $\Delta T_{g,max}$ for all tower gaps (coarse/med and med/fine meshes)

From the above discussion it can be concluded that the differences between the medium and fine meshes are reasonably small. Therefore, the medium mesh defined in Table 4-1 will be used for all cases involving VH42. Similar analysis was done to determine a suitable mesh for VH41. A mesh of 2,066,209 nodes was used for VH41.

4.6: Resolution of the Turbulent Boundary Layer

To resolve the turbulent boundary layer the mesh was refined near the solid surfaces of the gaps. It is required that the y^+ values on the surfaces within the gap be less than 100. For the medium mesh used for VH42, the value for n was 0.0038 [m] and the nodes expanded away from the walls at a ratio of 1.125. The maximum and average values for y^+ within the gaps were 29.95 and 4.68, respectively. The refinement of the grid near the gap walls resulted in a high nodal density within the gaps. The gaps occupy 2.5% of the total domain volume but 14.1% of the nodes were located within the gaps. Similar trends were observed for the mesh used in the analysis of VH41.

4.6: Turbulent Intensity at the Inlet

Berg (2006) investigated the effect of varying the turbulent parameters at the inlet. The turbulence intensity at the inlet was varied from 2.5% to 5% to 10% with the viscosity ratio held constant. The viscosity ratio was varied from 5 to 10 to 20 with the turbulence intensity held constant. It was observed that for all cases, the maximum domain temperature varied by less than 0.4%. As a result, the turbulence intensity and viscosity ratio were left at the default values of 5% and 10 in the present investigation.

CHAPTER 5: RESULTS AND DISCUSSION

5.1: Introduction

This chapter will focus on how varying the domain parameters can influence the effectiveness of the ventilation system. An effective cooling strategy will be determined for both VH41 and VH42. The criterion of having the maximum surface temperature of the tower below 60°C will be used for the study. The following parameters will be varied to achieve this:

- The inlet geometry parameters L_x and L_y.
- The inlet location parameter P_y.
- The location on the tower that the jet is aimed at, given by the angle θ.

In VH41, the tower elevation is 1.05 [m] above the ground; cases with this tower elevation will be referred to as the low tower. The tower located in VH42 is elevated 3.52 [m] above the ground; cases with this tower elevation will be referred to as the high tower. These are the two tower elevations that will be studied.

The inlet jet angle θ required to hit a particular desired location on the tower will vary depending on the location of the inlet and the tower's elevation above the ground. The geometry of the jet target path for both tower elevations is shown in Figure 5-1.

The parameter β will define the location that the jet is aimed at the tower and it can be calculated as:

$$\beta = \frac{\text{tower target location}}{\text{tower height}} = \frac{A}{7.98} \tag{5.1}$$

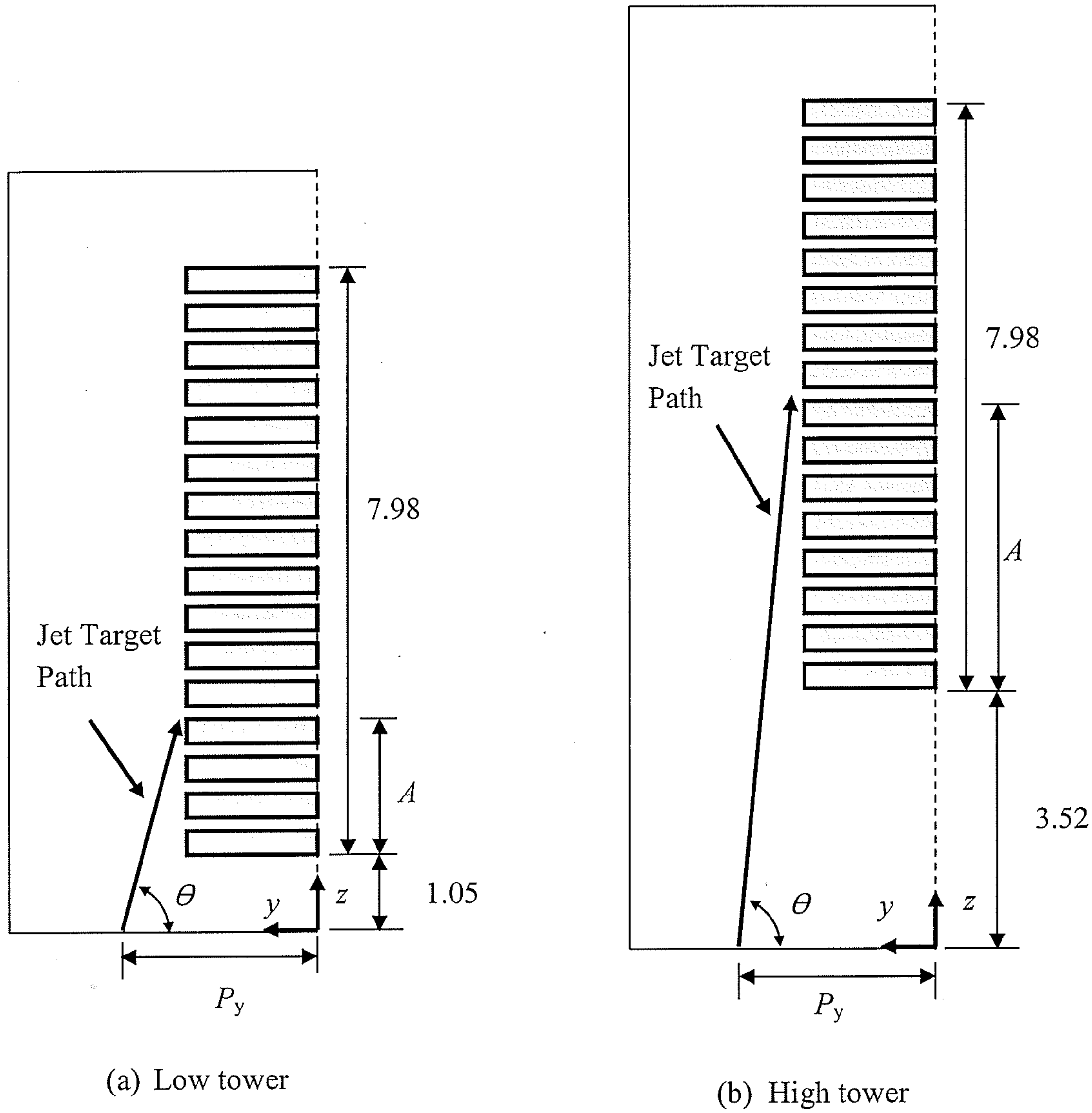

Figure 5-1: Side view showing example jet targets path for the high and low towers. Dimensions are in meters.

The results from the base inlet geometry and base inlet location will be presented in Section 5.2. In Section 5.2.2, a detailed account will be given in of the ventilation design currently employed in VH41 and VH42. These cases will serve as the basis against which all other cases will be evaluated. The design goal is to increase the interaction of air with the tower. The effect that the parameter β has on the tower ventilation will be determined in Section 5.2.3 for both the high tower and the low tower. Recommendations will be made regarding where the jet should be aimed and it will be observed how changing the tower elevation above the ground affects the ventilation.

The effect of inlet geometry will be presented in Section 5.3. The results from varying the inlet geometries parameters L_x and L_y will be discussed in Sections 5.3.1 and 5.3.4. The effect that β has on the tower ventilation for different inlet geometries will be discussed in Sections 5.3.2 and 5.3.3. It will be determined what impact the geometry of the inlet has on the ventilation system.

The effect of inlet location will be presented in Section 5.4. The inlet will be moved closer to the tower in Section 5.4.1. In Section 5.4.2 the inlet will be moved away from the tower and the effect of varying β will be presented for both the high and low towers. The inlet position parameter P_y will be varied to change the location of the inlet. It will be determined how the location of the inlet affects the effectiveness of the ventilation system.

A correlation between the amount of airflow entering a tower gap and the maximum temperature within that gap will be presented in Section 5.5.

The mass flow rate entering the domain from the inlet, the location and size of the outlet, and the tier heat flux will be fixed for all cases. A summary of all the cases studied is presented in Table 5-1.

Table 5-1: Summary of studied cases

Case	Tower Type	θ [deg]	β	Inlet Description	Inlet Position [m]	Inlet Dimensions [m]	
					P_y	L_y	L_x
1	High	77.4	0.06	Base inlet location, base inlet geometry * indicates existing cases for VH41 and VH42	2.68	0.48	0.545
* 2	Low	60					
* 3	High	90	N/A				
4	Low						
5	High	80.7	0.25				
6	Low	70					
7	High	83.2	0.51				
8	Low	80					
9	High	84.5	0.73				
10	Low	82.5					
11	High	85.4	0.95				
12	Low	84					
13	High	77.4	0.06	Base inlet location, 0.5 inlet, varying L_x	2.68	0.48	0.273
14	Low	60					
15	High	80.7	0.25				
16	Low	70					
17	High	83.2	0.51				
18	Low	80					
19	High	84.5	0.73				
20	Low	82.5					
21	High	85.4	0.95				
22	Low	84					
23	High	77.4	0.06	Base inlet location, 0.25 inlet, varying L_x	2.68	0.48	0.136
24	Low	60					
25	High	80.7	0.25				
26	Low	70					
27	High	83.2	0.51				
28	Low	80					
29	High	85.4	0.95				
30	Low	84					

Table 5-1: Continued

Case	Tower Type	θ [deg]	β	Inlet Description	Inlet Position [m]	Inlet Dimensions [m]	
					P_y	L_y	L_x
31	High	83.2	0.51	Base inlet location, 1.25 inlet, varying L_x	2.68	0.48	0.681
32	High	83.2	0.51	Base inlet location, 0.5 inlet, varying L_y		0.24	0.545
33	High	83.2	0.51	Base inlet location, 0.25 inlet, varying L_y		0.12	
34	High	83.2	0.51	Base inlet location, 0.5 inlet, varying L_y and L_x		0.339	0.385
35	High	83.2	0.51	Base inlet location, 0.25 inlet, varying L_y and L_x		0.24	0.273
36	High	68.0	0.06	Far from tower, 0.25 inlet, varying L_x	3.41	0.48	0.136
37	Low	43.7					
38	High	73.6	0.25				
39	Low	62.0					
40	High	77.9	0.51				
41	Low	72.3					
42	High	80.1	0.73				
43	Low	76.6					
44	High	81.6	0.95				
45	Low	79.3					
46	Low	83.2	0.51	Close to tower, various inlet sizes	2.39	0.48	0.545
47	Low						0.273
48	Low						0.136

5.2: Evaluation of the Base Inlet Conditions

The following section will present the results for the base inlet geometry and the base inlet location. This geometry is currently utilized in VH41 and VH42 and will be referred to as the base inlet conditions. A top view of the dimensions for the base inlet conditions is shown in Figure 5-2. In Section 5.2.1, a detailed discussion will be presented of the ventilation designs currently utilized in VH41 and VH42. In Section 5.2.2, the effect that varying β has on the tower ventilation will be presented for both the high tower and the low tower. A comparison of the two tower elevations will be presented in Section 5.2.3.

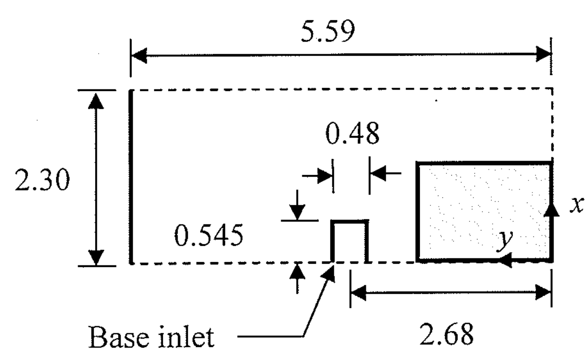

Figure 5-2: Top view of domain showing the base inlet conditions. Dimensions are in meters.

5.2.1: Existing Ventilation Designs Utilized in VH41 and VH42

The following section will discuss the ventilation designs that are currently utilized in VH41 and VH42. Before recommendations can be made regarding improving the ventilation, it is important to understand the performance of the existing design.

5.2.1.1: VH41, Jet Angled at 60°, Case 2

Currently in VH41, the jet is angled at 60°. This corresponds to a β of 0.06 and the jet target path centered on Gap 1. To analyze the effectiveness of the design, the air flow and temperature conditions that occur within the fifteen tower gaps will be discussed. The tier surface temperatures above the criterion of 60°C only occur on the top and bottom horizontal faces of a gap. The maximum and average surface temperatures on the outer faces of the tiers are 54.2°C and 30.5°C, respectively. Since the temperatures on the outer surfaces are relatively low, they will be excluded from any further analysis and discussion.

The nomenclature for the mass flow rates and bulk temperature for a typical tower gap using a top view are shown in Figure 5-3. Plane P1 is a vertical plane touching the tower surfaces facing the inlet and plane P2 is a vertical plane touching the tower surfaces facing away from the inlet. Airflow can enter or exit a gap through planes P1 and P2 while symmetry planes S1 and S3 are impermeable.

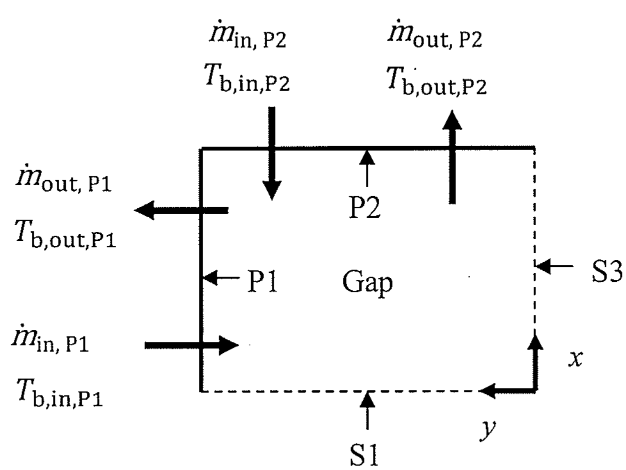

Figure 5-3: Top view of the mass flow rates and bulk temperatures for a typical tower gap

The mass flow rate is conserved within the gap, as shown in the equation below.

$$\dot{m}_{\mathrm{in,P1}} - \dot{m}_{\mathrm{out,P1}} + \dot{m}_{\mathrm{in,P2}} - \dot{m}_{\mathrm{out,P2}} = 0 \tag{5.2}$$

The net mass flow rate at a gap plane is defined by the equation below.

$$\dot{m}_{\mathrm{g,net}} = |(\dot{m}_{\mathrm{in}} - \dot{m}_{\mathrm{out}})| \tag{5.3}$$

The net mass flow rates on planes P1 and P2, as calculated by the code, were different because of interpolation errors. The maximum deviation in any gap was always less than 0.12% of the inlet mass flow rate. Therefore, the net mass flow rate through a gap was taken as the average of the net mass flow rates on planes P1 and P2. The percent net mass flow rate can be calculated as:

$$\%\dot{m}_{\mathrm{g,net}} = \frac{|(\dot{m}_{\mathrm{in,P1}} - \dot{m}_{\mathrm{out,P1}})| + |(\dot{m}_{\mathrm{in,P2}} - \dot{m}_{\mathrm{out,P2}})|}{2} \frac{100}{\dot{m}_{\mathrm{o}}} \tag{5.4}$$

Energy is conserved within a gap, as shown in the equation below.

$$\dot{E}_{\mathrm{in}} - \dot{E}_{\mathrm{out}} + \dot{E}_{\mathrm{gen}} = 0 \tag{5.5}$$

Where:

$$\dot{E}_{\mathrm{in}} = C_p \dot{m}_{\mathrm{in,P1}} T_{\mathrm{b,in,P1}} + C_p \dot{m}_{\mathrm{in,P2}} T_{\mathrm{b,in,P2}} \tag{5.6}$$

$$\dot{E}_{\mathrm{out}} = C_p \dot{m}_{\mathrm{out,P1}} T_{\mathrm{b,out,P1}} + C_p \dot{m}_{\mathrm{out,P2}} T_{\mathrm{b,out,P2}} \tag{5.7}$$

$$\dot{E}_{\mathrm{gen}} = A_{s,g} q'' \tag{5.8}$$

The energy generated from the gap surfaces is removed through two methods:

- Forced convection resulting from the ventilation system
- Free convection resulting from buoyancy effects.

The maximum temperature that occurs on the surfaces within each tower gap will be defined as $T_{g,max}$.

The profiles of $\%\dot{m}_{g,net}$ and $T_{g,max}$ at all tower gaps in Case 2 are shown in Figure 5-4. The highest $\%\dot{m}_{g,net}$ occurs at Gap 1, this corresponds to the location on the tower that the air jet was aimed at. The $\%\dot{m}_{g,net}$ steadily decreases after Gap 1 and reaches a value below 2 at Gap 10. From Gaps 10 to 15, $\%\dot{m}_{g,net}$ stays below 2. The tower gaps have $T_{g,max}$ values that are below 60°C from Gap 1 to Gap 9. From Gaps 10 to 15 the value of $T_{g,max}$ is above 60°C. The lowest $T_{g,max}$ value occurs at Gap 1, which corresponds with the gap with the highest value for $\%\dot{m}_{g,net}$. At Gap 2 there is a relatively large decrease of 10.3 in $\%\dot{m}_{g,net}$, relative to Gap 1, but a relatively small increase of 3.4°C in $T_{g,max}$. At Gap 10 $\%\dot{m}_{g,net}$ decreases by only 1.7 relative to Gap 9, while $T_{g,max}$ increases significantly by 29.2°C. It appears that there is a threshold value for $\%\dot{m}_{g,net}$. If $\%\dot{m}_{g,net}$ is below the threshold, the gap surface temperatures will be relatively high. Once the threshold value is crossed, $T_{g,max}$ will decrease sharply. Increasing $\%\dot{m}_{g,net}$ significantly beyond the threshold value will not proportionately reduce $T_{g,max}$.

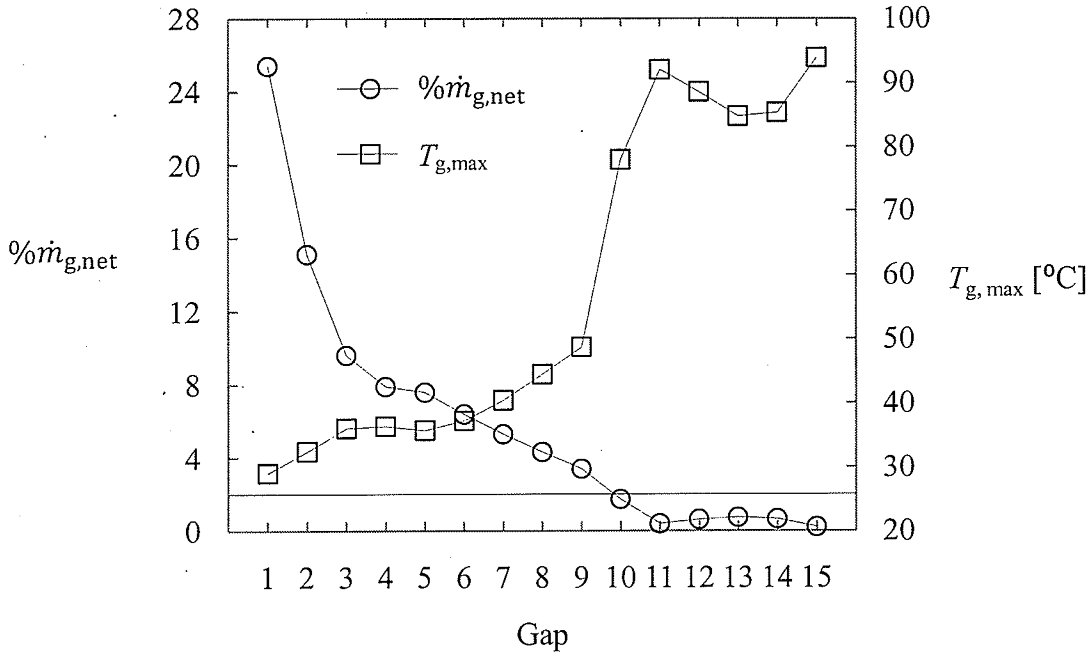

Figure 5-4: $\%\dot{m}_{g,net}$ and $T_{g,max}$ for all tower gaps (Case 2)

The streamlines entering Gap 6 on plane P1 are shown in Figure 5-5. These streamlines were traced by massless particles that tracked the path that the airflow takes. The streamlines enter Gap 6 directly from the inlet, flow all the way into the gap, and exit on the far side of plane P2. The streamlines show this behavior from Gaps 1 to 9. These are the gaps that have relatively low $T_{g,max}$ values in the range of 29.0°C to 48.7°C and relatively high $\%\dot{m}_{g,net}$ values in the range of 3.4 to 25.4. The streamlines that exhibit the behavior where they completely penetrate a tower gap will be referred to as type 1. The primary means of heat removal for these gaps is forced convection. The streamlines entering Gap 9 on plane P1 are shown in Figure 5-6; this is the highest tower gap that has type 1 streamlines. At this gap the values for $\%\dot{m}_{g,net}$ and $T_{g,max}$ are 3.4 and 48.7°C, respectively. The streamlines entering Gap 10 on plane P1 are shown in Figure 5-7. The streamlines enter Gap 10 directly from the inlet, flow approximately half way into the gap, and exit on the near side of plane P2. In this case, only one tower gap had streamlines that behaved in this way. The value for $T_{g,max}$ at Gap 10 is moderately high at 77.9°C and the value for $\%\dot{m}_{g,net}$ is moderately low at 1.7. Gap streamlines that exhibit the behavior where they moderately penetrate a tower gap will be referred to as type 2. At these gaps the airflow is transitioning between where forced convection is the dominant means of heat removal and where free convection is the dominant mode.

The streamlines entering Gap 12 on plane P1 are shown in Figure 5-8. The streamlines barely penetrate into the gap, and exit on plane P1. After the streamlines exit Gap 12, they enter the three gaps above it. The streamlines show this type of behavior from Gaps 11 to 15. This corresponds with the gaps that have relatively high $T_{g,max}$ values in the range of 84.7°C to 93.8°C and relatively low $\%\dot{m}_{g,net}$ values in the range of 0.2 to 0.7. Gap streamlines that exhibit this behavior will be referred to as type 3. The primary means of heat removal in these gaps is free convection.

From the above discussion it can be concluded that when $\%\dot{m}_{g,net}$ is above the threshold value of 2, the airflow will completely penetrate a tower gap and $T_{g,max}$ will be relatively low. When $\%\dot{m}_{g,net}$ drops below the threshold value of 2, the jet velocity is not strong enough to push the airflow completely into a gap and $T_{g,max}$ will increase above 60°C. For the existing conditions in VH41, the ventilation system adequately cools the bottom nine gaps but misses the top six gaps. Any design modifications to the ventilation system should be done with the intent to increasing $\%\dot{m}_{g,net}$ above 2 for Gaps 10 to 15. A design modification that further increases $\%\dot{m}_{g,net}$ for gaps 1 to 9 will have minimal benefit to the tower ventilation, since these gaps are already adequately penetrated by airflow.

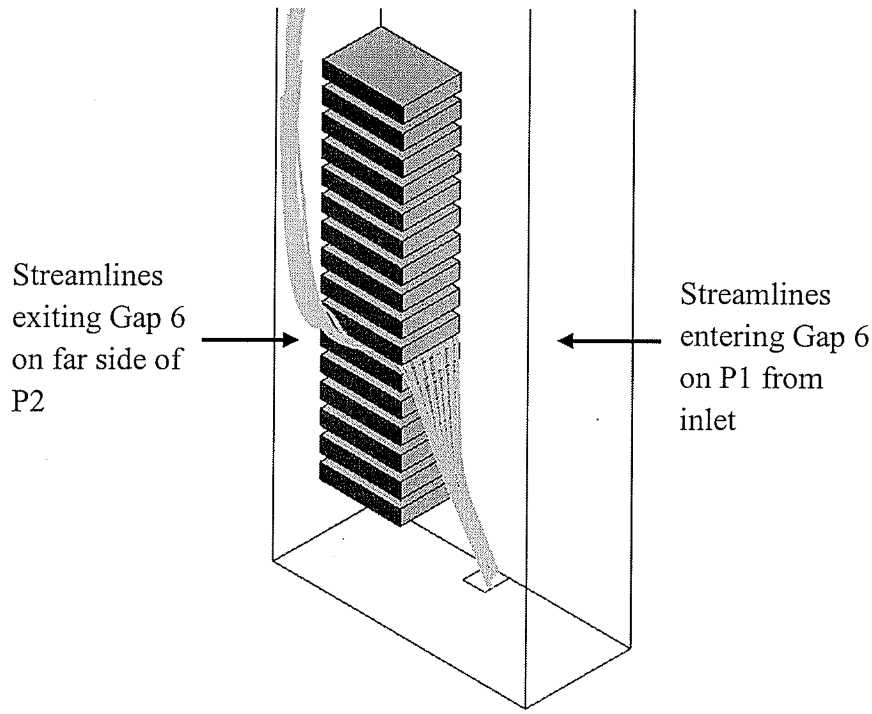

Figure 5-5: Type 1 streamlines entering Gap 6 on plane P1 (Case 2)

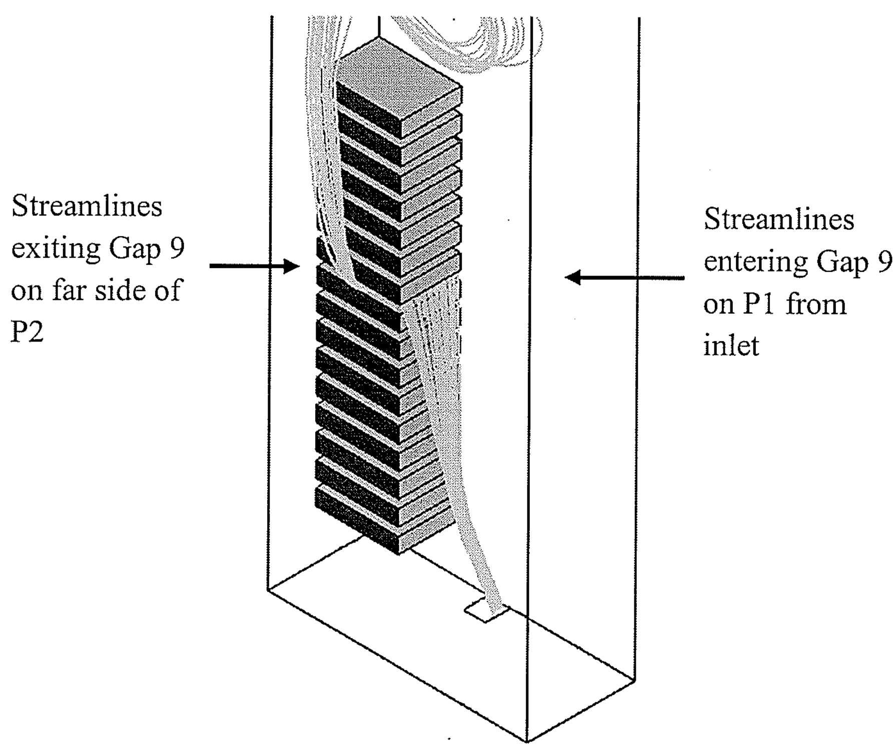

Figure 5-6: Type 1 streamlines entering Gap 9 on plane P1 (Case 2)

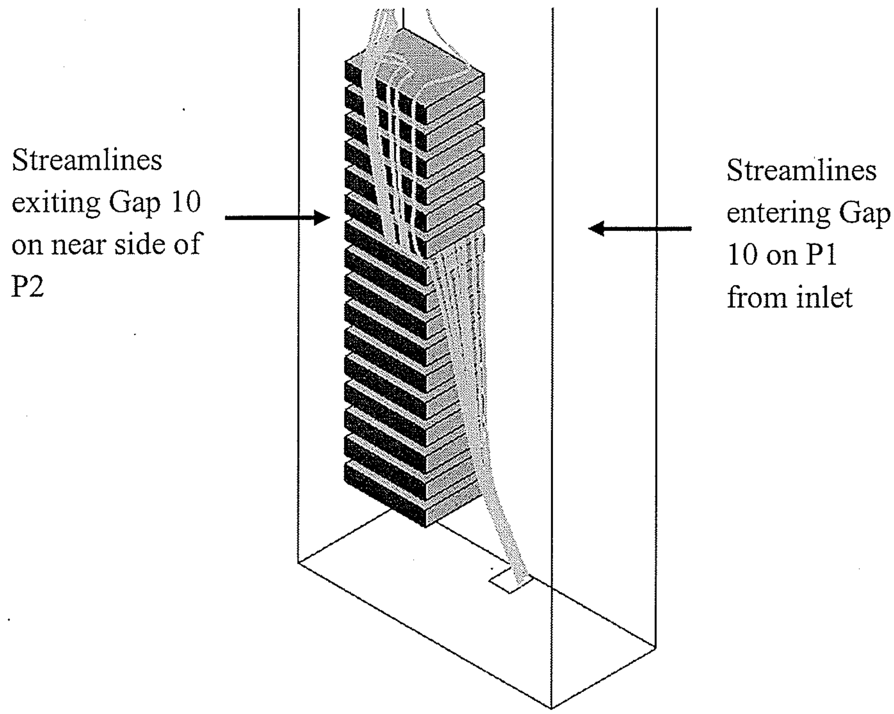

Figure 5-7: Type 2 streamlines entering Gap 10 on plane P1 (Case 2)

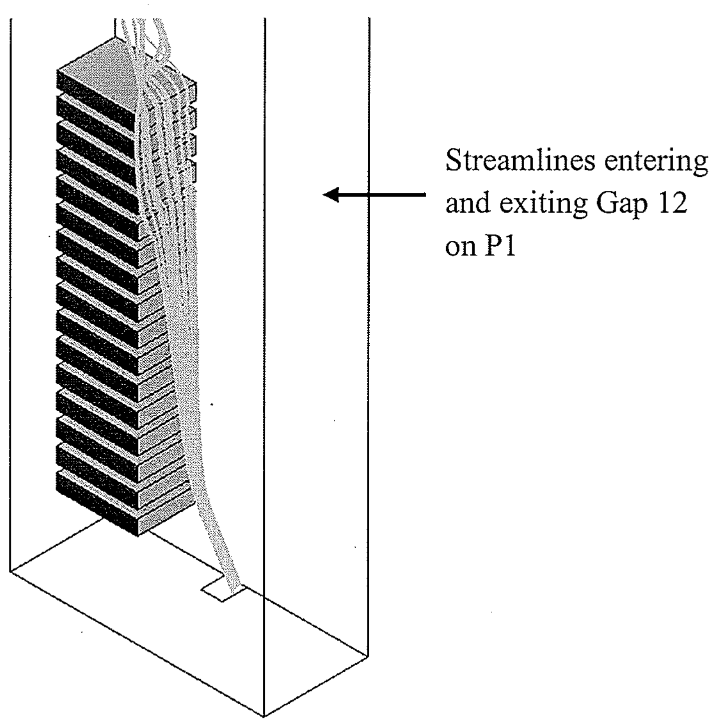

Figure 5-8: Type 3 streamlines entering Gap 12 on plane P1 (Case 2)

5.2.1.2: VH42, Jet Angled at 90°, Case 3

In VH42 the air jet is currently angled at 90°; at this angle the jet target path misses the tower. The profiles for $\%\dot{m}_{\mathrm{g,net}}$ and $T_{\mathrm{g,max}}$ at each gap is shown in Figure 5-9. For all tower gaps, $\%\dot{m}_{\mathrm{g,net}}$ is relatively low in the range of 0.01 to 1.7 and $T_{\mathrm{g,max}}$ is relatively high in the range of 73.2°C to 87.4°C.

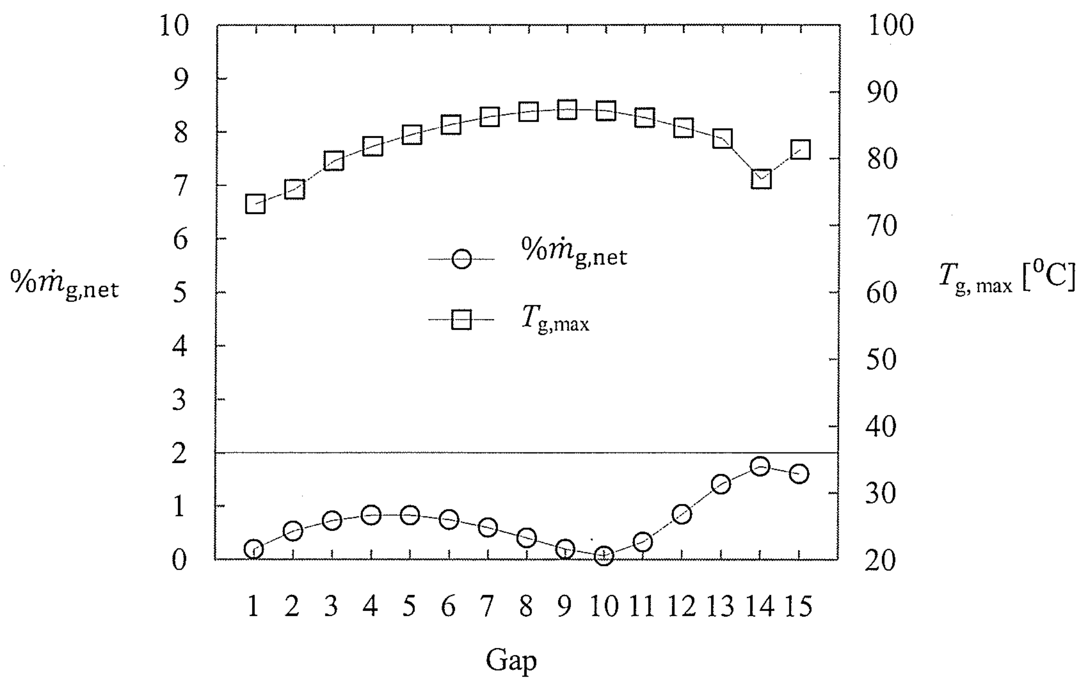

Figure 5-9: $\%\dot{m}_{\mathrm{g,net}}$ and $T_{\mathrm{g,max}}$ for all tower gaps (Case 3)

The streamlines entering all tower gaps show the characteristics of type 3 streamlines, where the streamlines do not significantly penetrate a gap. The streamlines entering Gap 10 on plane P1 are shown in Figure 5-10. The streamlines flow vertically up from the inlet, circulate within the domain, flow into Gap 10 on plane P1, and then exit the gap on plane P1 without significantly penetrating the gap.

When the jet is aimed vertically at 90°, the airflow circulates around the tower without significantly penetrating any of the tower gaps. This results in all gaps having $T_{g,max}$ values above 60°C.

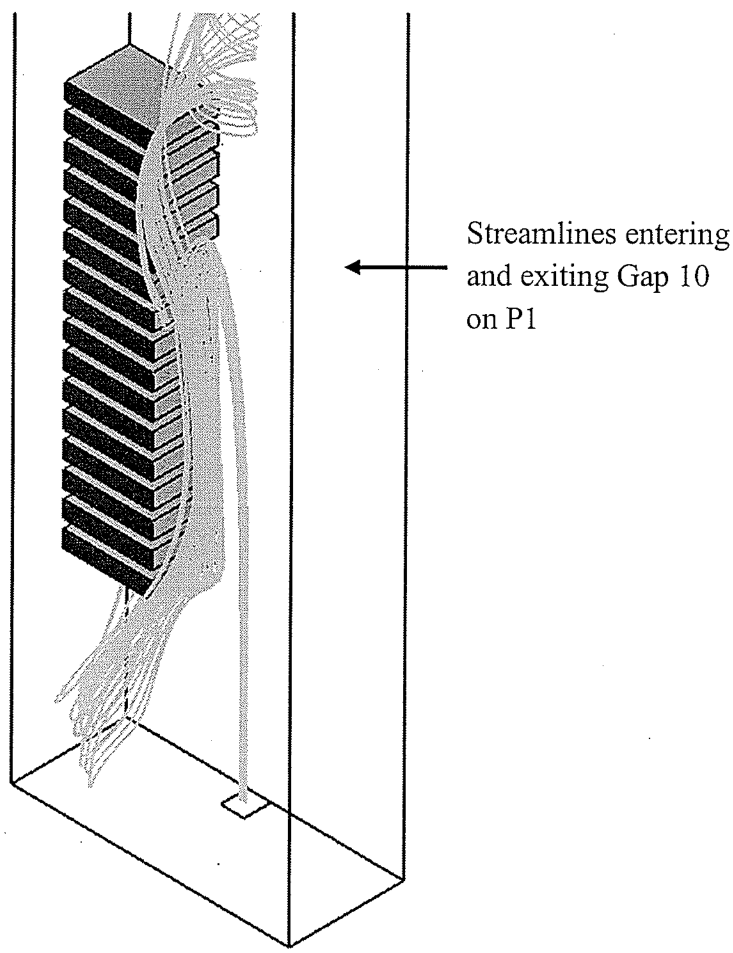

Figure 5-10: Type 3 streamlines entering Gap 10 on plane P1 (Case 3)

5.2.2: The Effect of β for the Base Inlet Conditions, Cases 1 to 12

In the following section the effect of varying β will be presented for the base inlet conditions. The results for the high and low towers will be presented separately and the section will be concluded with a comparison between the high tower and low tower.

5.2.2.1: The Effect of β for the High Tower, Cases 1, 5, 7, 9, and 11

The following section will present the results for the high tower using the base inlet conditions. The $\%\dot{m}_{\mathrm{g,net}}$ at each tower gap for Cases 1, 5, 7, 9, and 11 is shown in Figure 5-11. The jet inlet angle was varied from 77.4° to 85.4° for these cases. Irrespective of where the jet is aimed on the tower, $\%\dot{m}_{\mathrm{g,net}}$ for the top six gaps is always below 2. The jet velocity decays as it moves from the inlet to the tower. The distance to reach the top six gaps is large enough to decay the jet velocity to the point where it is not strong enough to significantly push airflow into the gaps. The streamlines entering the top six gaps always show the characteristics of type 2 or type 3. The streamlines entering the bottom six gaps always show the characteristics of type 1 streamlines, irrespective of β. Varying the parameter β will effect whether Gaps 7 to 9 have $\%\dot{m}_{\mathrm{g,net}}$ values above 2. The greatest number of gaps with $\%\dot{m}_{\mathrm{g,net}}$ values above 2 occurs when β is 0.25. At this β, nine gaps receive sufficient airflow. Increasing the value of β beyond 0.25 reduces the $\%\dot{m}_{\mathrm{g,net}}$ values for Gaps 1 to 9, but does not improve the $\%\dot{m}_{\mathrm{g,net}}$ values for Gaps 10 to 15.

The $T_{\mathrm{g,max}}$ at each tower gap for Cases 1, 5, 7, 9, and 11 is shown in Figure 5-12. Aside from a single gap from Case 5, when a gap has a $\%\dot{m}_{\mathrm{g,net}}$ value above 2, the value for $T_{\mathrm{g,max}}$ will drop below 60°C.

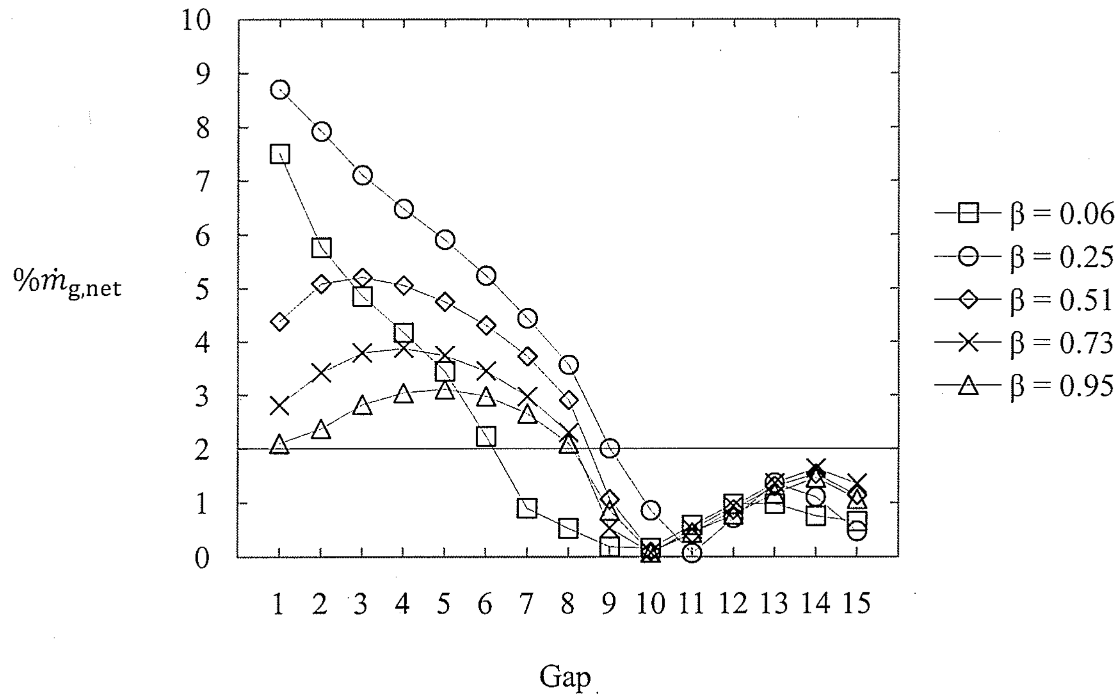

Figure 5-11: $\%\dot{m}_{g,net}$ for all tower gaps (Cases 1, 5, 7, 9, and 11)

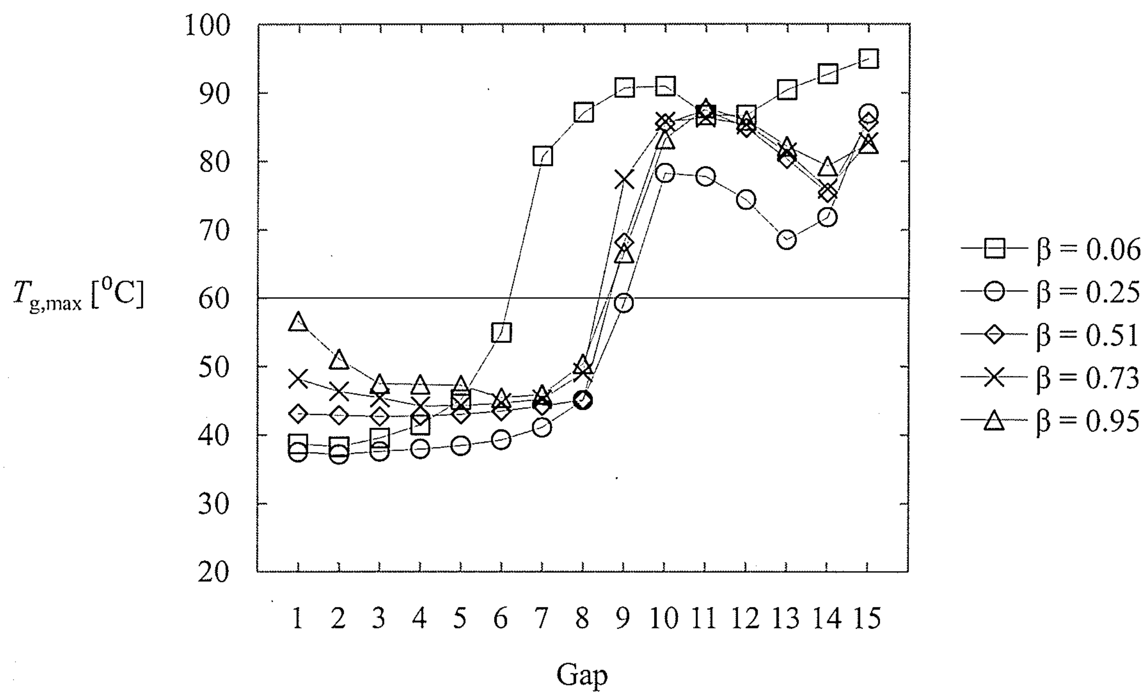

Figure 5-12: $T_{g,max}$ for all tower gaps (Cases 1, 5, 7, 9, and 11)

Plane P3 is defined as an x-z plane that is at x = 1.88 [m]. Its location and the direction from which contours will be viewed on the plane is shown in Figure 5-13.

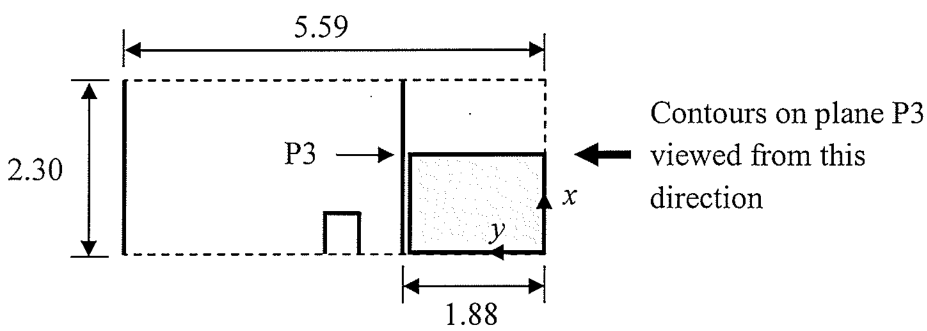

Figure 5-13: Top view of domain showing plane P3.
Dimensions are in meters.

The velocity of the airflow within the domain can be divided into components that are in the x-direction (u-velocity), y-direction (v-velocity), and z-direction (w-velocity). Since the gap planes P1 and P2 are vertical, only velocity components that are perpendicular to these planes will enter the gaps; on plane P1 only the v-velocity component will enter the gap and on plane P2 only the u-velocity component will enter the gap.

Contours of the v-velocity component on plane P3 are shown in Figure 5-14 for Cases 1, 5, and 11. These contours will qualitatively show the shape that the air jet takes 0.1 [m] in front of the tower. Where no contour is shown on plane P3, the $|v|$ is below 0.02 [$^{m}/_{s}$]. The location of the gap with the highest $\%\dot{m}_{g,net}$ and the tower target location are indicated on the contours.

When β is 0.06, the highest magnitude of $|v|$ occurs below the tower. This indicates that when the jet is aimed at a β of 0.06, a significant amount of the inlet airflow misses its intended target and flows beneath the tower. A contributing factor to this is that the airflow sinks because it is colder than the surrounding air in that region of the domain. In general, the farther the jet travels, the more the trajectory of the air jet sinks below the jet target location. At $\beta = 0.06$, the tower target location and the gap with the highest $\%\dot{m}_{g,net}$ both occur at Gap 1. The contour is qualitatively shown to fully cover Gaps 1 to 5 and partially cover Gap 6; this corresponds to the gaps that have relatively low $T_{g,max}$ values and relatively high $\%\dot{m}_{g,net}$ values.

For $\beta = 0.25$, the highest $|v|$ occurs at Gap 1 and below the tower. At this β, the corresponding tower target location is Gap 4, but the gap with the highest $\%\dot{m}_{g,net}$ is located three gaps below at Gap 1. The contour is qualitatively shown to cover more gaps relative to what was observed when β was 0.06 but the velocity has a weaker magnitude.

For $\beta = 0.95$ the corresponding tower target location is Gap 15. However, the gap with the highest $\%\dot{m}_{g,net}$ value is ten gaps lower at Gap 5. Despite aiming the air jet at the top of the tower only the bottom gaps are covered by the contour. The contour is qualitatively shown to have significantly reduced values of $|v|$ relative to when β was 0.06 and 0.25.

The streamlines entering Gap 7 on plane P1 for Cases 1 and 5 are shown in Figures 5-15 and 5-16, respectively. For $\beta = 0.06$ (case 1), the streamlines at Gap 7 show the characteristics of type 3. The values of $\%\dot{m}_{g,net}$ and $T_{g,max}$ at this gap are 0.9 and 80.7°C, respectively. Increasing β from 0.06 to 0.25 causes the streamlines at this gap to change to type 1, as shown in Figure 5-16. The value of $\%\dot{m}_{g,net}$ is increased to 4.4 and $T_{g,max}$ is reduced to 41.1°C. This demonstrates how varying β can influence the interaction of the ventilation system with the tower gaps.

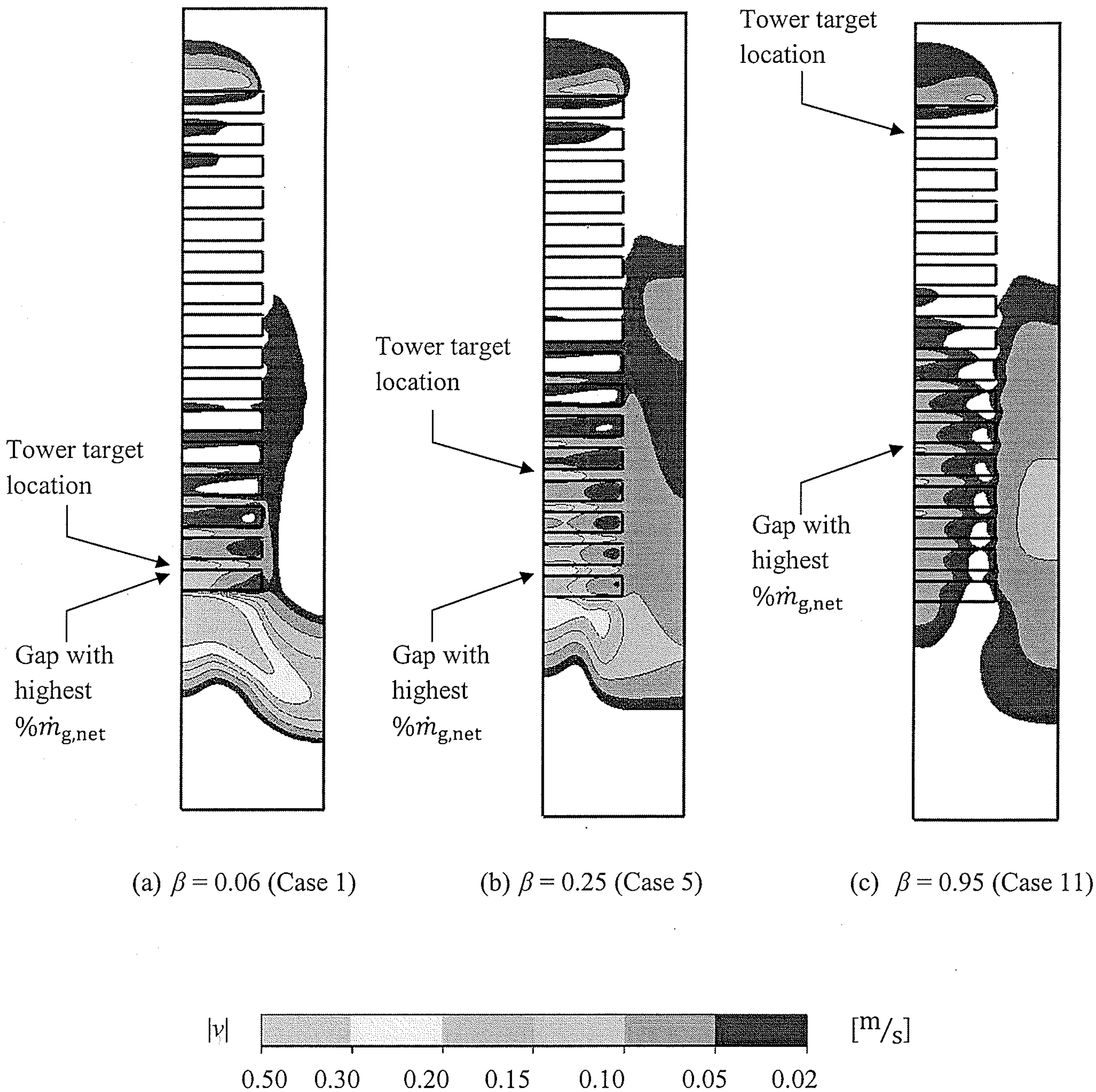

Figure 5-14: Contours of $|v|$ on plane P3 (Cases 1, 5, and 11)

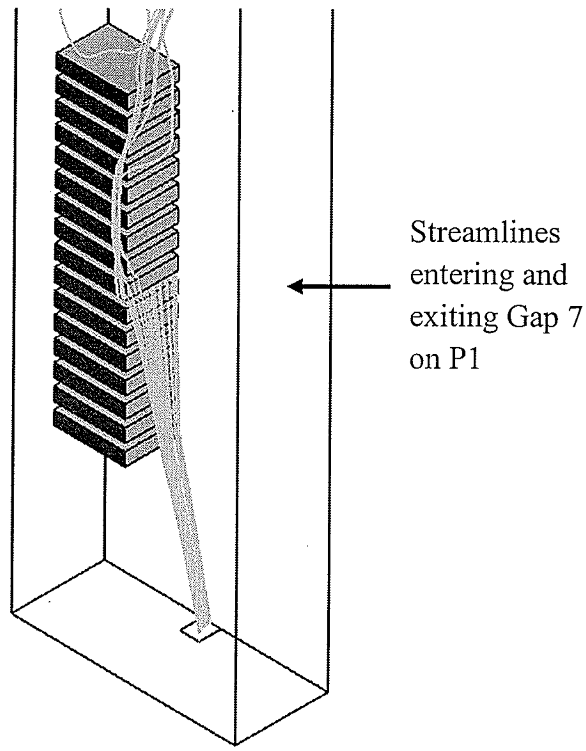

Figure 5-15: Type 3 streamlines entering Gap 7 on plane P1 (Case 1)

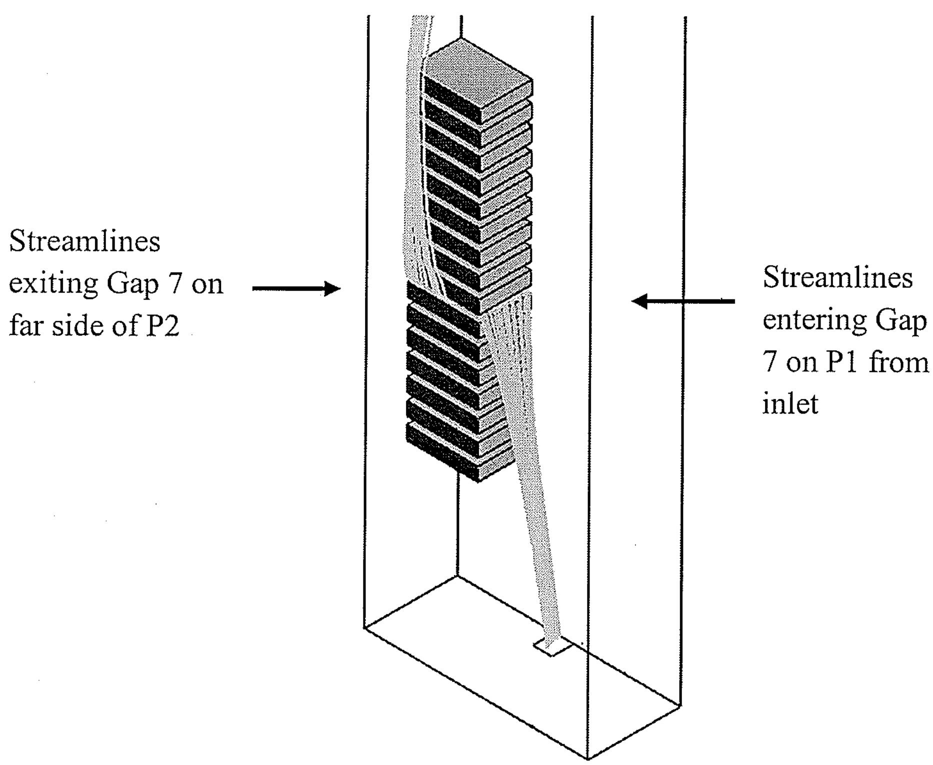

Figure 5-16: Type 1 streamlines entering Gap 7 on plane P1 (Case 5)

5.2.2.2: The Effect of β for the Low Tower, Cases 2, 6, 8, 10, and 12

The $\%\dot{m}_{\mathrm{g,net}}$ at each tower gap for Cases 2, 6, 8, 10, and 12 is shown in Figure 5-17. The jet inlet angle was varied for these cases from 60° to 84°. There is a greater range of jet angles that will cover the low tower relative to the high tower cases. Irrespective of where the jet is aimed on the tower, $\%\dot{m}_{\mathrm{g,net}}$ at the top four gaps is always below 2. Because the tower is closer to the ground relative to the high tower cases, the distance from the inlet to the top of the tower is reduced and the air jet will experience less velocity decay before it reaches these gaps. In contrast to the high tower cases, at Gaps 10 and 11 the jet velocity can still be strong enough to push airflow into the gaps. From Gaps 12 to 15 the jet velocity has decayed to the point where it is not strong enough to push airflow into the gaps. When β is 0.25, Gaps 1 to 10 have $\%\dot{m}_{\mathrm{g,net}}$ values above 2. Increasing β to 0.51 causes the value of $\%\dot{m}_{\mathrm{g,net}}$ at Gaps 1 and 2 to drop below 2 but it raises it above 2 for Gap 11. Further increasing β beyond 0.51 increases the number of the bottom gaps with $\%\dot{m}_{\mathrm{g,net}}$ values below 2; up to four gaps when β is 0.95. Increasing β beyond 0.51 does not improve the number of gaps covered at the top of the tower. The behavior where the jet misses the bottom gaps when β is at or above 0.51 is different from what was observed for the high tower cases where the bottom gaps always had $\%\dot{m}_{\mathrm{g,net}}$ values above 2.

The $T_{\mathrm{g,max}}$ at each tower gap for Cases 2, 6, 8, 10, and 12 is shown in Figure 5-18. Similar to the high tower cases, for a significant majority of the gaps, when $\%\dot{m}_{\mathrm{g,net}}$ is below 2, $T_{\mathrm{g,max}}$ is above 60°C.

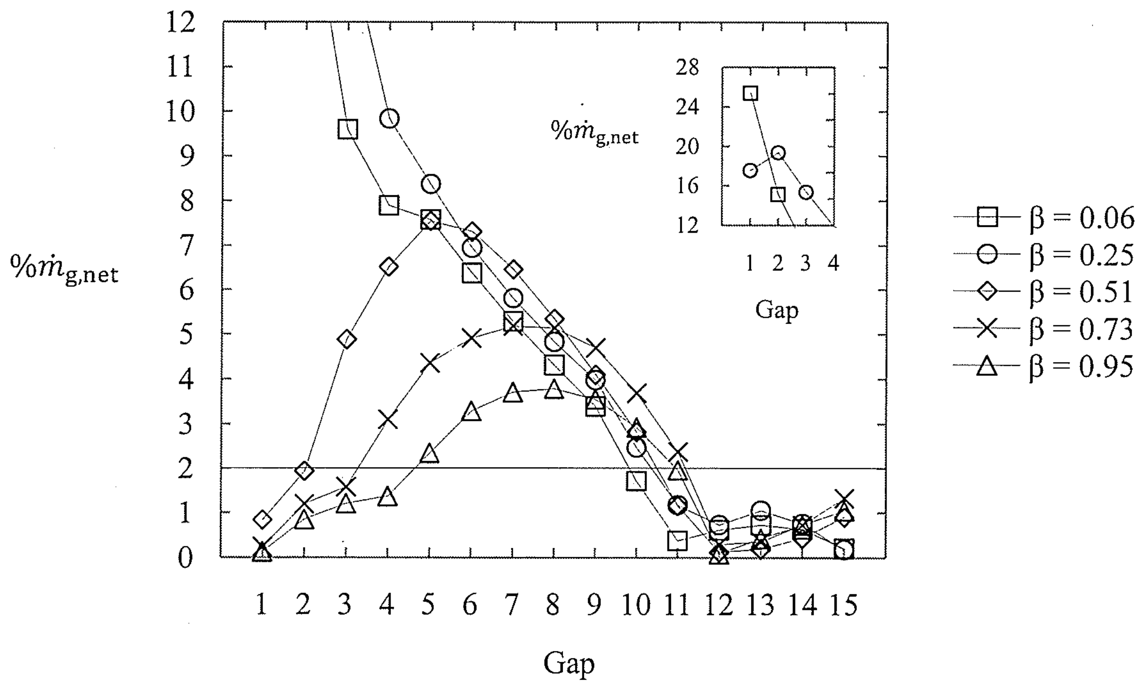

Figure 5-17: $\%\dot{m}_{g,net}$ for all tower gaps (Cases 2, 6, 8, 10, and 12)

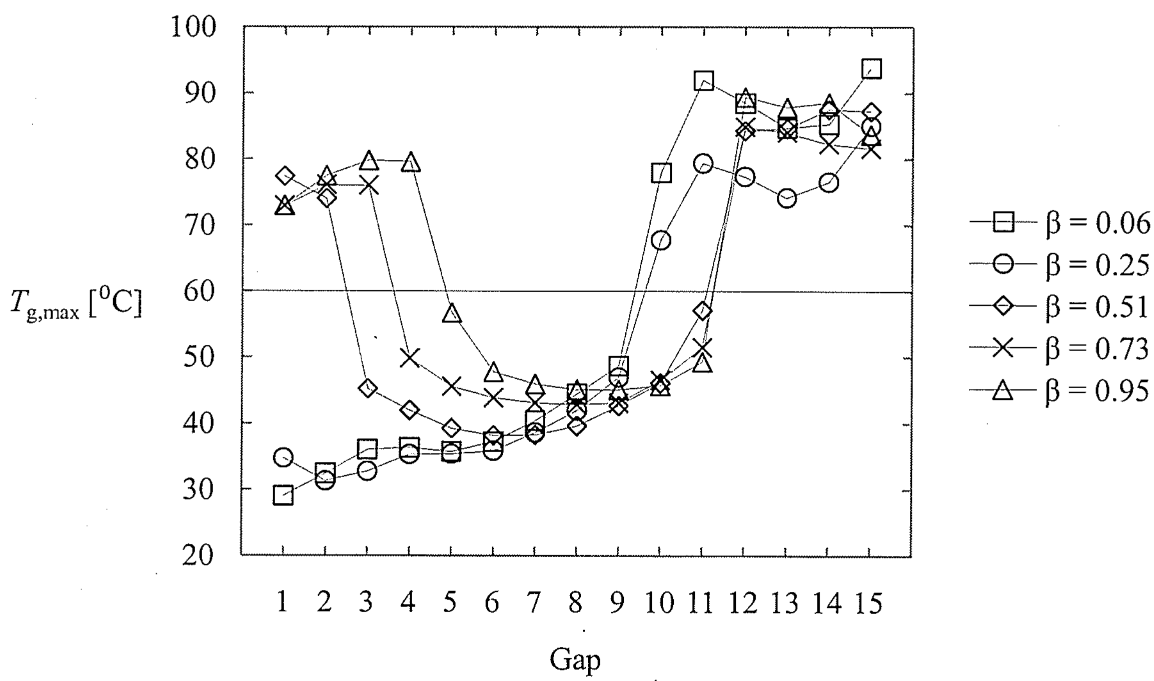

Figure 5-18: $T_{g,max}$ for all tower gaps (Cases 2, 6, 8, 10, and 12)

The v-velocity contours on plane P3 are shown in Figure 5-19 for Cases 2, 6, and 12. For β = 0.06, the highest value of $|v|$ occurs in Gap 1 and below the tower. The size of the contour below the tower is significantly smaller than what was observed for the equivalent high tower case. As well, the range of $|v|$ is significantly wider than the equivalent case in Figure 5-14. Similar to the equivalent high tower case, the tower target location and the gap with the highest $\%\dot{m}_{g,net}$ value both occur at Gap 1. The contour is qualitatively shown to cover Gaps 1 to 9; this corresponds with the gaps that have relatively low $T_{g,max}$ values and relatively high $\%\dot{m}_{g,net}$ values.

For $\beta = 0.25$, the highest value of $|v|$ occurs at Gaps 1 to 2 and does not occur below the tower. The gap with the highest $\%\dot{m}_{g,net}$ is Gap 2; this is two gaps lower than the tower target location. The contour is qualitatively shown to cover the same number of gaps that was observed when β was 0.06 but overall the magnitude of $|v|$ at the gaps has been increased.

For $\beta = 0.95$, the gap with the highest $\%\dot{m}_{g,net}$ value occurs at Gap 8; this is seven gaps lower than the tower target location. The contour plot indicates relatively lower values of $|v|$ compared to when β was 0.06 and 0.25. The bottom gaps are no longer fully covered by the contours. For the low tower cases, the distance that the air jet sinks below the tower target location is smaller relative to an equivalent high tower case.

The streamlines entering Gap 11 on plane P1 for Cases 6 and 10 are shown in Figures 5-20 and 5-21, respectively. When β is 0.25 (case 6), the streamlines at this gap show the characteristics of type 3. The values of $\%\dot{m}_{g,net}$ and $T_{g,max}$ at this gap are 1.2 and 79.4°C, respectively. Increasing β from 0.25 to 0.73 causes the streamlines at this gap to change to type 1. The value of $\%\dot{m}_{g,net}$ increased to 2.4 and $T_{g,max}$ is reduced to 51.5°C.

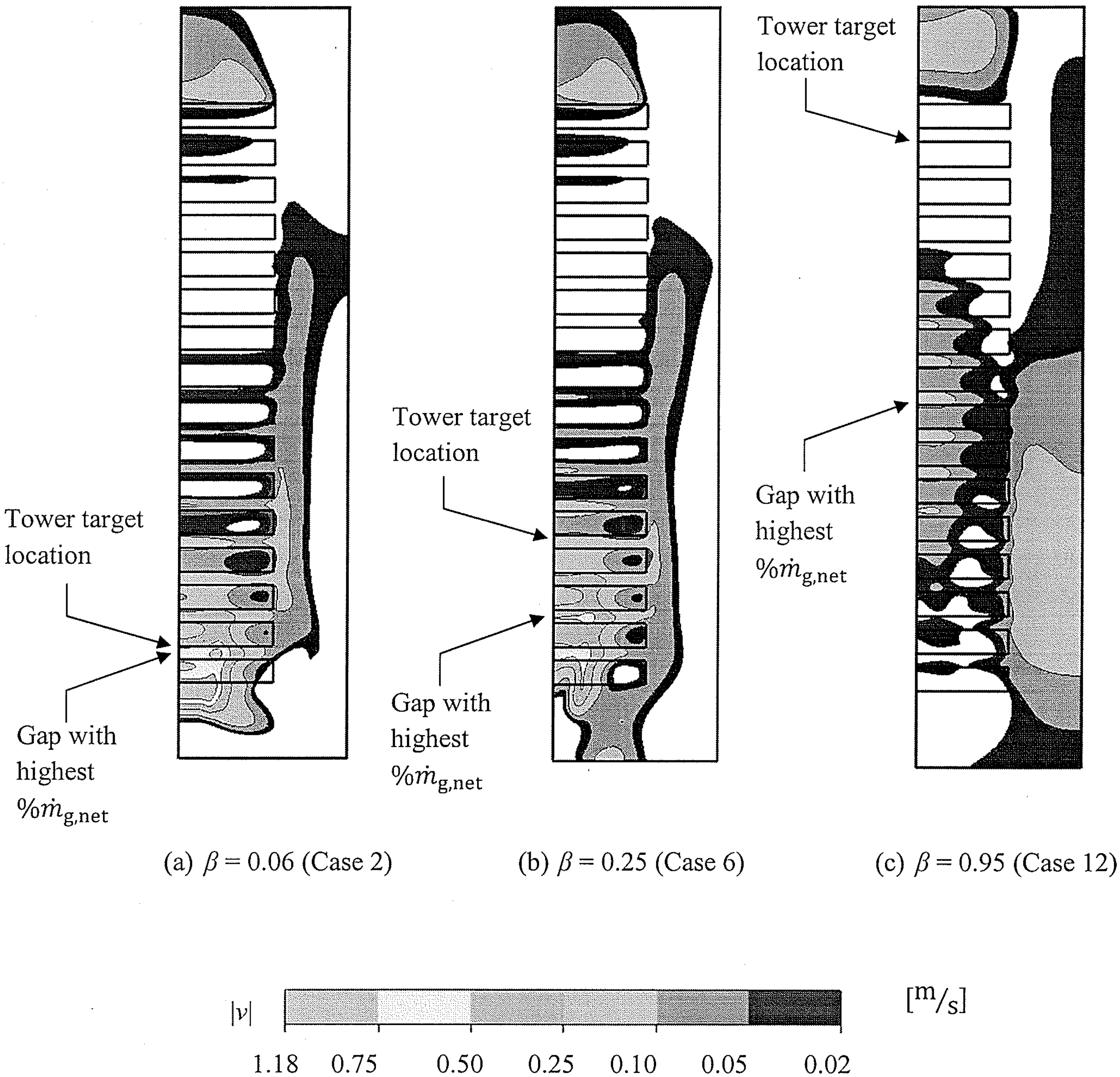

Figure 5-19: Contours of |v| on plane P3 for Cases 2, 6, and 12

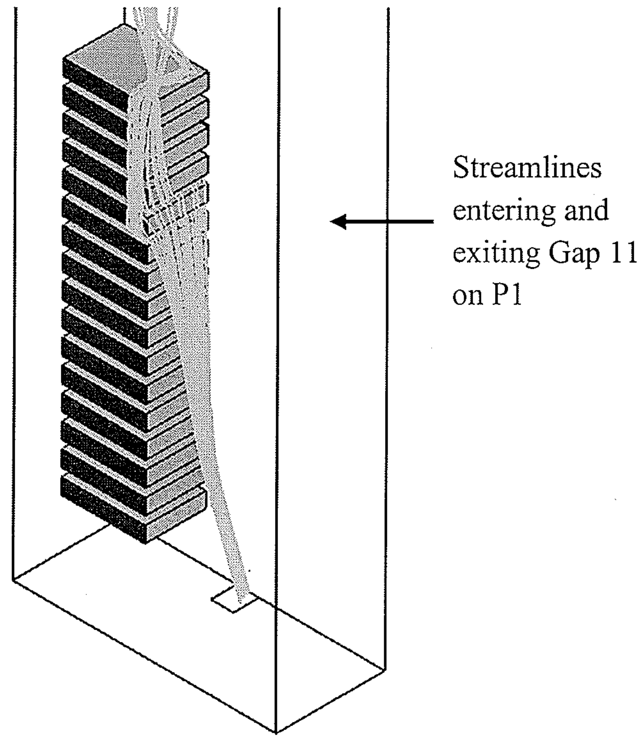

Figure 5-20: Type 3 streamlines entering Gap 11 on plane P1 (Case 6)

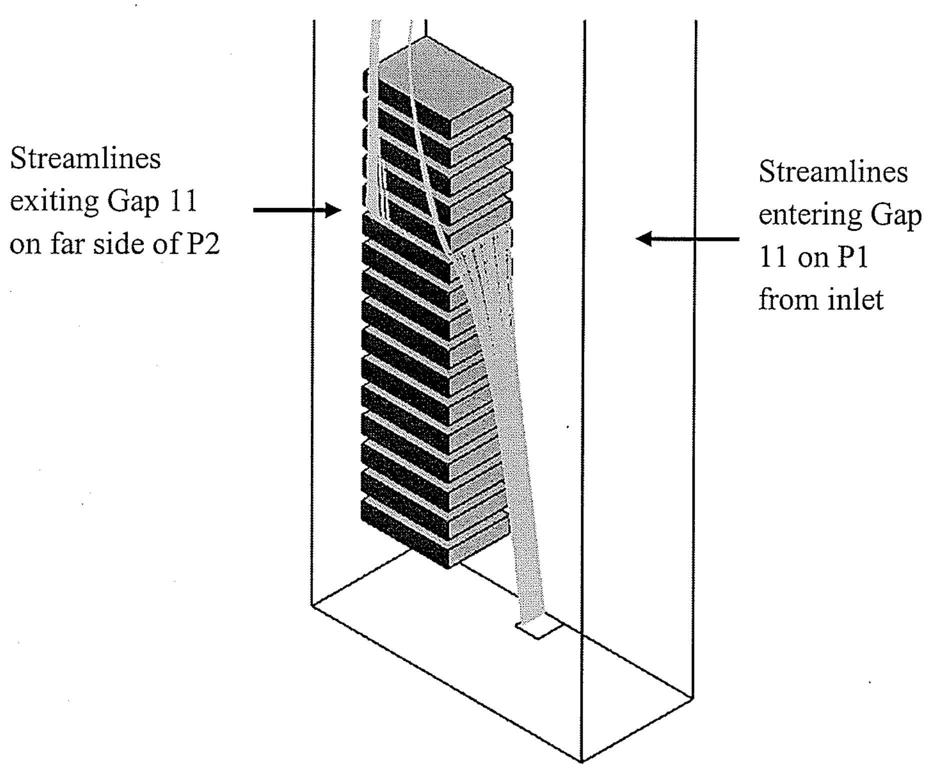

Figure 5-21: Type 1 streamlines entering Gap 11 on plane P1 (Case 10)

5.2.2.3: Summary of the Effect of β for the Base Inlet Conditions

In the previous sections, a strong correlation was demonstrated between a gap having $\%\dot{m}_{\mathrm{g,net}}$ values above 2 and having $T_{\mathrm{g,max}}$ values below 60°C. Plots of $T_{\mathrm{g,max}}$ vs. $\%\dot{m}_{\mathrm{g,net}}$ are shown in Figures 5-22 and 5-23 for the high tower and low tower, respectively. The figures are divided into four quadrants.

Quadrant 1 (Q1): $(2 < \%\dot{m}_{\mathrm{g,net}} < 100)$ and $(20°\mathrm{C} < T_{\mathrm{g,max}} < 60°\mathrm{C})$

Quadrant 2 (Q2): $(2 < \%\dot{m}_{\mathrm{g,net}} < 100)$ and $(60°\mathrm{C} < T_{\mathrm{g,max}} < 100°\mathrm{C})$

Quadrant 3 (Q3): $(0 < \%\dot{m}_{\mathrm{g,net}} < 2)$ and $(60°\mathrm{C} < T_{\mathrm{g,max}} < 100°\mathrm{C})$

Quadrant 4 (Q4): $(0 < \%\dot{m}_{\mathrm{g,net}} < 2)$ and $(20°\mathrm{C} < T_{\mathrm{g,max}} < 60°\mathrm{C})$

In Quadrant 1 the data points follow a clear trend where $T_{\mathrm{g,max}}$ increases exponentially with decreasing $\%\dot{m}_{\mathrm{g,net}}$. The dominant mechanism of heat removal for these gaps is forced convection. In Quadrant 3 the data points are significantly more scattered indicating that $\%\dot{m}_{\mathrm{g,net}}$ is not the only factor affecting $T_{\mathrm{g,max}}$. For the data points in quadrant 3, the airflow entering a gap consists of relatively low velocity airflow from the inlet and airflow that is circulating within the domain due to temperature gradients. The primary means of cooling is free convection in this quadrant. Out of 180 data points resulting from Cases 1 to 12 only one data point is located in Quadrant 2 and three data points are located in Quadrant 4. These results clearly confirm the rule of thumb that a minimum value of $\%\dot{m}_{\mathrm{g,net}} = 2$ is required for maintaining $T_{\mathrm{g,max}}$ below 60°C, irrespective of θ for both the high and low towers.

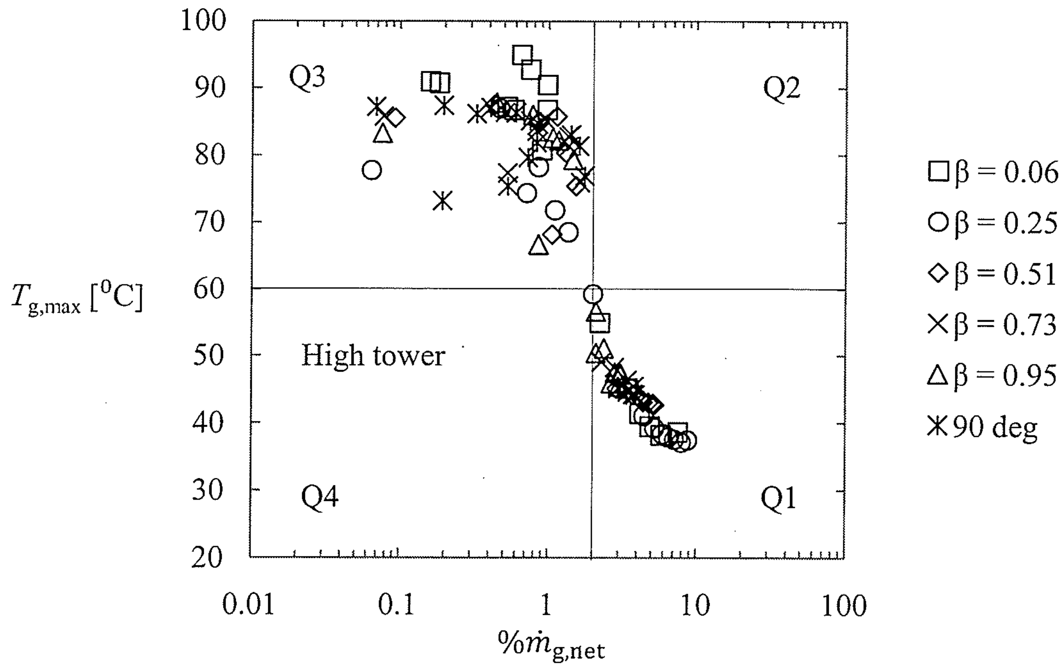

Figure 5-22: $T_{g,max}$ vs. $\%\dot{m}_{g,net}$ (Cases 1, 3, 5, 7, 9, and 11)

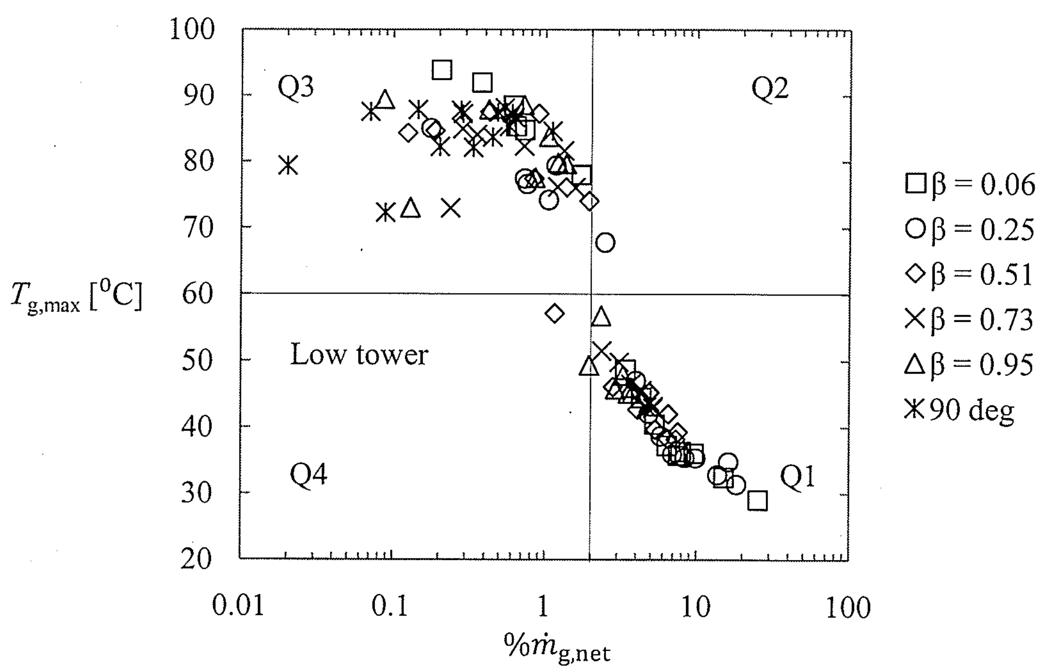

Figure 5-23: $T_{g,max}$ vs. $\%\dot{m}_{g,net}$ (Cases 2, 4, 6, 8, 10, and 12)

The summation of $\%\dot{m}_{g,net}$ for all tower gaps will be defined as $\sum\%\dot{m}_{g,net}$. The profile for $\sum\%\dot{m}_{g,net}$ as β is varied for both the high tower and low tower is shown in Figure 5-24. For both tower elevations, the highest $\sum\%\dot{m}_{g,net}$ value occurs when β is 0.25, and $\sum\%\dot{m}_{g,net}$ decreases as β deviates from this position. When β is in the range from 0.06 to 0.25, $\sum\%\dot{m}_{g,net}$ is significantly higher for the low tower relative to the high tower. As β is increased beyond 0.25, the difference between the high and low tower cases decreases until they are virtually the same when β is 0.95.

The average temperature of all tower gap surfaces will be defined as $T_{t,av}$. The profile for $T_{t,av}$ as β is varied for both the high tower and low tower is shown in Figure 5-25. For both tower elevations, the lowest $T_{t,av}$ occurs when β is 0.25. This corresponds to the condition where the highest $\sum\%\dot{m}_{g,net}$ was observed. The value of $T_{t,av}$ increases as $\sum\%\dot{m}_{g,net}$ decreases. The low tower cases have a lower $T_{t,av}$ for all β values except for $\beta = 0.95$. The greatest difference in $T_{t,av}$ between the two tower elevations occurs when β is 0.06; this corresponds to the β with the greatest difference in $\sum\%\dot{m}_{g,net}$ between the two cases.

The maximum temperature for all tower surfaces will be defined as $T_{t,max}$. The profile of $T_{t,max}$ as β is varied for both the high and low towers are shown in Figure 5-26. The value of $T_{t,max}$ is always above 60°C, irrespective of the value of β. The high and low tower cases have similar $T_{t,max}$ values despite having different $\sum\%\dot{m}_{g,net}$ and $T_{t,av}$ values. This result is because, for both tower heights, at least one tower gap had $\%\dot{m}_{g,net}$ below 2.

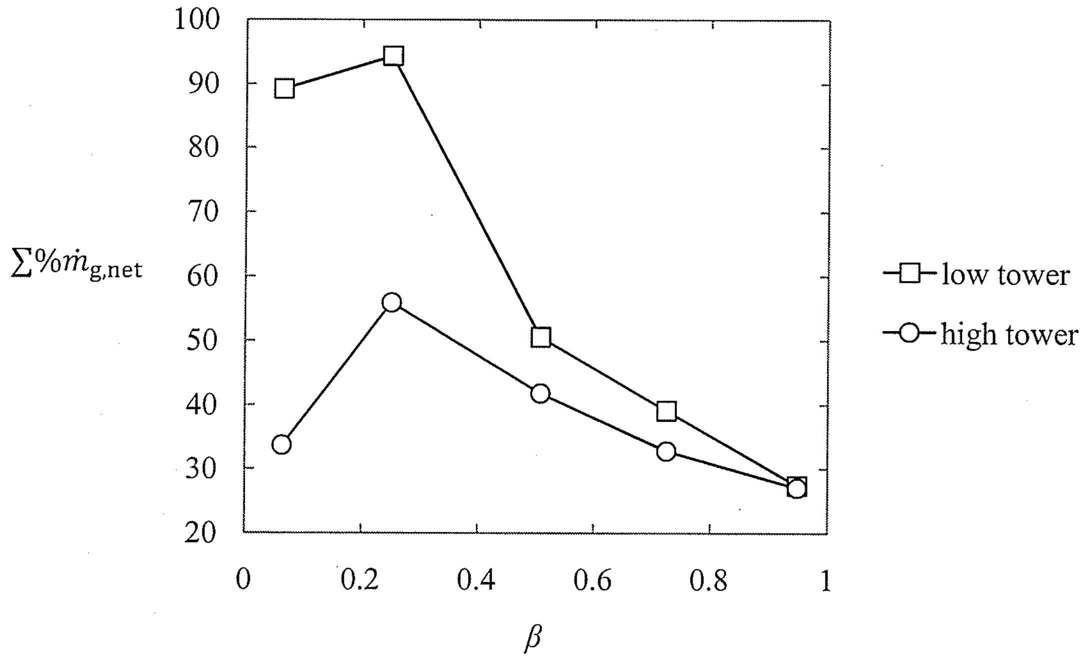

Figure 5-24: $\sum\%\dot{m}_{g,net}$ vs. β (Cases 1, 2, and 5 to 12)

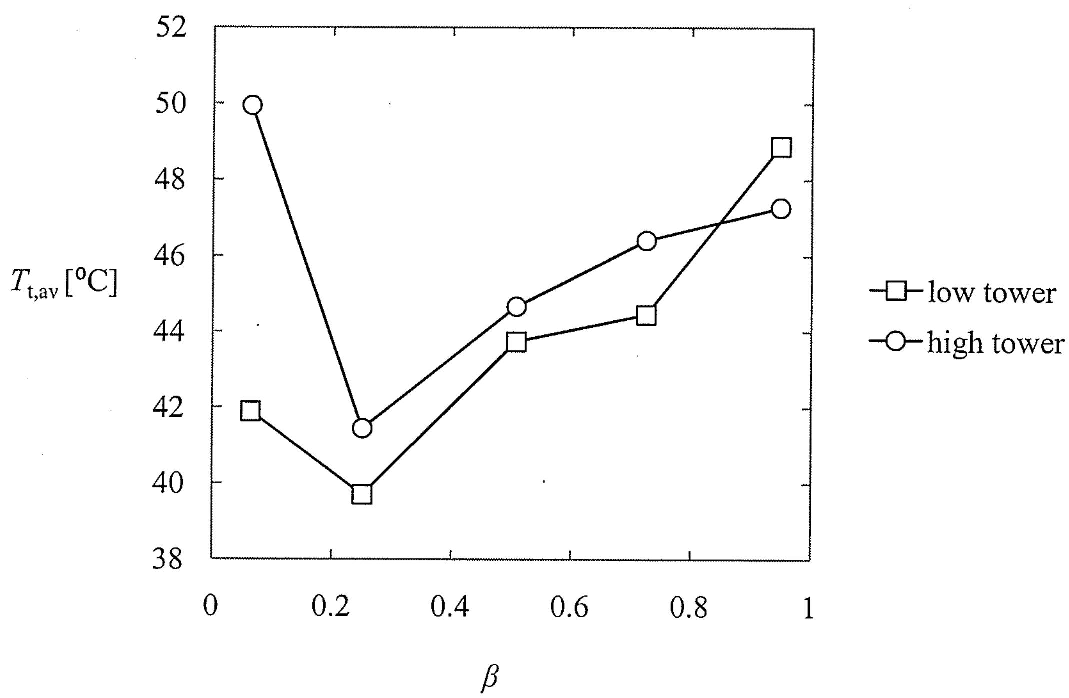

Figure 5-25: $T_{t,av}$ vs. β (Cases 1, 2, and 5 to 12)

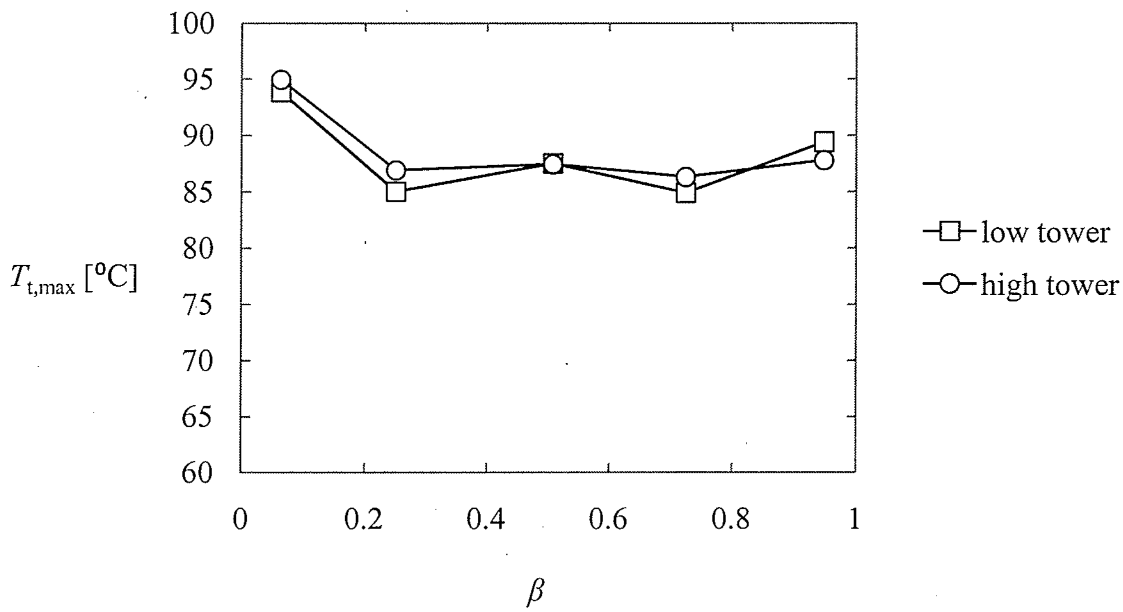

Figure 5-26: $T_{t,max}$ vs. β (Cases 1, 2, and 5 to 12)

A summary of the results for the base inlet conditions in provided in Table 5-2. When β is 0.25, nine tower gaps have temperature values below 60°C, irrespective of the tower elevation. At this β, $T_{t,av}$ is slightly lower for the low tower. For both tower elevations it is not possible to have a maximum temperature at all gaps below 60°C.

The primary differences in the ventilation systems for the high and low tower are:

- For the high tower, irrespective of the value of β the ventilation system will never sufficiently cover Gaps 10 to 15. The bottom of the tower always receives sufficient airflow.
- For the low tower, irrespective of the value of β the ventilation system will never sufficiently cover Gaps 12 to 15. When the air jet is aimed low the top of the tower receives insufficient airflow. If the air jet is aimed high, the bottom of the tower receives insufficient airflow.

From the results of changing θ for the original inlet configuration, the following observations can be:

- In VH42, θ should be changed from the current value of 90° to about 80°-81°. This will significantly improve the ventilation of the tower by increasing the number of gaps cooled below 60°C from zero to nine. The value for $T_{t,av}$ will be reduced by about 17°C. There will be relatively little change in $T_{t,max}$ as β is varied.
- In VH41, a modest improvement can be obtained by changing θ from 60° to about 70°. This does not increase the number of gaps cooled below 60 °C but does reduce $T_{t,av}$ by about 2°C. Similar to VH42, there is relatively little change in $T_{t,max}$ as β is varied.

Table 5-2: Summary of key results from Cases 1 to 12

Case	θ [deg]	β	Tower Type	$T_{t,max}$ [^{0}C]	No. of gaps with $T_{g,max}$ > 60 [^{0}C]	$T_{t,av}$ [^{0}C]	$\sum\%\dot{m}_{g,net}$
1	77.4	0.06	High Tower	94.9	9	49.9	33.7
3	90	N/A		87.4	15	58.7	11.0
5	80.7	0.25		86.9	6	41.4	55.9
7	83.2	0.51		87.4	7	44.7	41.8
9	84.5	0.73		86.3	7	46.4	32.7
11	85.4	0.95		87.8	7	47.3	27.0
2	60	0.06	Low Tower	93.8	6	41.9	89.2
4	90	N/A		87.8	15	61.6	5.8
6	70	0.25		85.0	6	39.7	94.3
8	80	0.51		87.5	6	43.7	50.5
10	82.5	0.73		84.9	7	44.5	39.1
12	84	0.95		89.4	8	48.9	27.4

5.3: The Effect of Inlet Geometry

In the previous section, it was found that the current jet velocity is not strong enough to reach the top of the tower. Due to the conservation of mass, decreasing the size of the inlet will proportionately increase the jet velocity.

The following sections will present the results obtained by using different inlet geometries, with the inlet port kept at the base location and a constant inlet mass flow rate. In Sections 5.3.1 and 5.3.4, the size of the inlet will be varied with the tower elevation and jet impact location held constant. In Section 5.3.2 and Section 5.3.3 the effect of varying β for different inlet geometries will be examined for the high and low towers.

5.3.1: The Effect of Varying L_x While Keeping L_y Constant for the High Tower, Cases 7, 17, 27, and 31

The size of the inlet port will be changed in the following section by varying L_x and holding L_y constant at the base length. The following results are for high tower with β = 0.51. The four different inlet geometries that will be compared in this section are shown in Figure 5-27.

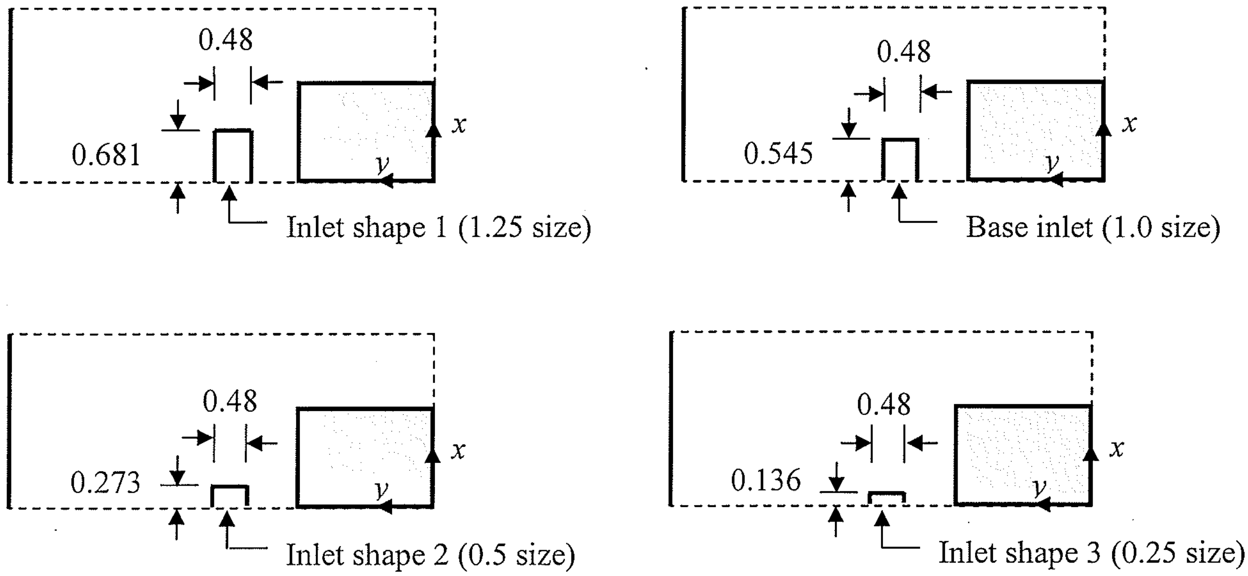

Figure 5-27: Top view of inlet sizes. Dimensions shown in meters.

The values for $\%\dot{m}_{\mathrm{g,net}}$ and $T_{\mathrm{g,max}}$ at each tower gap for case 7, 17, 27, and 31 are shown in Figures 5-28 and 5-29, respectively. As the inlet size is reduced, the value of $\%\dot{m}_{\mathrm{g,net}}$ generally increases at all tower gaps. When the inlet size is increased to inlet shape 1, only Gaps 1 to 6 have $\%\dot{m}_{\mathrm{g,net}}$ values above 2. When the inlet size is reduced to inlet shape 2, Gaps 1 to 13 have $\%\dot{m}_{\mathrm{g,net}}$ values above the threshold. This indicates that the jet velocity is now strong enough to push airflow into these gaps. When the inlet size is reduced further to inlet shape 3, all of the tower gaps have $\%\dot{m}_{\mathrm{g,net}}$ values above the threshold value. The jet velocity is now at a magnitude where it can reach the top of the tower. As previously shown, when $\%\dot{m}_{\mathrm{g,net}}$ is higher than 2, $T_{\mathrm{g,max}}$ is normally below 60°C. Case 27 is the first case that has been presented to have all $T_{\mathrm{g,max}}$ values below 60°C. Examining the streamlines for Case 27 indicates that all gap streamlines are type 1 (these results are not shown).

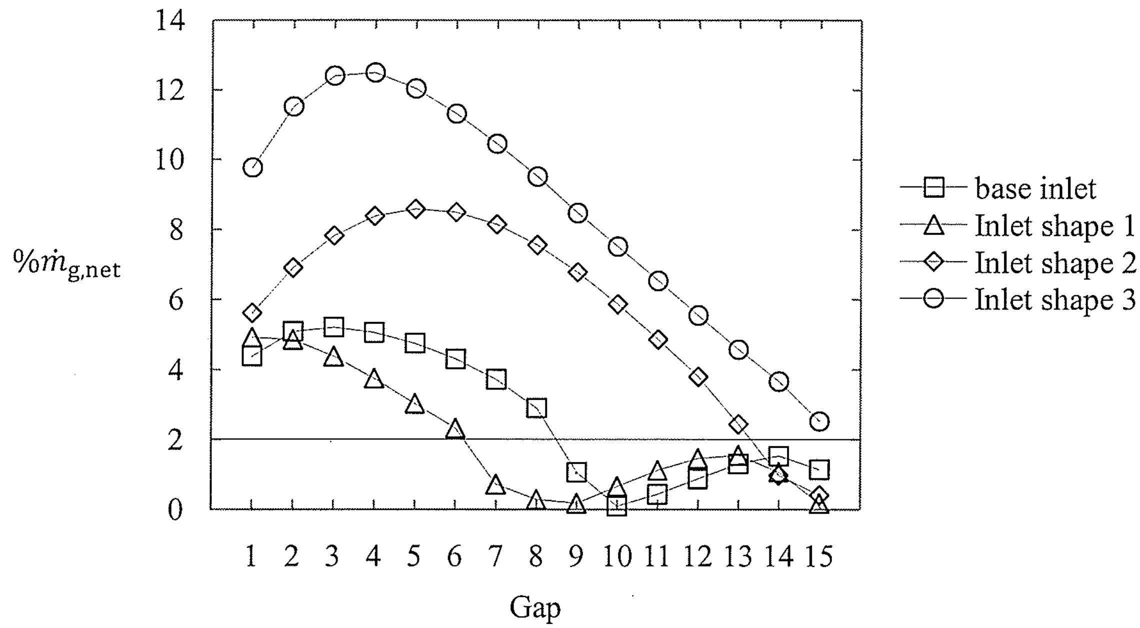

Figure 5-28: $\%\dot{m}_{g,net}$ for all tower gaps (Cases 7, 17, 27, and 31)

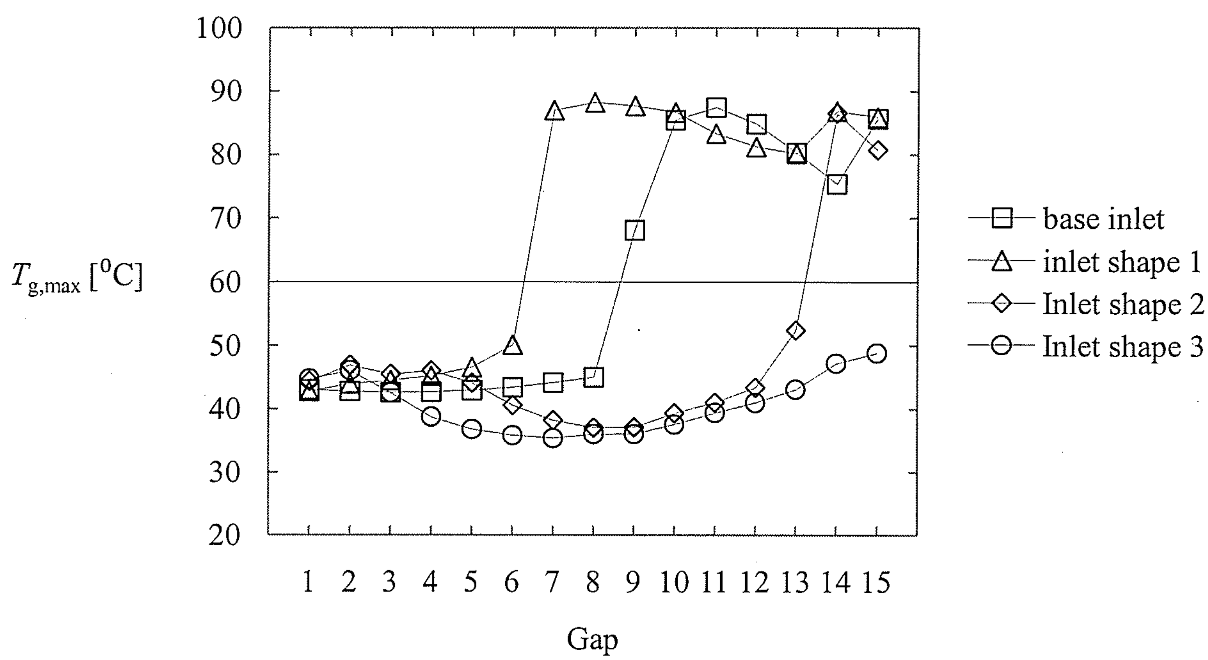

Figure 5-29: $T_{g,max}$ for all tower gaps (Cases 7, 17, 27, and 31)

Contours of the v-velocity component on plane P3 are shown in Figure 5-30 for Cases 27 and 31.

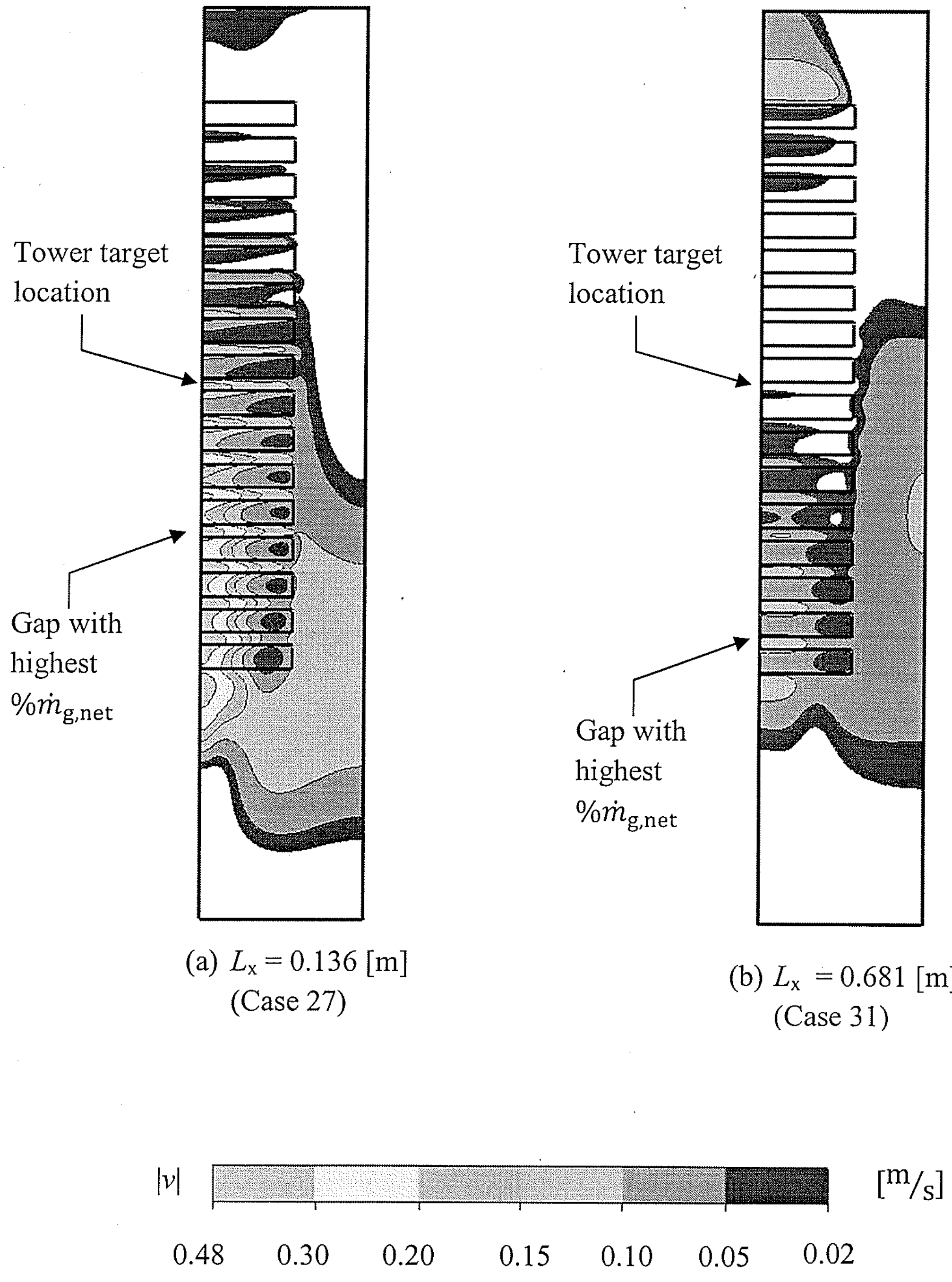

(a) $L_x = 0.136$ [m] (Case 27)

(b) $L_x = 0.681$ [m] (Case 31)

Figure 5-30: Contours of $|v|$ on plane P3 for Cases 27 and 31

Reducing the size of the inlet from inlet shape 1 to inlet shape 3 is shown to significantly increase the value of $|v|$. For Case 31, the gap with the highest $\%\dot{m}_{\mathrm{g,net}}$ value is seven gaps below the target location at Gap 1. For Case 27, the gap with the highest $\%\dot{m}_{\mathrm{g,net}}$ value is four gaps below the target location at Gap 4. The zone of high $|v|$ is qualitatively shown to be narrow in the x-direction and long in the z-direction. This coincides with the shape of the inlet which is narrow in the x-direction and long in the y-direction

The profiles of $\sum\%\dot{m}_{\mathrm{g,net}}$ and $T_{\mathrm{t,av}}$ as L_{x} is varied are shown in Figure 5-31. As the length of L_{x} is decreased, $\sum\%\dot{m}_{\mathrm{g,net}}$ increases and $T_{\mathrm{t,av}}$ decreases. A strong correlation is shown between the average temperature of the tower and the amount of airflow penetrating the gaps. When the inlet is reduced to 0.25 of the base size, $\sum\%\dot{m}_{\mathrm{g,net}}$ is above 100; this trend is a result of airflow from the ventilation system entering multiple gaps and air circulating into the gaps due to buoyancy effects.

The profile for $T_{\mathrm{t,max}}$ as L_{x} is varied is shown in Figure 5-32. There is relatively no change in $T_{\mathrm{t,max}}$ when the L_{x} is in the range of 0.681 [m] to 0.273 [m]. Once L_{x} is reduced to 0.136 [m], $T_{\mathrm{t,max}}$ decreases below 60°C.

A summary of the results for reducing the inlet size are provided in Table 5-3. From the above discussion it can be concluded that, for the high tower and a value β of 0.51, reducing the inlet size will decrease $T_{\mathrm{t,av}}$ and increase the number gaps with $\%\dot{m}_{\mathrm{g,net}}$ values above the threshold. Once the inlet size is reduced to 25% of the base size, all tower gaps have $T_{\mathrm{g,max}}$ values below 60°C and $\%\dot{m}_{\mathrm{g,net}}$ values above 2.

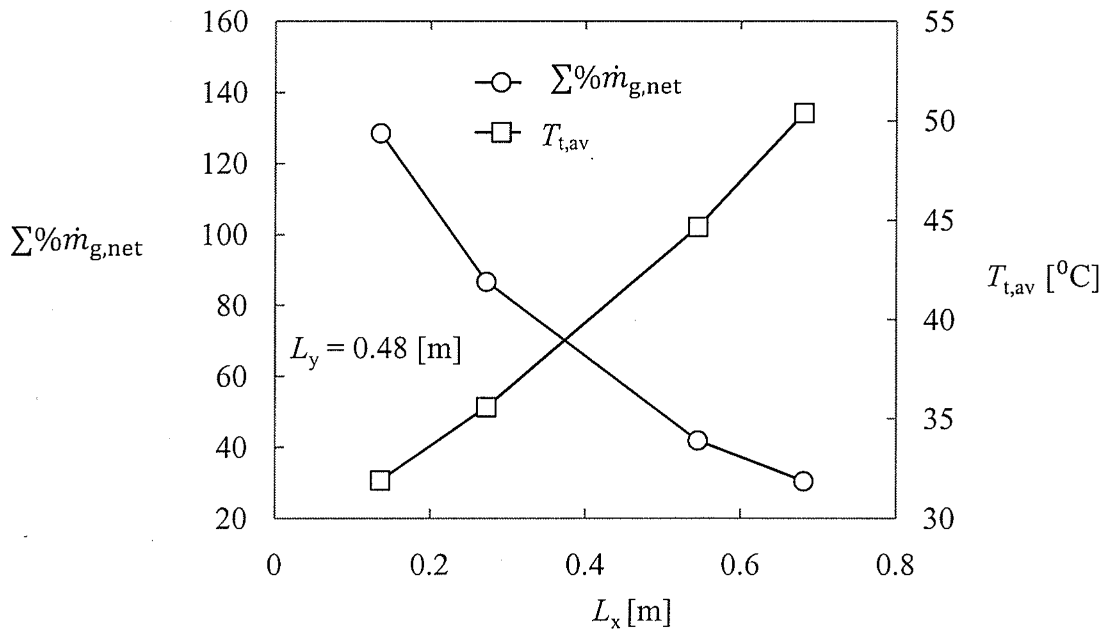

Figure 5-31: $\sum\%\dot{m}_{g,net}$ and $T_{t,av}$ vs. L_x (Cases 7, 17, 27, and 31)

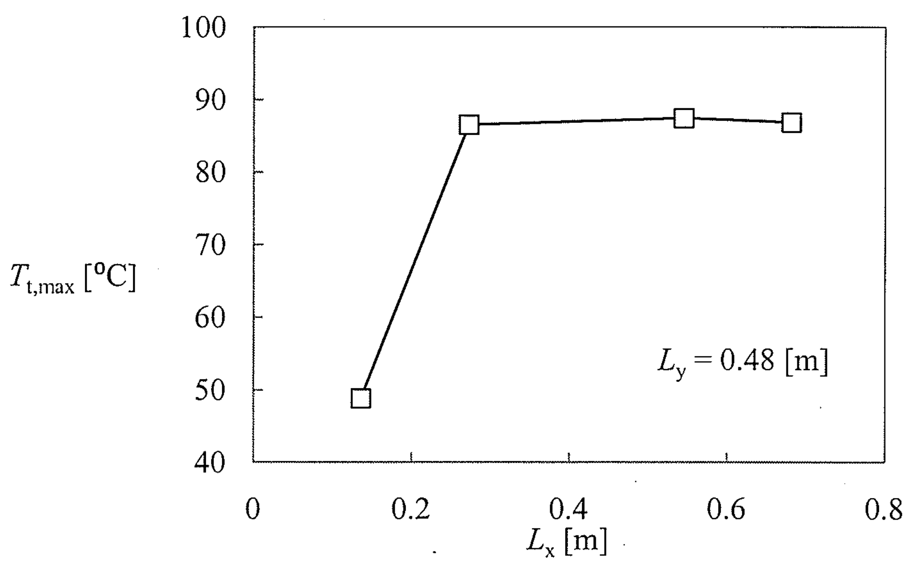

Figure 5-32: $T_{t,max}$ vs. L_x (Cases 7, 17, 27, and 31)

Table 5-3: Summary of key results from Cases 7, 17, 27, and 31

Case	L_x [m]	β	Tower Type	$T_{t,max}$ [^{0}C]	No. of gaps with $T_{g,max}$ > 60 [^{0}C]	$T_{t,av}$ [^{0}C]	$\sum\%\dot{m}_{g,net}$
7	0.545	0.51	High Tower	87.4	7	44.7	41.8
17	0.273			86.5	2	35.6	86.6
27	0.136			48.8	0	31.9	128.4
31	0.681			86.9	9	50.4	30.4

5.3.2: The Effect of β for Inlet Shape 3, Cases 23 to 30

The following section will discuss the effect of varying β for inlet shape 3. The results from the high and low towers will be presented separately and the section will be concluded with a comparison between the two tower elevations.

5.3.2.1: The Effect of β for the High Tower, Cases 23, 25, 27, and 29

The profiles of $\%\dot{m}_{g,net}$ and $T_{g,max}$ at all tower gap are shown in Figures 5-33 and 5-34, respectively for Cases 23, 25, 27, and 29. When β is 0.06, Gaps 14 and 15 have $\%\dot{m}_{g,net}$ values below 2. For all other values of β, all tower gaps experience $\%\dot{m}_{g,net}$ values above 2, except Gap 15 at $\beta = 0.95$. Increasing β beyond 0.25 lowers $\%\dot{m}_{g,net}$ for the first six gaps but does not significantly change $\%\dot{m}_{g,net}$ for the top nine gaps. The only case that has maximum gap temperatures above 60°C is when β is 0.06.

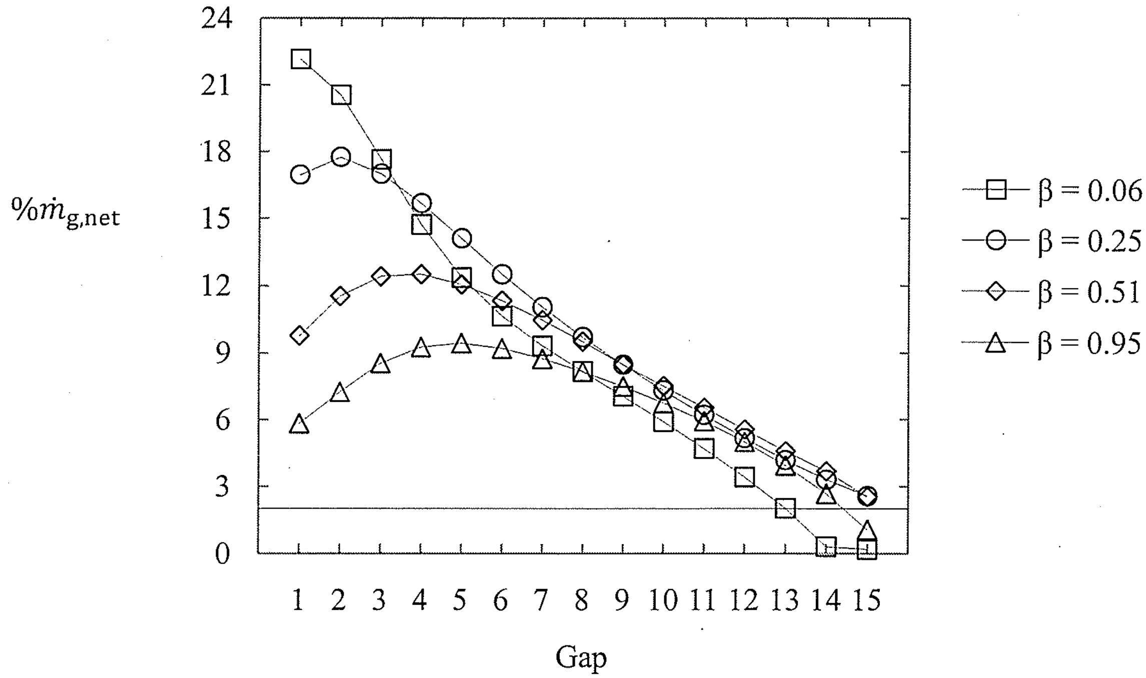

Figure 5-33: $\%\dot{m}_{g,net}$ for all tower gaps (Cases 23, 25, 27, and 29)

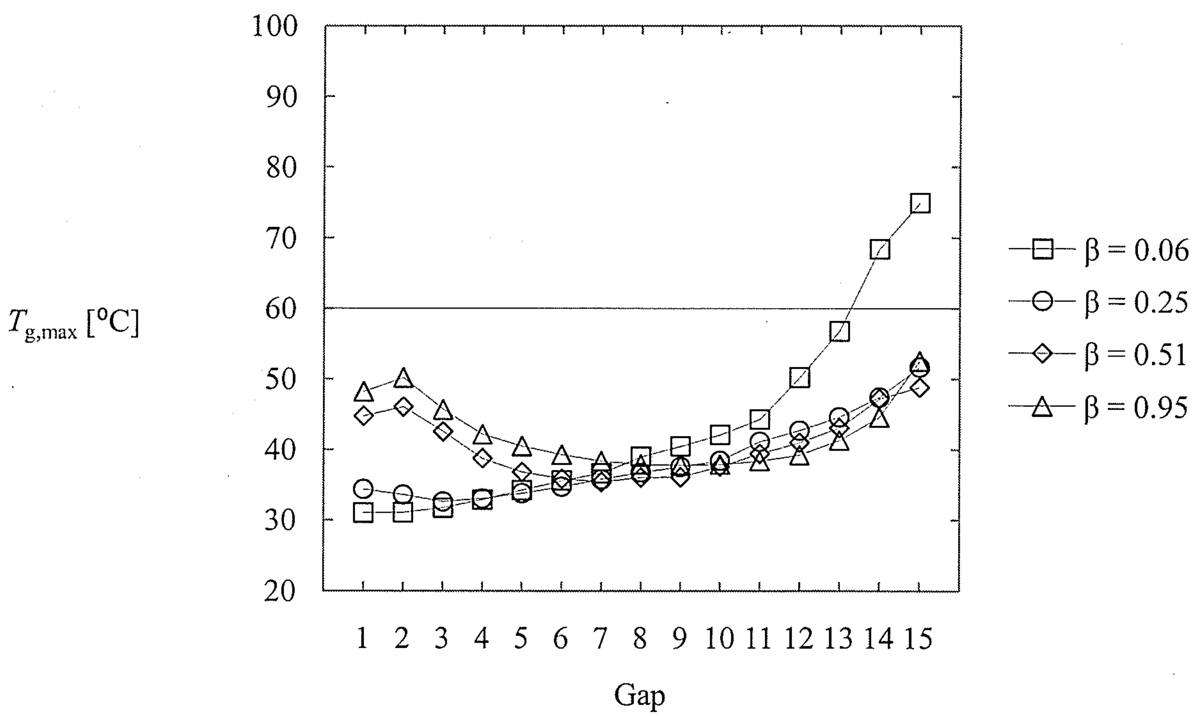

Figure 5-34: $T_{g,max}$ for all tower gaps (Case 23, 25, 27, and 29)

5.3.2.2: The Effect of β for the Low Tower, Cases 24, 26, 28, and 30

The profiles of $\%\dot{m}_{g,net}$ and $T_{g,max}$ at all tower gaps are shown in Figures 5-35 and 5-36, respectively for Cases 24, 26, 28, and 30. When β is in the range of 0.06 to 0.25, $\%\dot{m}_{g,net}$ is high for the bottom gaps and low for the top gaps. When β is in the range of 0.51 to 0.95, $\%\dot{m}_{g,net}$ is low for the bottom gaps and high for the top tower gaps. There is no value of β for the low tower cases where the jet covers the entire tower. This is in contrast to what was observed for the high tower cases. Since θ is lower, relative to the high tower cases, the airflow is localized to where it was aimed on the tower and is not spread out like was seen with the high tower cases. When $\%\dot{m}_{g,net}$ is above 2, $T_{g,max}$ is reduced below 60°C.

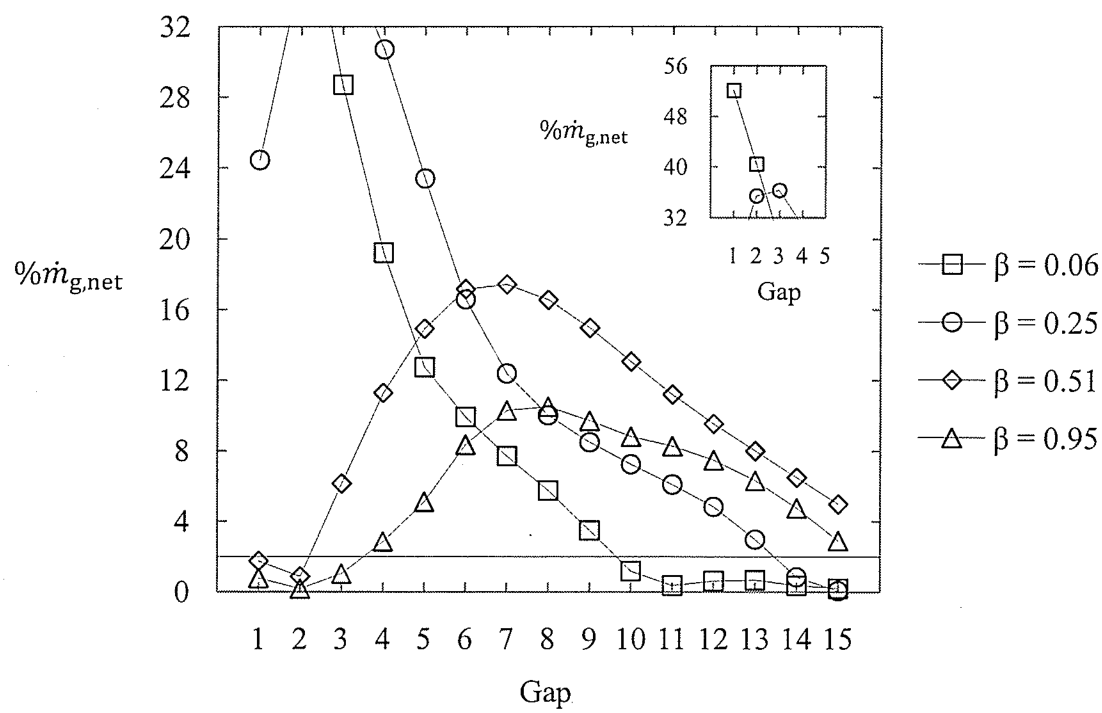

Figure 5-35: $\%\dot{m}_{g,net}$ for all tower gaps (Cases 24, 26, 28, and 30)

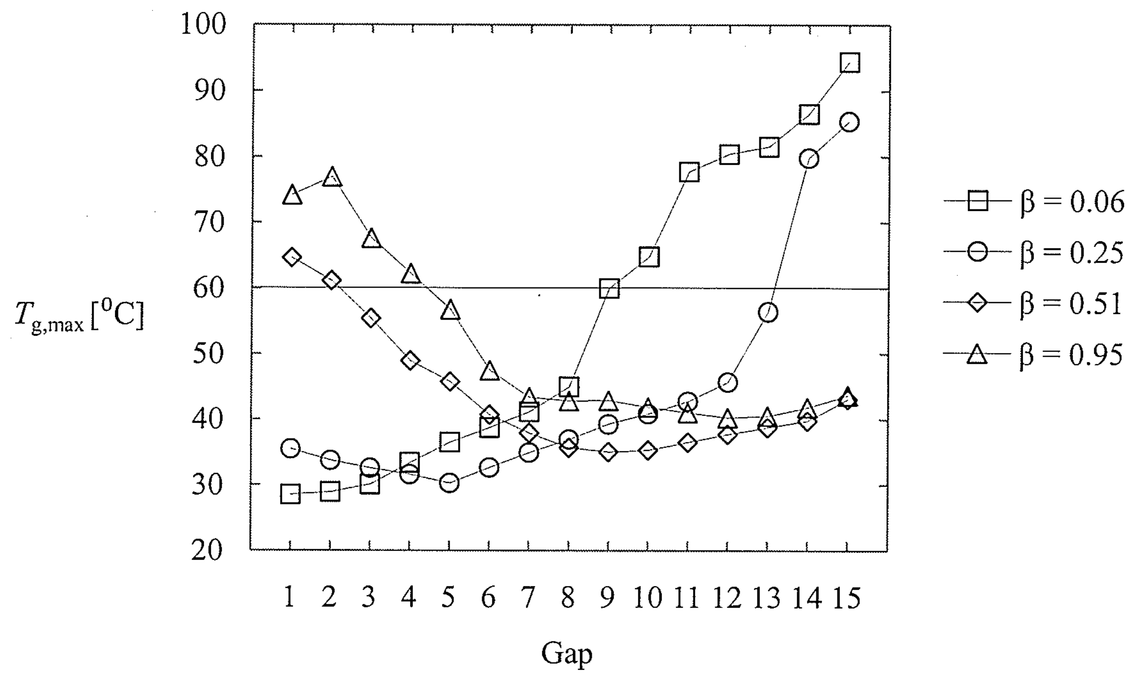

Figure 5-36: $T_{g,max}$for all tower gaps (Cases 24, 26, 28, and 30)

5.3.2.3: Summary of the Effect of β for Inlet Shape 3

The profile of $\sum\%\dot{m}_{g,net}$ as β is varied for both the high and low towers is shown in Figure 5-37. The low tower cases have higher $\sum\%\dot{m}_{g,net}$ for β values in the range of 0.06 to 0.51, and the high tower has a slightly higher $\sum\%\dot{m}_{g,net}$ value when β is 0.95. The maximum $\sum\%\dot{m}_{g,net}$ occurs at a β of 0.25 for both tower elevations. This is the same β that was observed for the cases where the inlet was the base size.

The profile of $T_{t,av}$ as β is varied for both the high and low towers is shown in Figure 5-38. The high tower has lower values of $T_{t,av}$ relative to the low tower for all β values. This is in contrast to what was observed with the base inlet size where the low tower had lower values of $T_{t,av}$, and is in contrast to what would be expected considering that most of the low tower cases have higher values for $\sum\%\dot{m}_{g,net}$. For the low tower cases, certain gaps received excessively high amounts of airflow, while other tower gaps were starved for airflow. For the high tower cases, the tower gaps received less airflow but the airflow was spread out over the entire tower.

The profile of $T_{t,max}$ as β is varied for both the high and low towers is shown in Figure 5-39. For the low tower cases, since the jet always provides inadequate airflow to some tower gaps, $T_{t,max}$ is always relatively high. For the high tower cases, aside from when β is 0.06, $T_{t,max}$ is below 60°C.

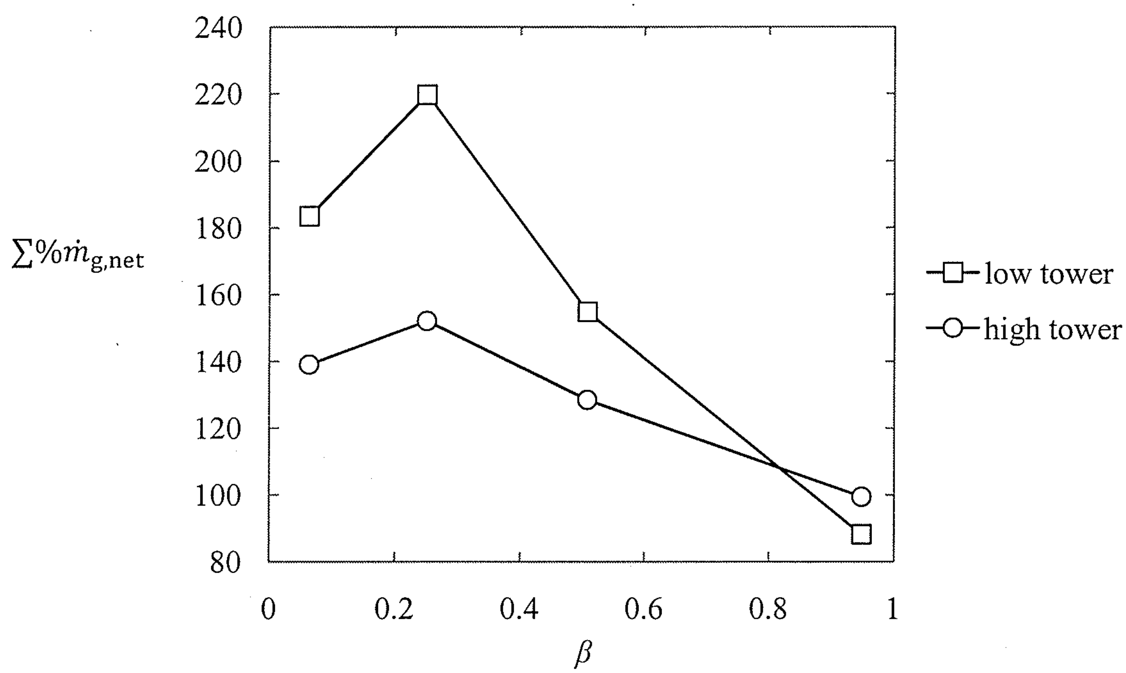

Figure 5-37: $\sum\%\dot{m}_{g,net}$ vs. β (Cases 23 to 30)

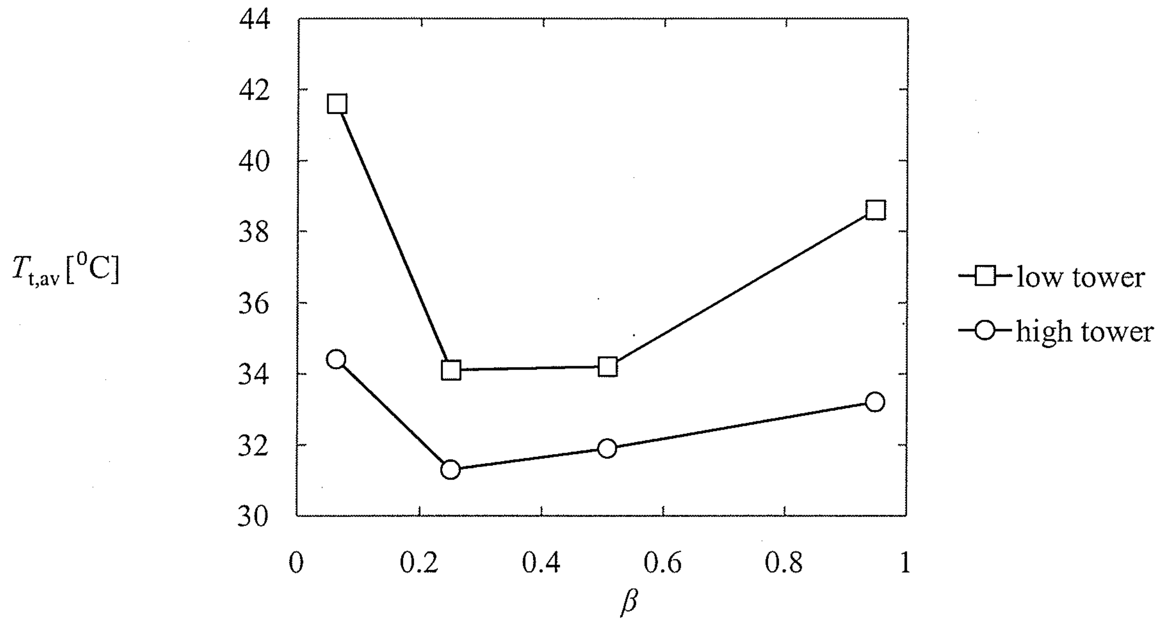

Figure 5-38: $T_{t,av}$ vs. β (Cases 23 to 30)

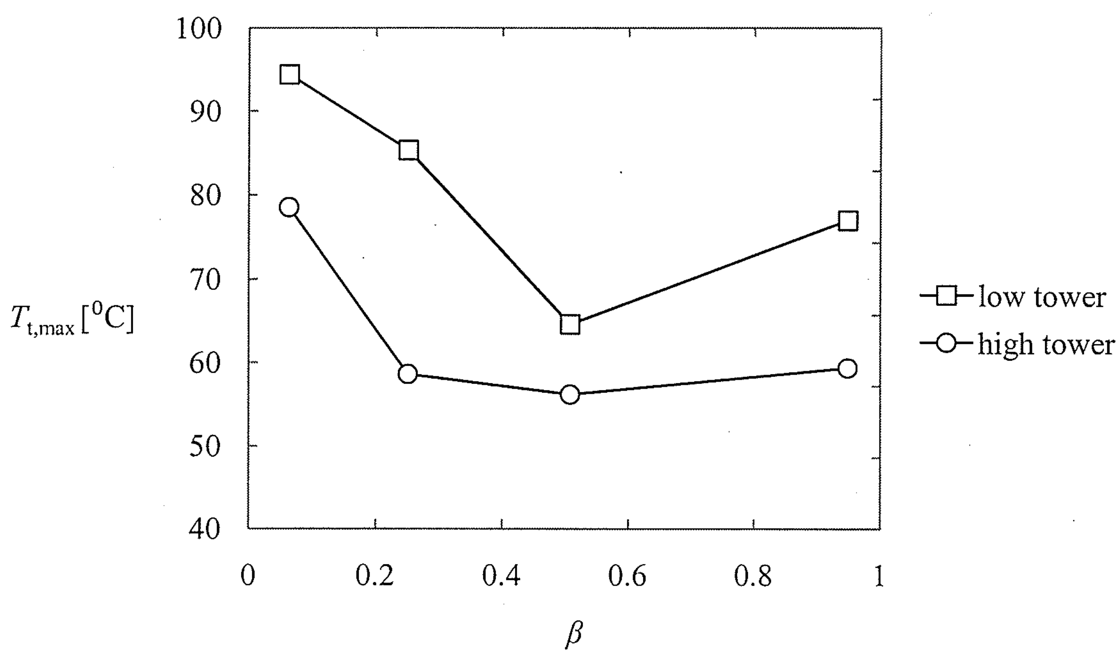

Figure 5-39: $T_{t,max}$ vs. β (Cases 23 to 30)

A summary of the results from the cases in this section are provided in Table 5-4. The following observation can be made regarding the two tower elevation conditions when a shape 3 inlet is implemented:

- At this inlet size, the high tower has a significant advantage over the low tower.
- There is no value of β where the low tower will be completely cooled below 60°C.

Table 5-4: Summary of key results from Cases 23 to 30

Case	θ [deg]	β	Tower Type	$T_{t,max}$ [°C]	No. of gaps with $T_{g,max}$ > 60 [°C]	$T_{t,av}$ [°C]	$\sum\%\dot{m}_{g,net}$
23	77.4	0.06	High Tower	74.9	2	34.4	139.0
25	80.7	0.25		51.7	0	31.3	152.0
27	83.2	0.51		48.8	0	31.9	128.4
29	85.4	0.95		52.5	0	33.2	99.4
24	60	0.06	Low Tower	94.4	6	41.6	138.7
26	70	0.25		85.3	2	34.1	219.7
28	80	0.51		64.6	2	34.2	154.8
30	84	0.95		76.9	4	38.6	88.2

5.3.3: The Effect of β for Inlet Shape 2, Cases 13 to 22

The following sections will discuss the effect of varying β has when the inlet geometry is inlet shape 2. The results from the high and low towers will be presented separately and the section will be concluded with a comparison between the two tower elevations.

5.3.3.1: The Effect of β for the High Tower, Cases 13, 15, 17, 19, and 21

The profiles for $\%\dot{m}_{\mathrm{g,net}}$ and $T_{\mathrm{g,max}}$ at all tower gaps are shown in Figures 5-40 and 5-41, respectively, for Cases 13, 15, 17, 19, and 21. For β = 0.06, Gaps 1 to 10 have $\%\dot{m}_{\mathrm{g,net}}$ values above 2. Increasing β to 0.25 raises $\%\dot{m}_{\mathrm{g,net}}$ above 2 at Gap 11. For β = 0.51 to 0.95, Gaps 1 to 13 have $\%\dot{m}_{\mathrm{g,net}}$ values above 2. Irrespective of where the jet is aimed on the tower, Gaps 14 and 15 never received sufficient airflow. At those gaps, the jet velocity has decayed to a level where it is not strong enough to sufficiently push airflow into these two gaps. Increasing β beyond 0.51 decreases $\%\dot{m}_{\mathrm{g,net}}$ for the bottom gaps but does not improve it for the top gaps. The 50% inlet size is a significant improvement over the base inlet size, where Gaps 10 to 15 never received adequate airflow. When $\%\dot{m}_{\mathrm{g,net}}$ is above 2, $T_{\mathrm{g,max}}$ is reduced below 60°C.

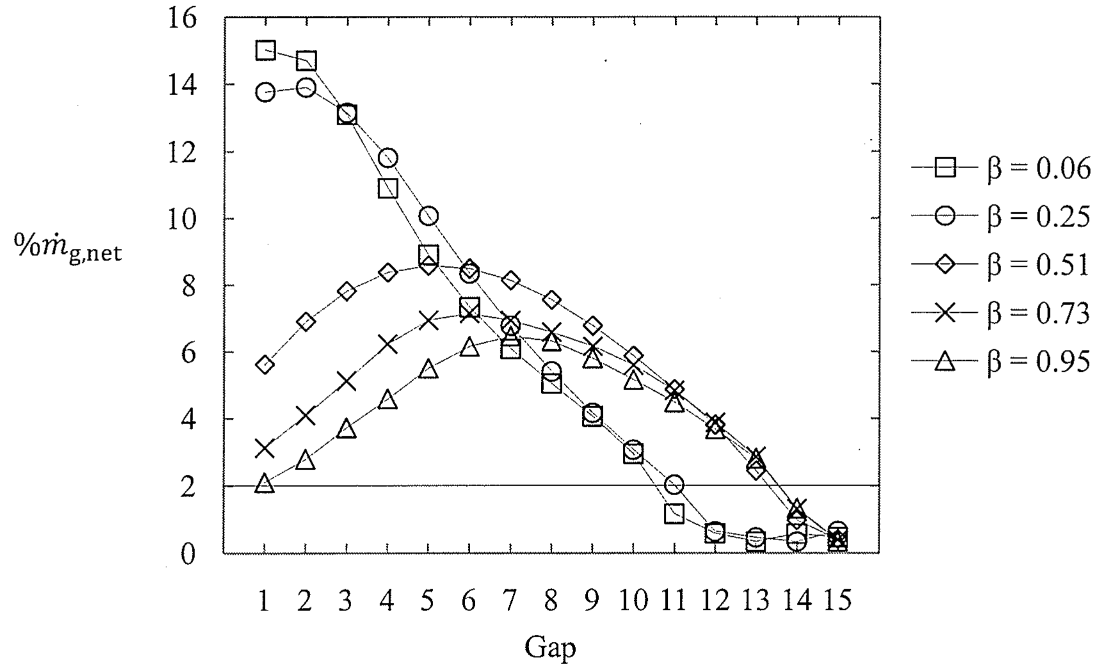

Figure 5-40: $\%\dot{m}_{g,net}$ for all tower gaps (Cases 13, 15, 17, 19, and 21)

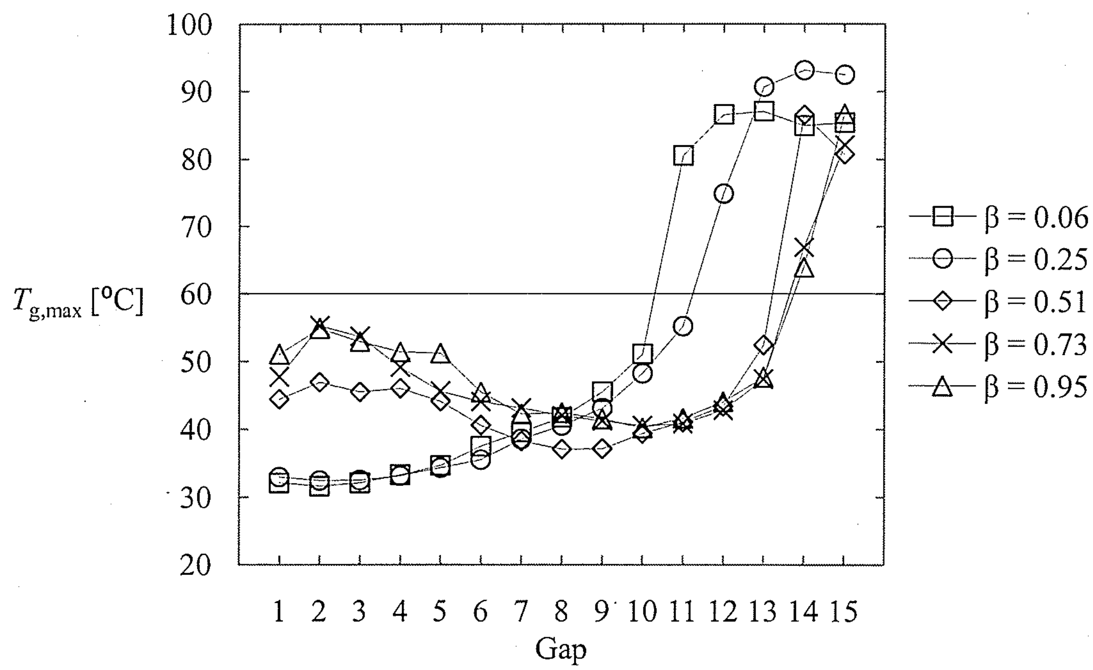

Figure 5-41: $T_{g,max}$ for all tower gaps (Cases 13, 15, 17, 19, and 21)

5.3.3.2: The Effect of β for the Low Tower, Cases 14, 16, 18, 20, and 22

The profiles of $\%\dot{m}_{g,net}$ and $T_{g,max}$ at all tower gaps are shown in Figures 5-42 and 5-43, respectively, for Cases 14, 16, 18, 20, and 22. When β is in the range of 0.06 to 0.25, $\%\dot{m}_{g,net}$ is above 2 for the bottom 9-12 gaps and is below 2 for the top 3-6 gaps. When β is in the range of 0.73 to 0.95, $\%m_{g,net}$ is below 2 for the bottom 3-5 gaps and is above 2 for the top 10-12 gaps. When β is set at 0.51 there is insufficient airflow at Gaps 1, 2, and 15, but sufficient airflow from Gaps 3 to 14. For the low tower cases the jet velocity is strong enough to reach to top tower gaps but there is no β where the jet covers every gap. This is similar to what was observed for the low tower cases with the 25% inlet size. When $\%\dot{m}_{g,net}$ is above 2, $T_{g,max}$ is reduced below 60°C.

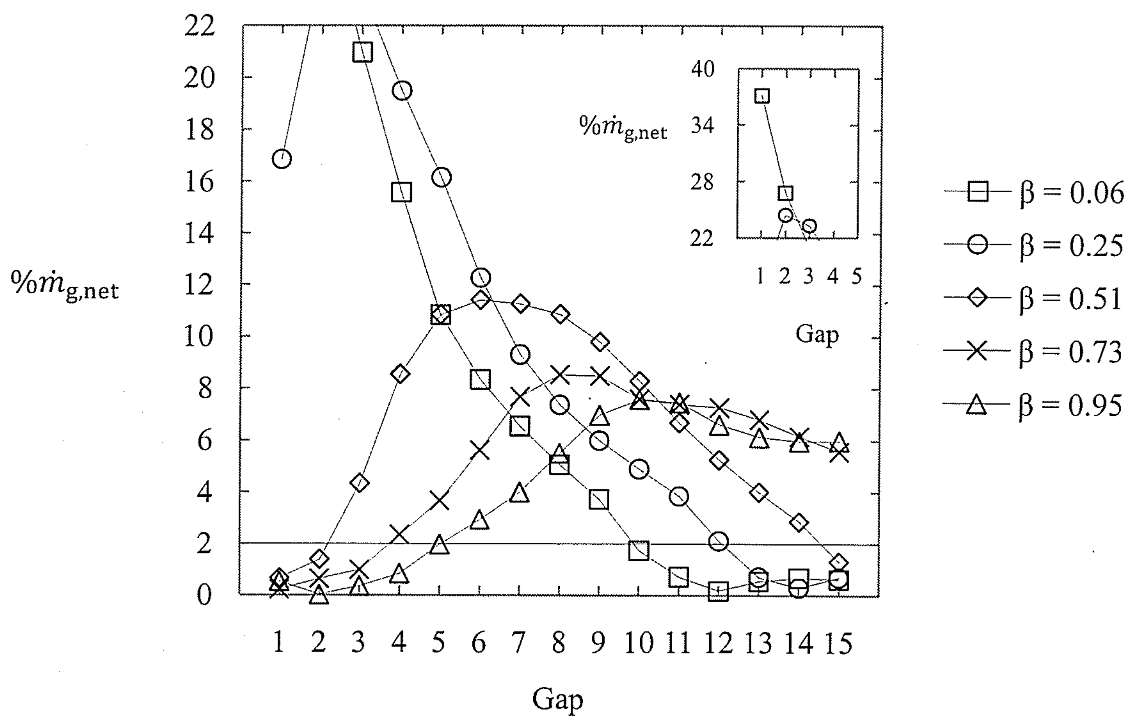

Figure 5-42: $\%\dot{m}_{g,net}$ for all tower gaps (Cases 14, 16, 18, 20, and 22)

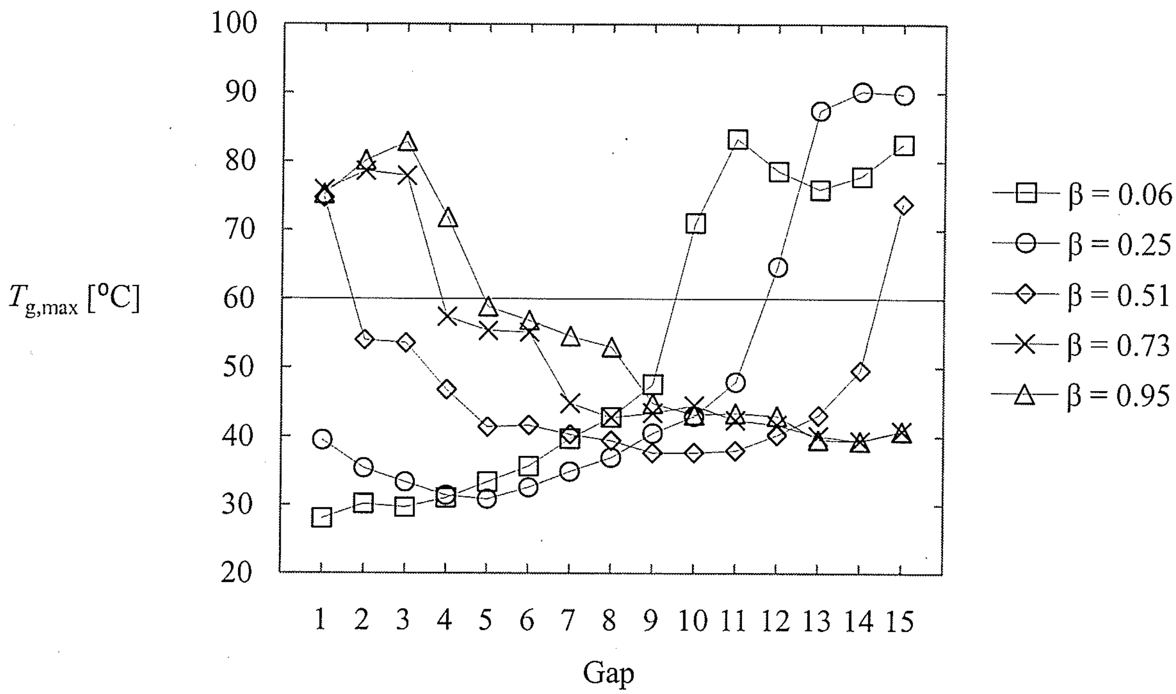

Figure 5-43: $T_{g,max}$ for all tower gaps (Cases 14, 16, 18, 20, and 22)

5.3.3.3: Summary of the Effect of β for Inlet Shape 2

The profile of $\sum\%\dot{m}_{g,net}$ as β is varied for both the high and low towers is shown in Figure 5-44. For both tower elevations, the highest value of $\sum\%\dot{m}_{g,net}$ occurs at β = 0.25. This location is consistent with what was observed for the previous cases. The low tower cases have higher values of $\sum\%\dot{m}_{g,net}$ relative to the high tower for all β values. The difference in $\sum\%\dot{m}_{g,net}$ between the two tower heights decreases as β increases.

The profile of $T_{t,av}$ as β is varied for both the high and low towers is shown in Figure 5-45. For both tower elevations, the lowest value of $T_{t,av}$ occurs at β = 0.51 and at this condition, there is relatively no difference between the two towers. This is a different location from where the highest $\sum\%\dot{m}_{\mathrm{g,net}}$ value was observed and is inconsistent with what was observed in the previous cases.

The profile for $T_{\mathrm{t,max}}$ as β is varied for both the high and low towers is shown in Figure 5-46. Irrespective of the tower elevation and for all values of β, $T_{\mathrm{t,max}}$ is above 60 °C. This is a result of the air jet always providing insufficient airflow to some gaps irrespective of β or tower elevation. The low tower cases have slightly lower values for $T_{\mathrm{t,max}}$ relative to the high tower cases.

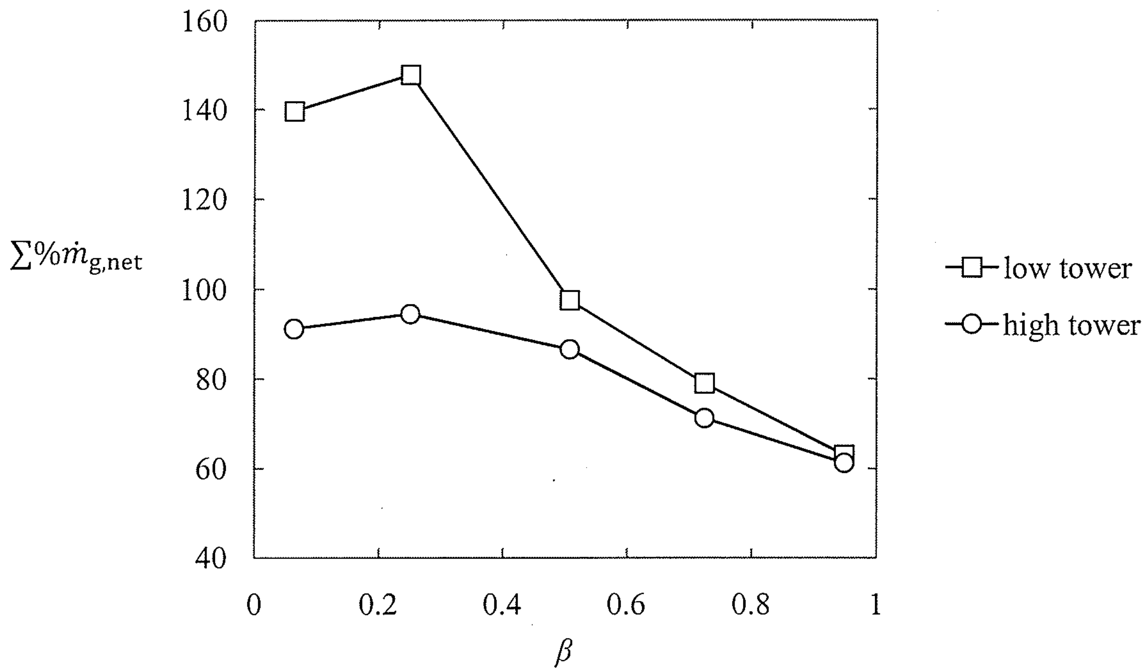

Figure 5-44: $\sum\%\dot{m}_{\mathrm{g,net}}$ vs. β (Cases 13 to 22)

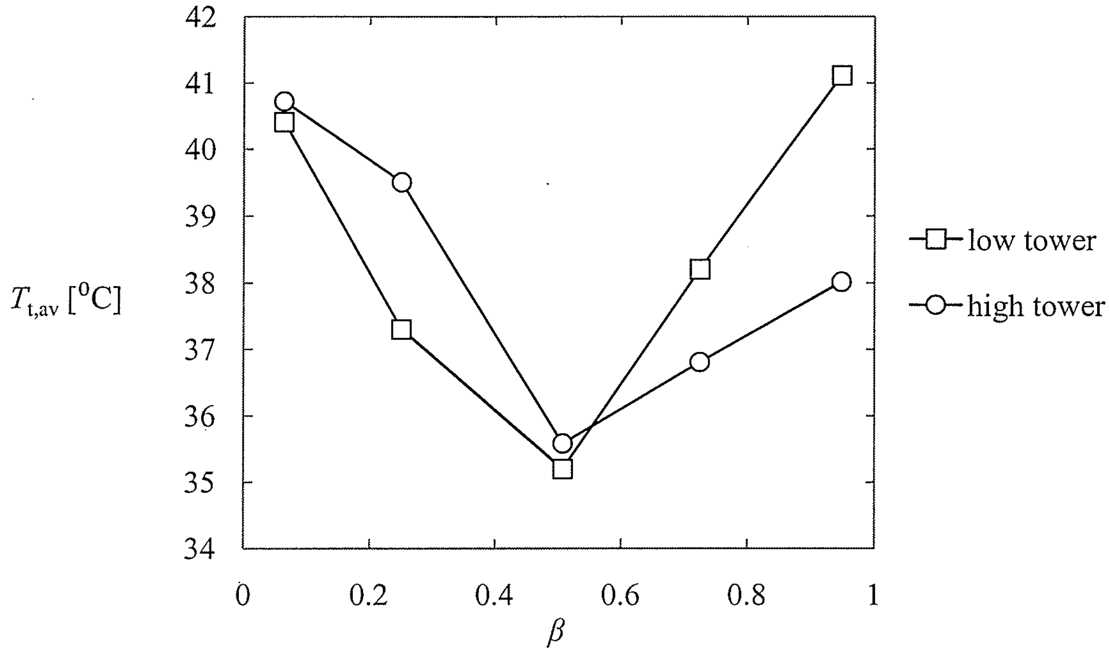

Figure 5-45: $T_{t,av}$ vs. β (Cases 13 to 22)

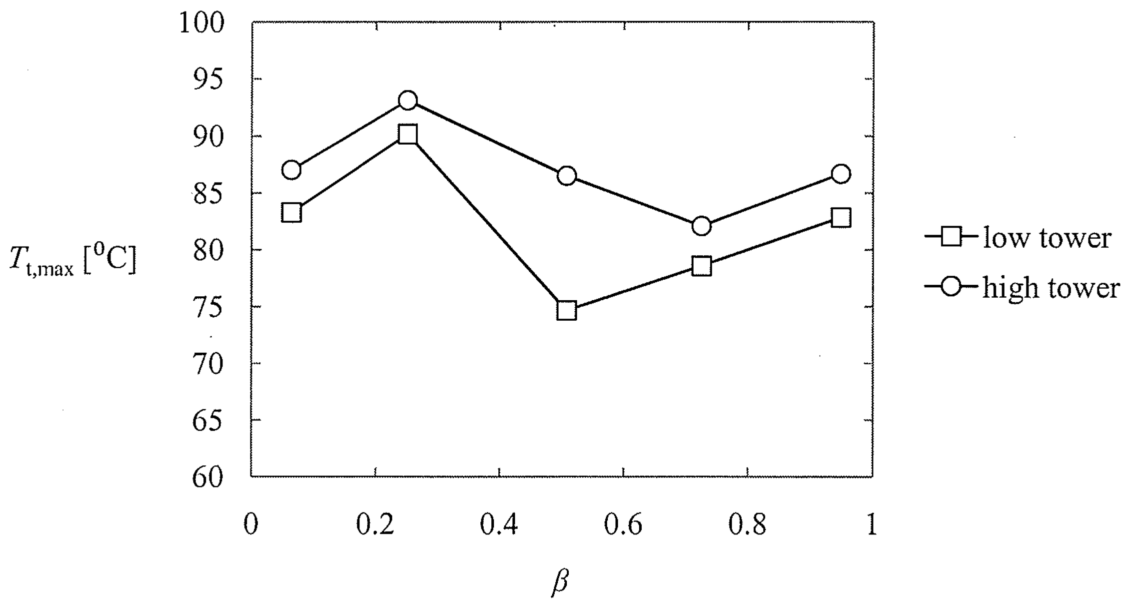

Figure 5-46: $T_{t,max}$ vs. β (Cases 13 to 22)

A summary of the results for the cases with inlet shape 2 are provided in Table 5-5. For both tower heights, the most advantageous results occurred when the jet was aimed at a β of 0.51. At this β, thirteen gaps were cooled below 60 °C. For both height conditions, complete tower coverage could not be achieved, but for different reasons.

- For the high tower cases, the jet velocity is not strong enough to reach the top of the tower.
- For the low tower cases, the jet velocity can reach the top tower gaps, but the jet cannot be angled to cover the entire tower.

Table 5-5: Summary of key results from Cases 13 to 22

Case	θ [deg]	β	Tower Type	$T_{t,max}$ [^{o}C]	No. of gaps with $T_{g,max}$ > 60 [^{o}C]	$T_{t,av}$ [^{o}C]	$\sum\%\dot{m}_{g,net}$
13	77.4	0.06	High Tower	87.0	5	40.4	91.2
15	80.7	0.25		93.1	4	39.5	94.5
17	83.2	0.51		86.5	2	35.6	86.6
19	84.5	0.73		82.1	2	36.8	71.2
21	85.4	0.95		86.7	2	38.0	61.2
14	60	0.06	Low Tower	82.5	6	40.4	139.6
16	70	0.25		90.2	4	37.3	147.8
18	80	0.51		74.7	2	35.2	97.5
20	82.5	0.73		78.6	3	38.2	79.0
22	84	0.95		82.8	4	41.1	63.0

5.3.4: The Effect of Different Inlet Shapes, Cases 32 to 35

In this section, inlets with different geometries will be compared for the high tower with β = 0.51. In Figure 5-47, the size of the inlet is decreased by varying both L_x and L_y. In Figure 5-48 the size of the inlet is reduced by varying L_y while holding L_x constant at the base length.

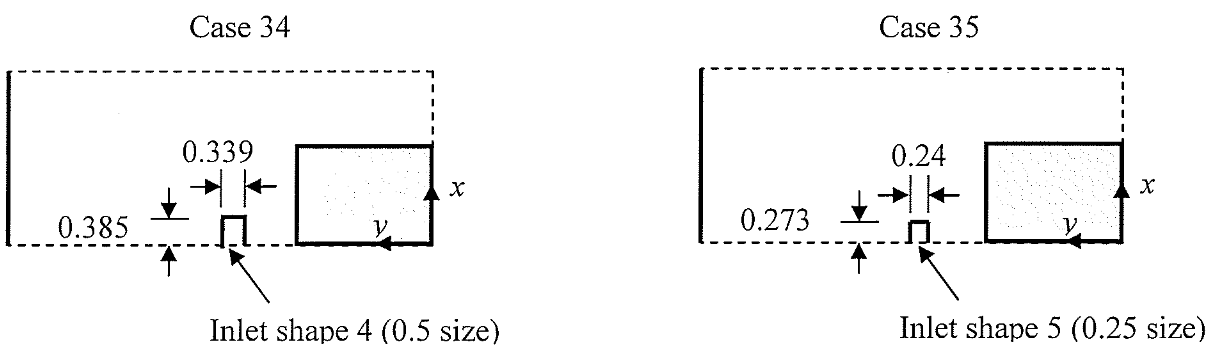

Figure 5-47: Top view of domain showing the inlet geometries that will be compared when both the width L_x and length L_y are varied (Cases 34 and 35). Dimensions are in meters.

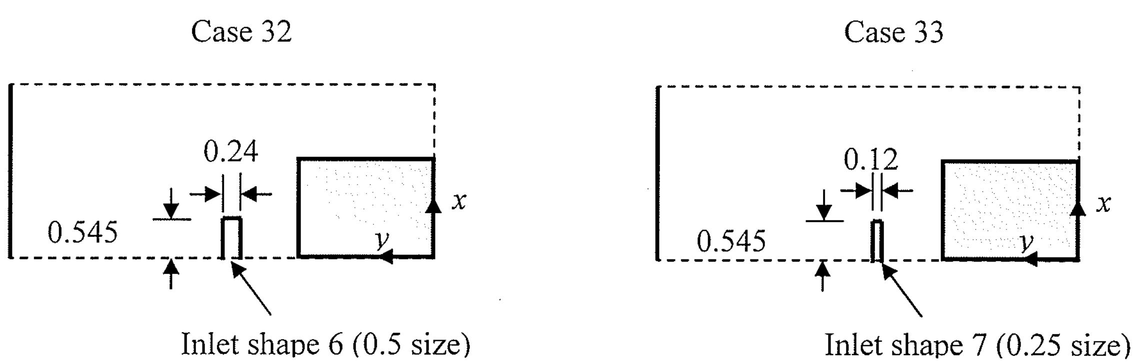

Figure 5-48: Top view of domain showing the inlet geometries that will be compared when both the width L_x and length L_y are varied (Cases 32 and 33). Dimensions are in meters.

The profiles of $\%\dot{m}_{g,net}$ and $T_{g,max}$ at all tower gaps are shown in Figures 5-49 and 5-50, respectively, for inlet shape 3, 5, and 7. All these shapes correspond to a 0.25 inlet size. Only when the inlet shape 3 is utilized do all of the gaps receive $\%\dot{m}_{g,net}$ values above the threshold value of 2. For inlet shapes 5 and 7, $\%\dot{m}_{g,net}$ drops below 2 at the top tower gaps. When $\%\dot{m}_{g,net}$ is above 2, $T_{g,max}$ is reduced below 60°C.

The profiles of $\%\dot{m}_{g,net}$ and $T_{g,max}$ at all tower gaps are shown in Figures 5-51 and 5-52, respectively, for inlet shapes 2, 4, and 6. All these shapes correspond to a 0.5 inlet size. For all three cases, $\%\dot{m}_{g,net}$ drops below 2 at Gap 14 and 15. There is relatively little difference in the profiles for all inlet shape. When $\%\dot{m}_{g,net}$ is above 2, $T_{g,max}$ is reduced below 60°C.

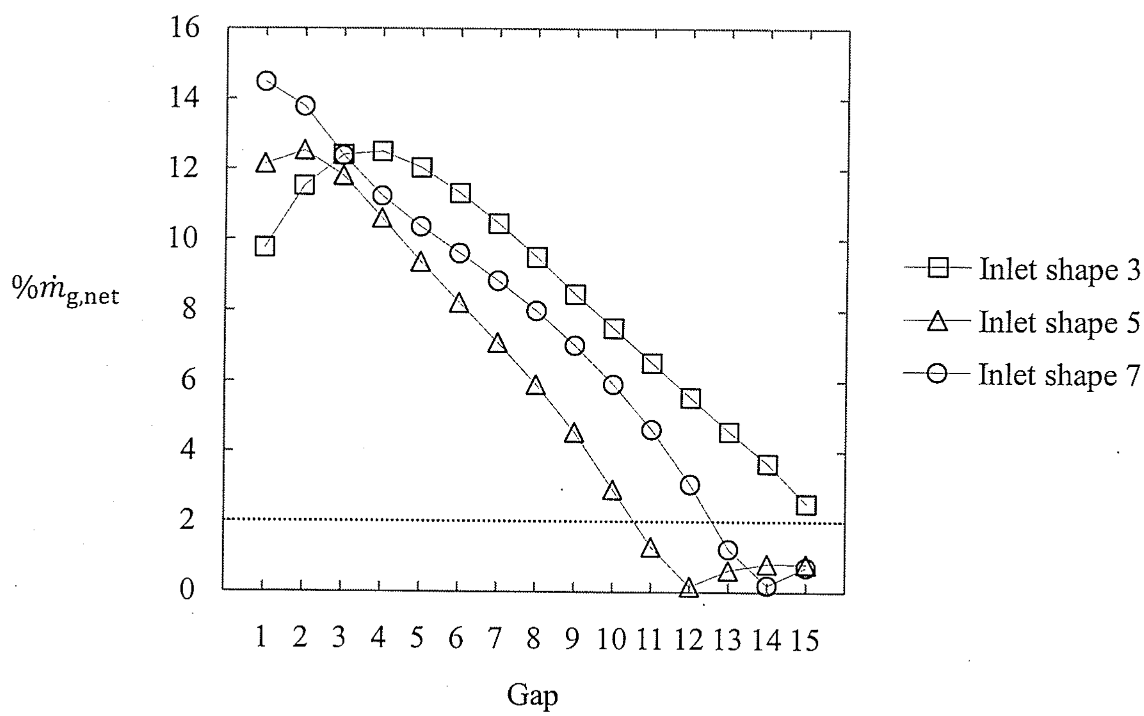

Figure 5-49: $\%\dot{m}_{g,net}$ for all tower gaps (Cases 27, 33, and 35)

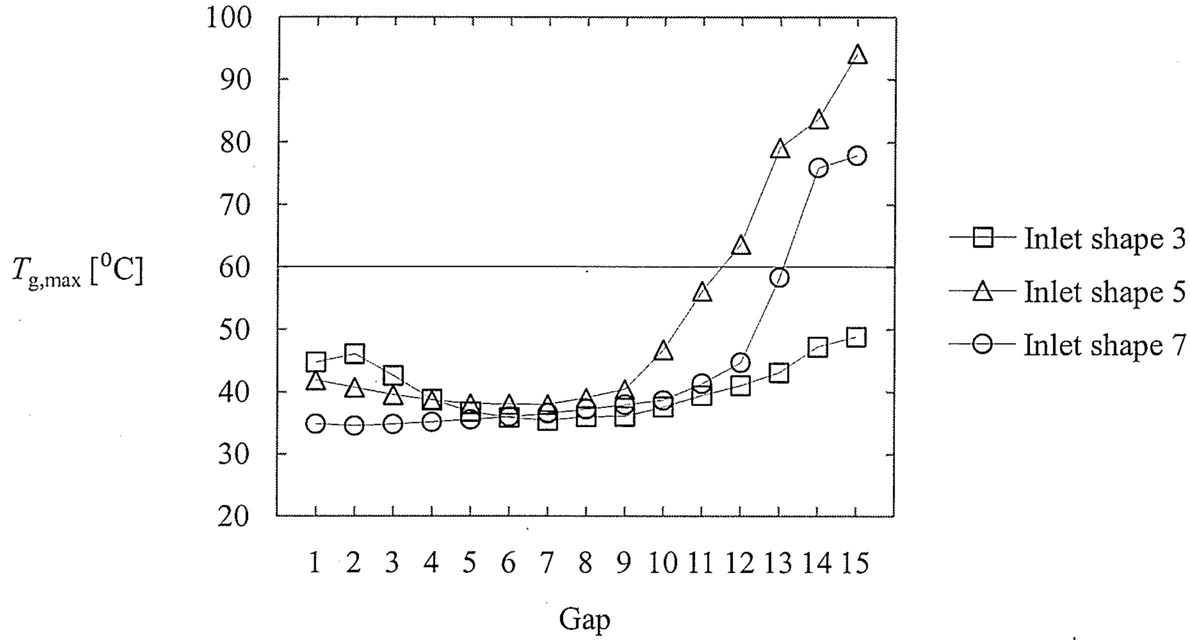

Figure 5-50: $T_{g,max}$ for all tower gaps (Cases 27, 33, and 35)

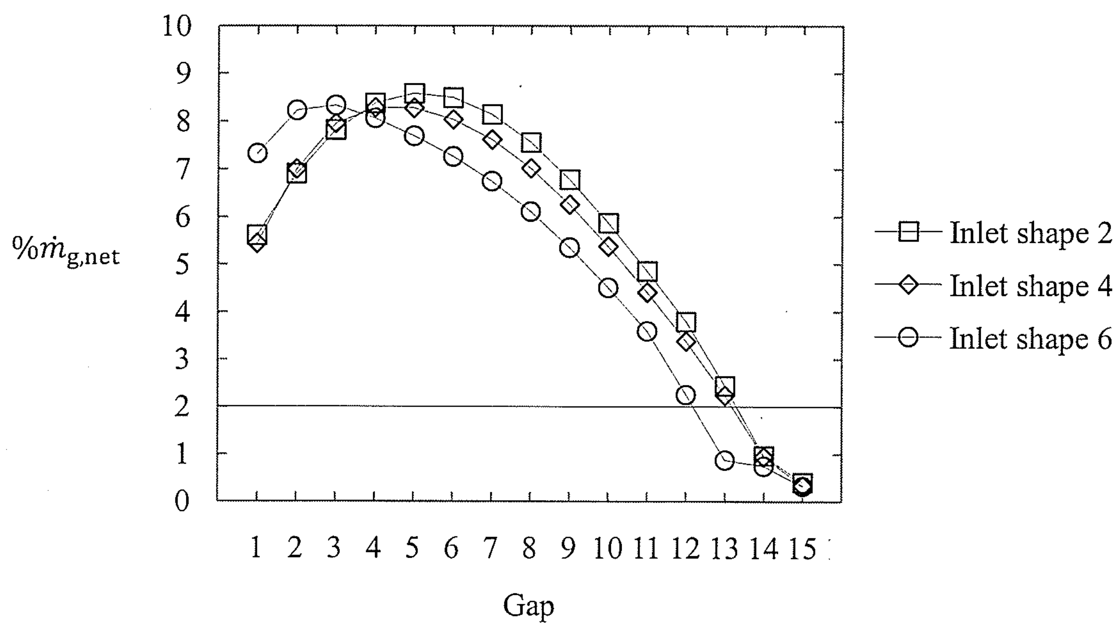

Figure 5-51: $\%\dot{m}_{g,net}$ for all tower gaps (Cases 17, 32, and 34)

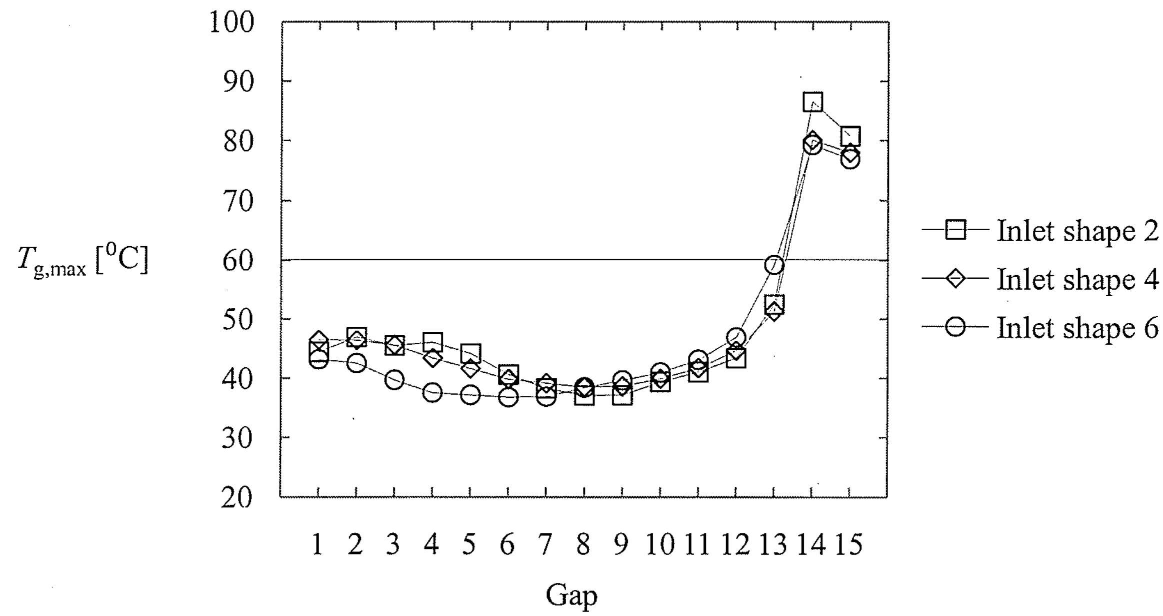

Figure 5-52: $T_{g,max}$ vs. for all tower gaps (Cases 17, 32, and 34)

The results from this section are summarized in Table 5-6. It can be concluded that when the inlet size is reduced to 0.5 of the base size, the aspect ratio of the inlet will not be a factor in the cooling effectiveness. If the inlet is reduced to 0.25 of the base size, the aspect ratio of the inlet will have an effect on the ventilation of the tower. In general when the inlet area is relatively small, it should be designed to be as wide as possible in the y-direction.

Table 5-6: Summary of key results from Cases 32 to 35

Case	L_y [m]	L_x [m]	$T_{t,max}$ [°C]	No. of gaps with $T_{g,max}$ > 60 [^{0}C]	$T_{t,av}$ [°C]	$\sum\%\dot{m}_{g,net}$
32	0.385	0.339	80.1	2	35.7	82.5
33	0.12	0.273	94.2	4	39.6	87.4
34	0.24	0.545	79.3	2	35.8	70.1
35	0.12	0.545	77.9	2	35.3	96.8

5.3.5: Summary of the Effect of Inlet Geometry

It was shown in Section 5.3.1 that there is a trend whereby decreasing the inlet size, increases $\%\dot{m}_{\mathrm{g,net}}$ and decreases $T_{\mathrm{t,av}}$. In Section 5.3.4, the aspect ratio of the inlet was found to have a minor effect on the effectiveness of the tower ventilation when the inlet was 0.5 of the base inlet size. The aspect ratio was found to be a significant factor in the tower ventilation when the inlet area was 0.25 of the base inlet area. At this size it was advantageous for the inlet to be longer in the y-direction than in the x-direction. A comparison of the effect of inlet shape for $\sum\%\dot{m}_{\mathrm{g,net}}$, $T_{\mathrm{t,av}}$, and $T_{\mathrm{t,max}}$ as β is varied for the high and low towers can be found in Appendix C.

The following observations can be made regarding the inlet geometry for the high tower cases:

- Reducing the inlet size will in general improve the ventilation by increasing the number of gaps with $\%\dot{m}_{\mathrm{g,net}}$ values above 2. When an inlet shape 3 (0.25 size) was implemented along with a β value at or above 0.25, all tower gaps had $\%\dot{m}_{\mathrm{g,net}}$ values above 2.
- When an inlet shape 2 (0.5 size) was implemented, the jet velocity was not strong enough to sufficiently push airflow into Gaps 14 and 15.
- For all inlet sizes, the bottom gaps always received sufficient airflow, irrespective of the value of β.

The following observations can be made regarding the inlet geometry for the low tower cases:

- For the low tower, reducing the inlet size from the base inlet size to inlet shape 2 (0.5 size) improved the tower ventilation.

- Reducing the inlet from shape 2 (0.5 size) to shape 3 (0.25 size) had a minimal effect on improving the ventilation. For both of these inlet sizes, the jet velocity was strong enough to sufficiently push airflow into the top tower gaps, and for both inlet sizes a minimum of two tower gaps had $T_{\mathrm{g,max}}$ values above 60°C.
- For all inlet sizes, the jet could not be angled in a way that can supply all of the gaps sufficient airflow. In general, when the jet was aimed low the top gaps received insufficient airflow and when the jet was aimed high the bottom gaps received insufficient airflow.

5.4: The Effect of Inlet Location

This section presents the results from cases where the location of the inlet was changed by varying the parameter P_y. In Section 5.4.1, the inlet location was moved closer to the tower. In these cases, a higher θ was required for the same β on the tower. In Section 5.4.2, the inlet was moved farther away from the tower. In these cases, a lower θ was required for the same β on the tower.

5.4.1: The Effect of Moving the Inlet Closer to the Tower: Cases 45-48

In a previous section, it was shown that when an inlet shape 3 was utilized on the high tower along with a $\beta \geq 0.25$, all tower gaps were cooled below 60°C. The same ventilation results could not be duplicated for the low tower. A contributing factor to the better cooling observed for the high tower was that θ was higher, allowing the jet to flow upward along the tower and spread the airflow over more gaps. The jet angle for the low tower required to hit the equivalent location on the tower was smaller, causing the airflow to be localized. In this section, for the low tower only, the jet will be aimed at a $\beta = 0.51$ and the inlet will be moved closer to the tower, causing the inlet jet angle to increase from 80° to 83.2°. This new angle corresponds to the angle from a high tower case that sufficiently cooled all tower gaps. The jet target path for the low tower with the inlet closer to the tower and base location is shown in Figure 5-53.

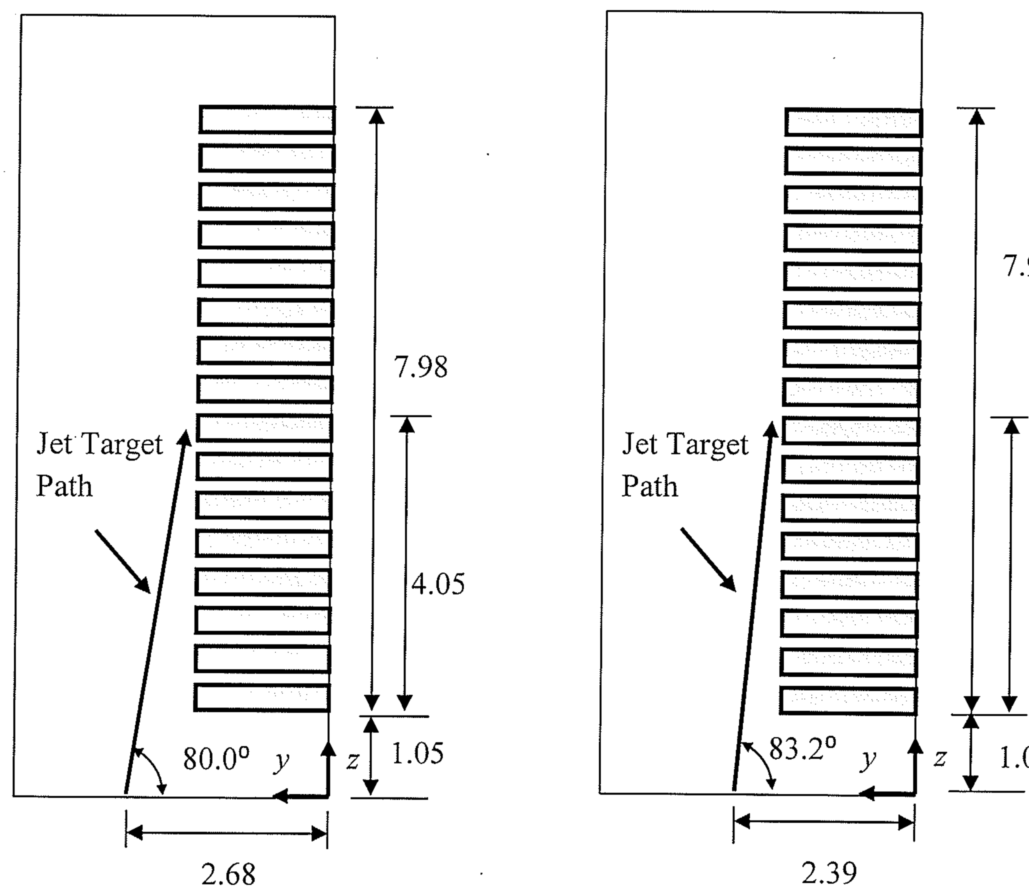

(a) Base inlet location for Cases 8, 18, and 28

(b) Close inlet location for Cases 46 to 48

Figure 5-53: Side view showing the jet target path for the base and close inlet locations. Dimensions are in meters.

The profiles of $\%\dot{m}_{g,net}$ and $T_{g,max}$ at all tower gaps are shown in Figures 5-54 and 5-55, respectively, for Cases 8 and 46. The inlet size studied in these cases is the base inlet size. Moving the inlet closer to the tower reduces the maximum $\%\dot{m}_{g,net}$ value. This is a result of the higher jet angle reducing the v-component of the velocity. Although the maximum $\%\dot{m}_{g,net}$ value is reduced, the airflow is spread out over more gaps and the bottom two gaps now have $\%\dot{m}_{g,net}$ values above the threshold. This increases the number of gaps with $T_{g,max}$ values below 60°C from nine to eleven. From Gaps 12 to 15, $T_{g,max}$ is reduced but is still above 60°C.

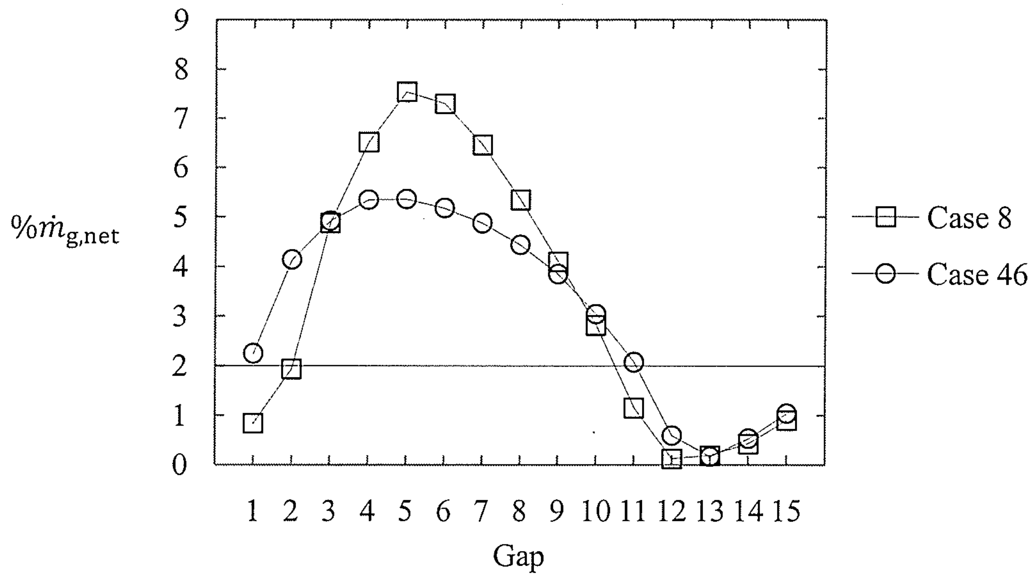

Figure 5-54: $\%\dot{m}_{g,net}$ for all tower gaps (Cases 8 and 46)

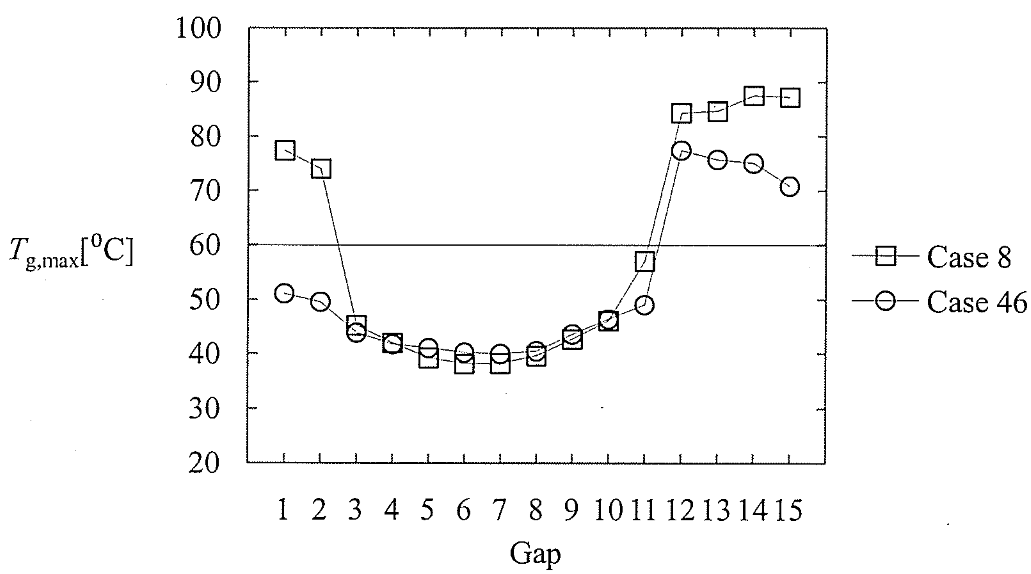

Figure 5-55: $T_{g,max}$ for all tower gaps (Cases 8 and 46)

The profiles of $\%\dot{m}_{g,net}$ and $T_{g,max}$ at all tower gaps are shown in Figures 5-56 and 5-57, respectively, for Cases 18 and 47. The inlet geometry for these cases is shape 2 (0.5 inlet size). Moving the inlet closer to the tower reduced the maximum $\%\dot{m}_{g,net}$ value, but the airflow is now spread out over the entire tower and the value of $\%\dot{m}_{g,net}$ is above 2 for all tower gaps. This is the first low-tower case where all gaps have $T_{g,max}$ values that are below 60°C. And this is the first case for both tower elevations where a shape 2 inlet could sufficiently cool all fifteen tower gaps.

The streamlines entering all tower gaps show the characteristics of type 1 when the inlet is close to the tower and the inlet area is 0.5 the base size. The type 1 streamlines entering Gap 15 for Case 46 are shown in Figure 5-58. For Case 46 at Gap 15, the values of $\%\dot{m}_{g,net}$ and $T_{g,max}$ are 5.2 and 42.1°C, respectively. When the inlet is at the base location, the streamlines at Gap 15 show the characteristics of type 2. The type 2 streamlines entering Gap 15 for Case 18 are shown in Figure 5-59. The jet velocity is no longer strong enough to completely push airflow into this gap. For Case 18 at Gap 15, the values of $\%\dot{m}_{g,net}$ and $T_{g,max}$ are 1.3 and 73.8°C, respectively. This demonstrates how changing the inlet location can influence the interaction of the ventilation system with the tower gaps.

Comparisons between the base inlet location and the close inlet location in terms of the profiles of $\sum\%\dot{m}_{g,net}$, $T_{t,av}$, and $T_{t,max}$ at various L_x are shown in Figures 5-60, 5-61 and 5-62, respectively. Moving the inlet closer to the tower had relatively no effect on $\sum\%\dot{m}_{g,net}$ for all L_x. Moving the inlet closer to the tower lowered the values of $T_{t,av}$ and $T_{t,max}$ for all values of L_x.

With the close inlet location, $T_{t,max} \leq 60°C$ was achieved at $L_x = 0.136$ [m] (0.25 inlet) and 0.273 [m] (0.5 inlet).

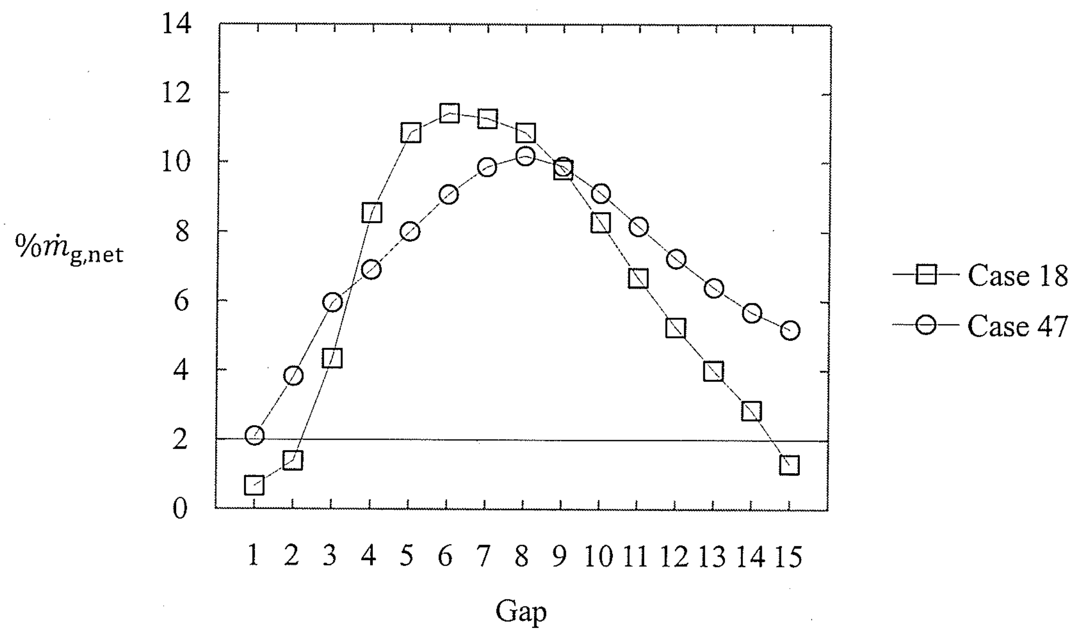

Figure 5-56: $\%\dot{m}_{g,net}$ for all tower gaps (Cases 18 and 47)

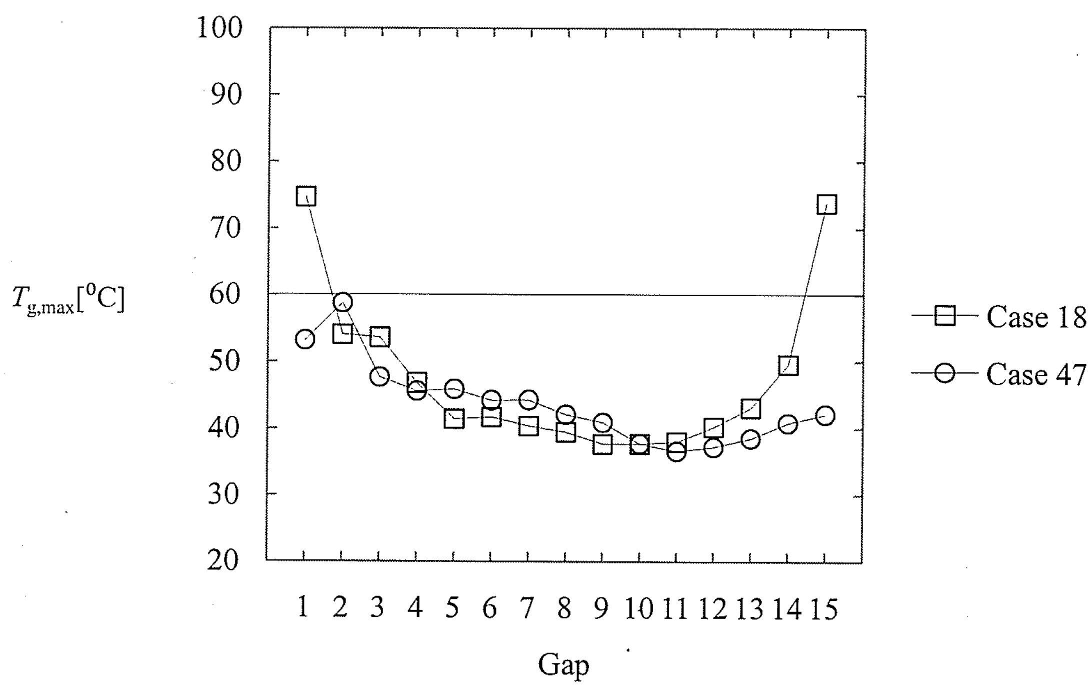

Figure 5-57: $T_{g,max}$ for all tower gaps (Cases 18 and 47)

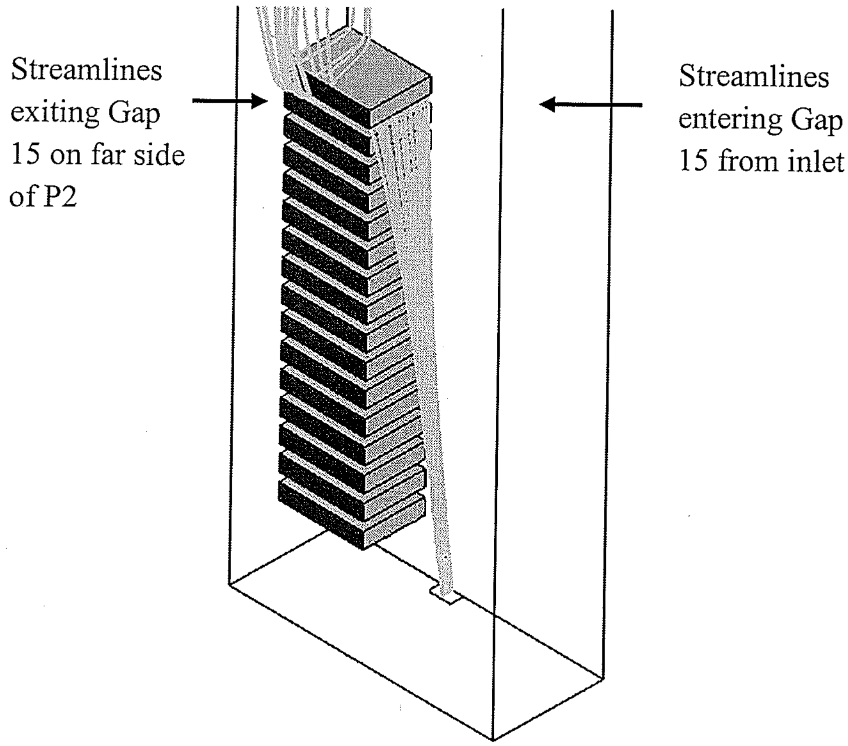

Figure 5-58: Type 1 streamlines entering Gap 15 on plane P1 (Case 47)

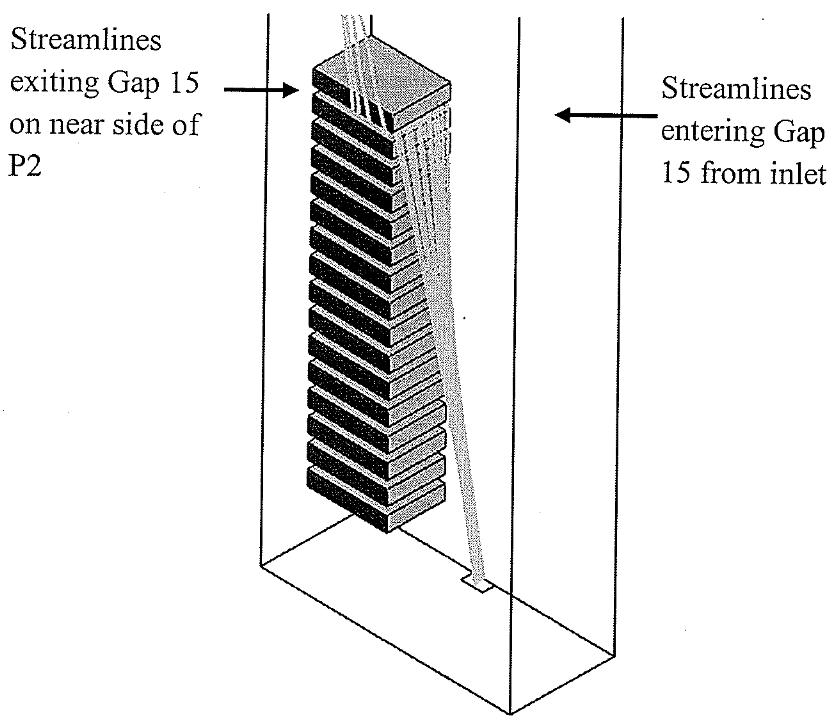

Figure 5-59: Type 2 streamlines entering Gap 15 on plane P1 (Case 18)

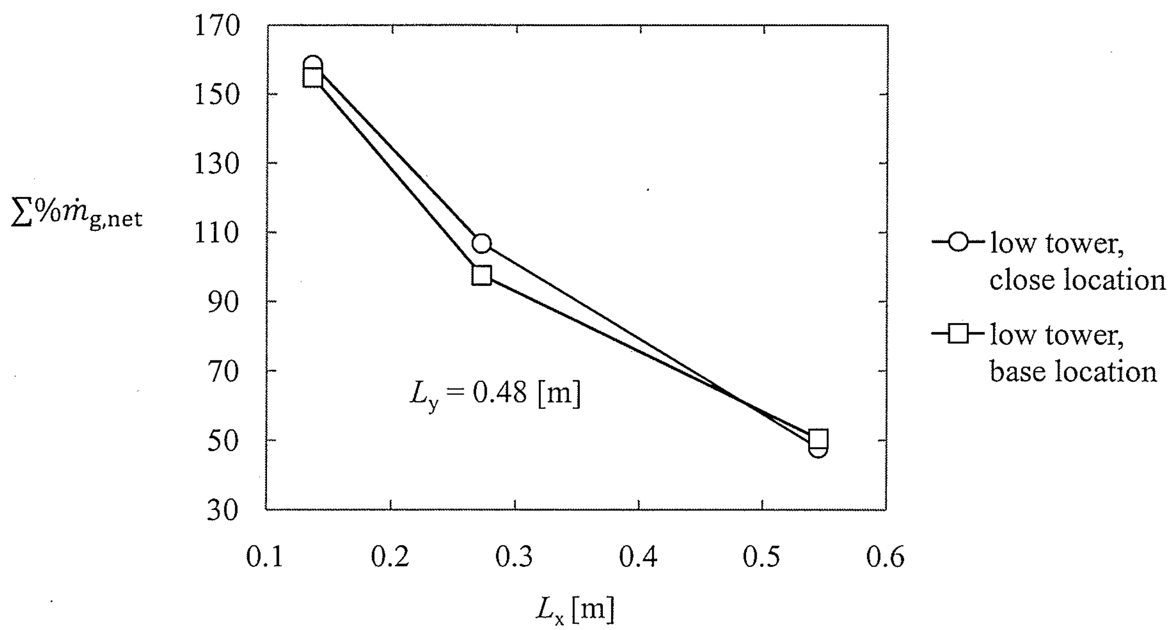

Figure 5-60: $\sum\%\dot{m}_{g,net}$ vs. L_x (Cases 8, 18, 28, and 46 to 48)

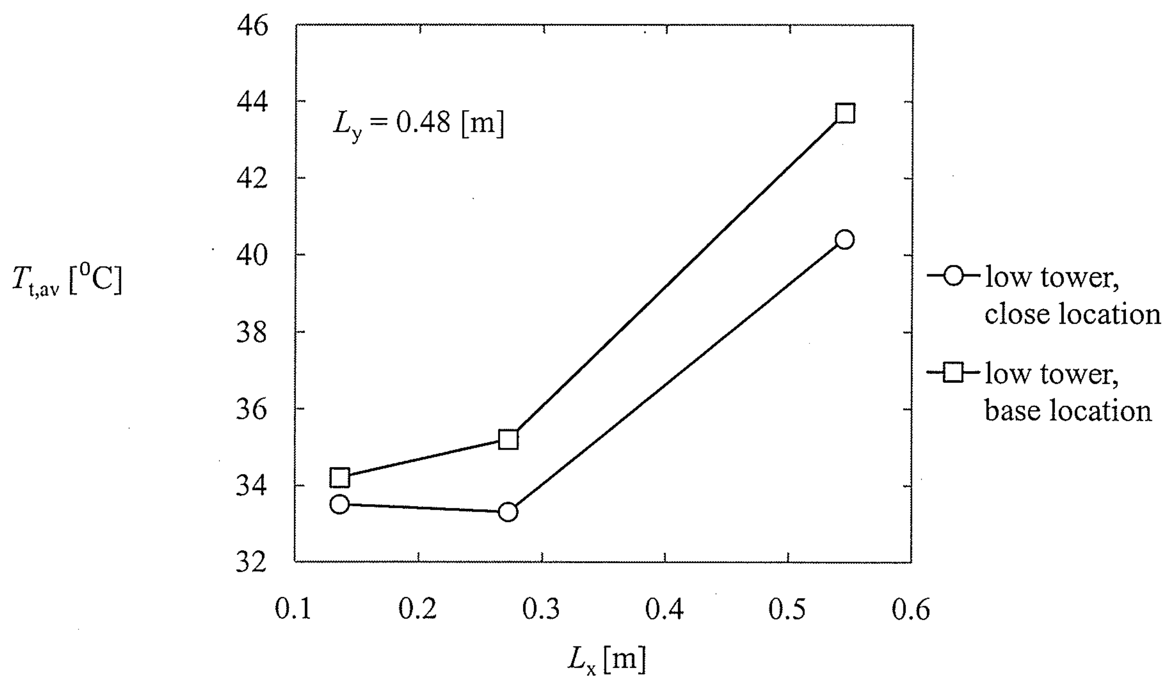

Figure 5-61: $T_{t,av}$ vs. L_x (Cases 8, 18, 28, and 46 to 48)

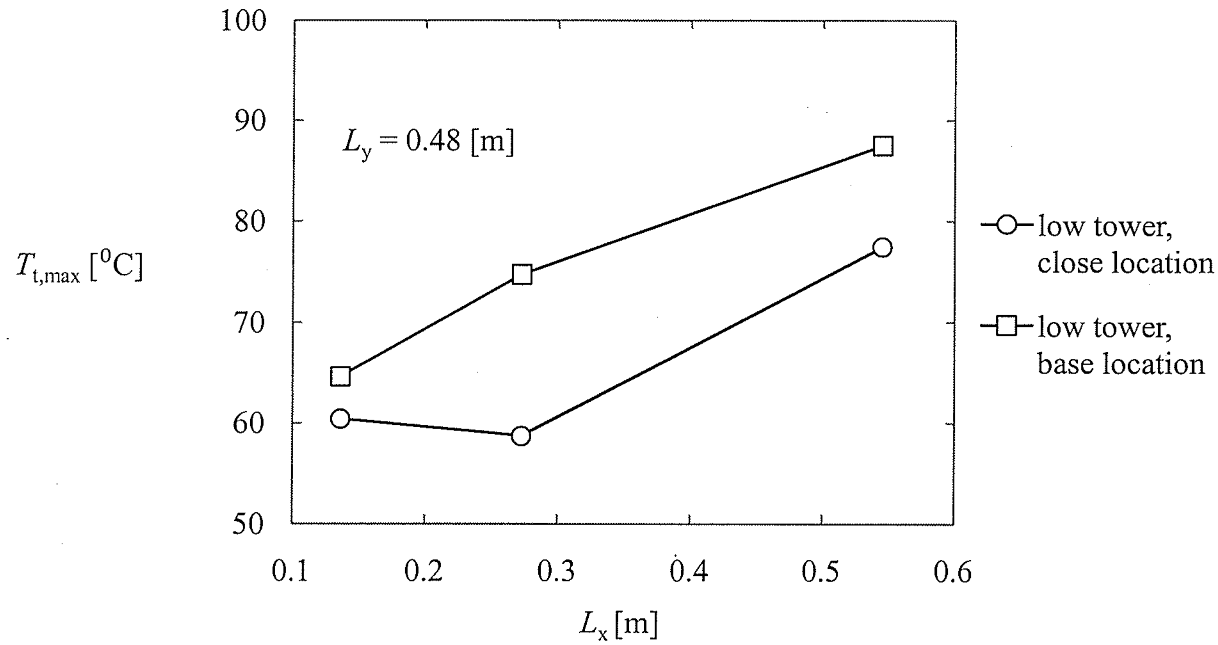

Figure 5-62: $T_{t,max}$ vs. L_x (Cases 8, 18, 28, and 46 to 48)

The results from this section are summarized in Table 5-7. It can be concluded that for the low tower, moving the inlet closer to the tower will be beneficial to the ventilation system. It was observed that all tower gaps were cooled below 60°C with a 0.5 size inlet. For the 0.25 size inlet $T_{t,max}$ was 60.4°C which is very close to the criterion of 60°C. Similar results cannot be duplicated for the high tower using that inlet size. The reason that a 0.5 inlet will not completely cool the high tower is that the jet velocity will always decay below an effective level by the time it reaches the top gaps. Since the low tower is closer to the ground, the airflow from a 0.5-size inlet has the potential of reaching the top of the tower at a velocity strong enough to push air into the top gaps.

Table 5-7: Summary of key results from Cases 8, 18, 28, and 46 to 48

Case	L_x [m]	θ [deg]	β	$P_{x,i}$ [m]	$T_{t,max}$ [°C]	No. of gaps with $T_{g,max}$ > 60 [°C]	$T_{t,av}$ [°C]	$\sum\%\dot{m}_{g,net}$
46	0.545				77.4	4	40.4	47.8
47	0.273	83.2°	0.51	2.68	58.7	0	33.3	106.7
48	0.136				60.4	1	33.5	158.3
8	0.545				87.5	6	43.7	50.5
18	0.273	80°	0.51	2.39	74.7	2	35.2	97.5
28	0.136				64.6	2	34.2	154.8

5.4.2: The Effect of β when the Inlet is Far Away from the Tower, Cases 36 to 45

This section discusses the effect of β on tower cooling when the inlet is farther away from the tower and the inlet is shape 3 (0.25-size inlet). The results from the high and low towers will be presented separately and the section will be concluded with a comparison between the results at the base inlet location and the far inlet location. Moving the inlet farther away from the tower while keeping β the same results in a lower θ. The airflow is now required to travel a greater distance to reach the tower, which causes more decay in the jet velocity. A top view of the inlet geometry and inlet location used in this section is shown in Figure 5-63.

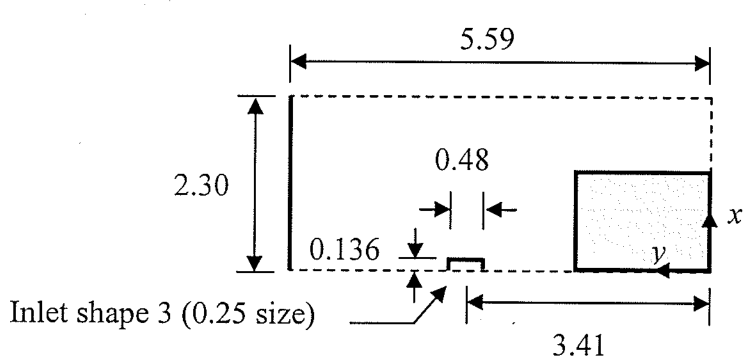

Figure 5-63: Top view of domain showing the inlet geometry and location for Cases 36 to 45. Dimensions are in meters.

5.4.2.1: The Effect of β for the High Tower, Cases 36, 38, 40, 42, and 44

The jet inlet angle for the high tower cases in this section is varied from 68° to 81.6°. The profiles for $\%\dot{m}_{g,net}$ and $T_{g,max}$ at all tower gaps for Cases 36, 38, 40, 42, and 44 are shown in Figures 5-64 and 5-65, respectively. When β is in the range of 0.06 to 0.51, airflow does not significantly penetrate the top three tower gaps. When β is in the range of 0.73 to 0.95, airflow does not significantly penetrate the bottom gap. These are the first high tower cases where the bottom gap is missed by the jet. For all values of β, Gaps 14 and 15 will not receive adequate airflow. The increased distance between the inlet and the tower is sufficient to decay the jet velocity to the point where the airflow cannot penetrate Gaps 14 and 15. In contrast to the cases where the inlet is at the base location, there is no value for β where all of the tower gaps will receive sufficient airflow. When $\%\dot{m}_{g,net}$ is above 2, $T_{g,max}$ is reduced below 60°C.

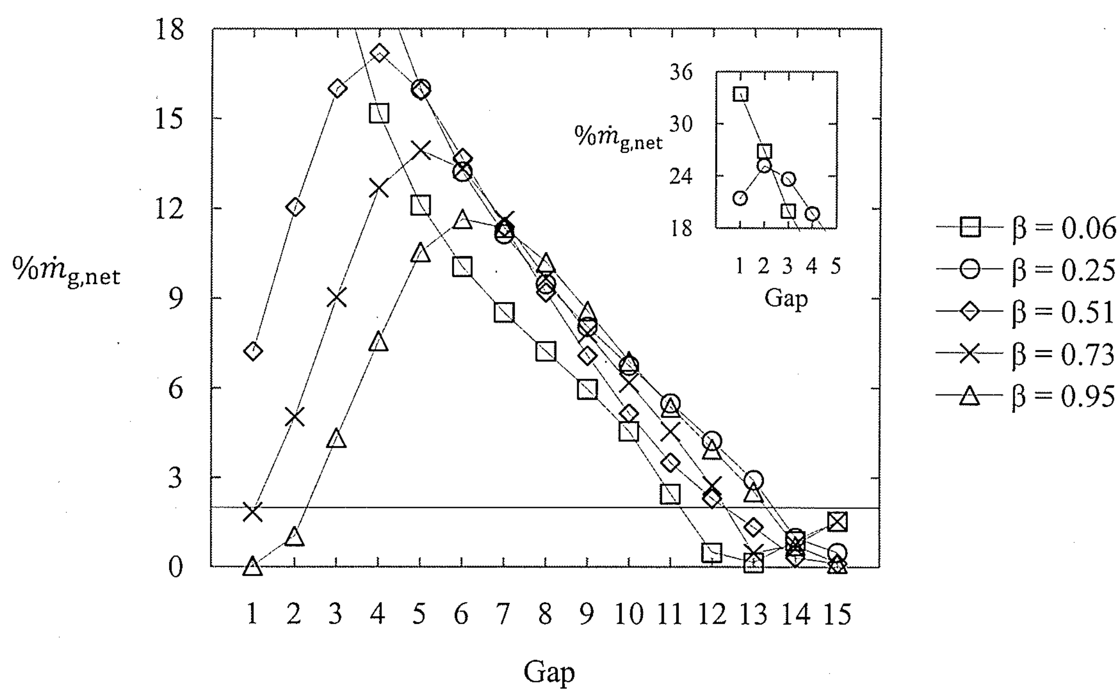

Figure 5-64: $\%\dot{m}_{g,net}$ for all tower gaps (Cases 36, 38, 40, 42, and 44)

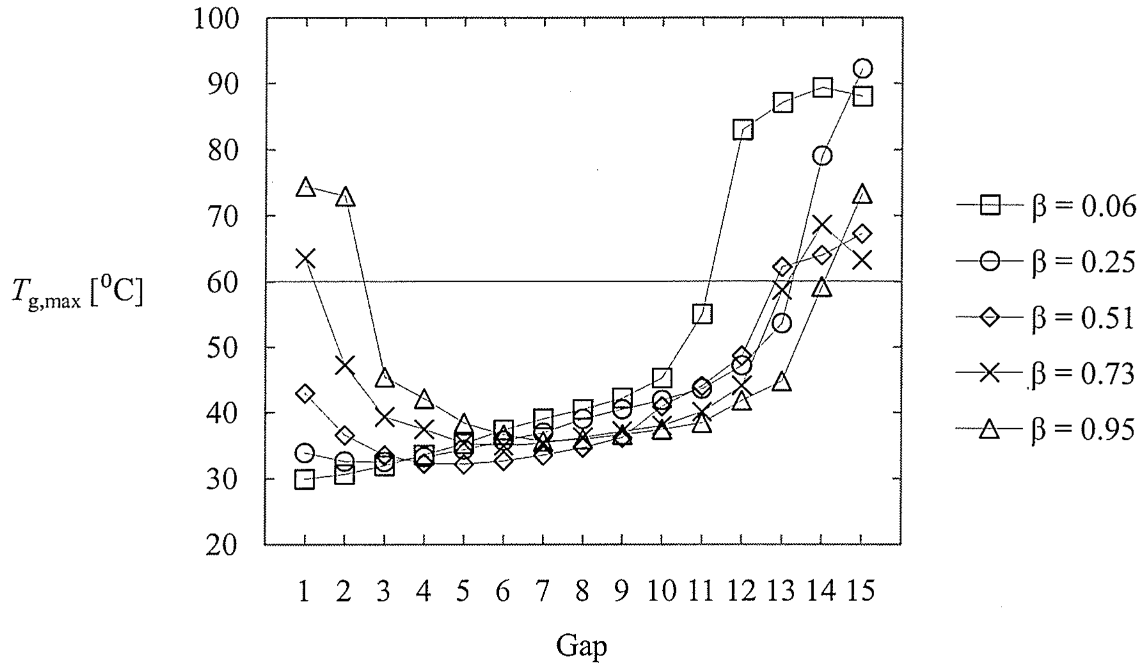

Figure 5-65: $T_{g,max}$ for all tower gaps (Cases 36, 38, 40, 42, and 44)

5.4.2.2: The Effect of β for the Low Tower, Cases 37, 39, 41, 43, and 45

The jet inlet angle for the low tower cases in this section ranged from 43.7° to 79.3°. The profiles for $\%\dot{m}_{g,net}$ and $T_{g,max}$ at all tower gaps for Cases 37, 39, 41, 43, and 45 are shown in Figures 5-66 and 5-67, respectively. When β is in the range of 0.06 to 0.25, airflow does not significantly penetrate the top three tower gaps. If β is in the range of 0.51 to 0.95, airflow does not significantly penetrate the bottom three tower gaps. There is no value of β where all of the tower gaps receive adequate airflow; this is similar to what was observed when the inlet was at the base location. When $\%\dot{m}_{g,net}$ is above 2, $T_{g,max}$ is reduced below 60°C.

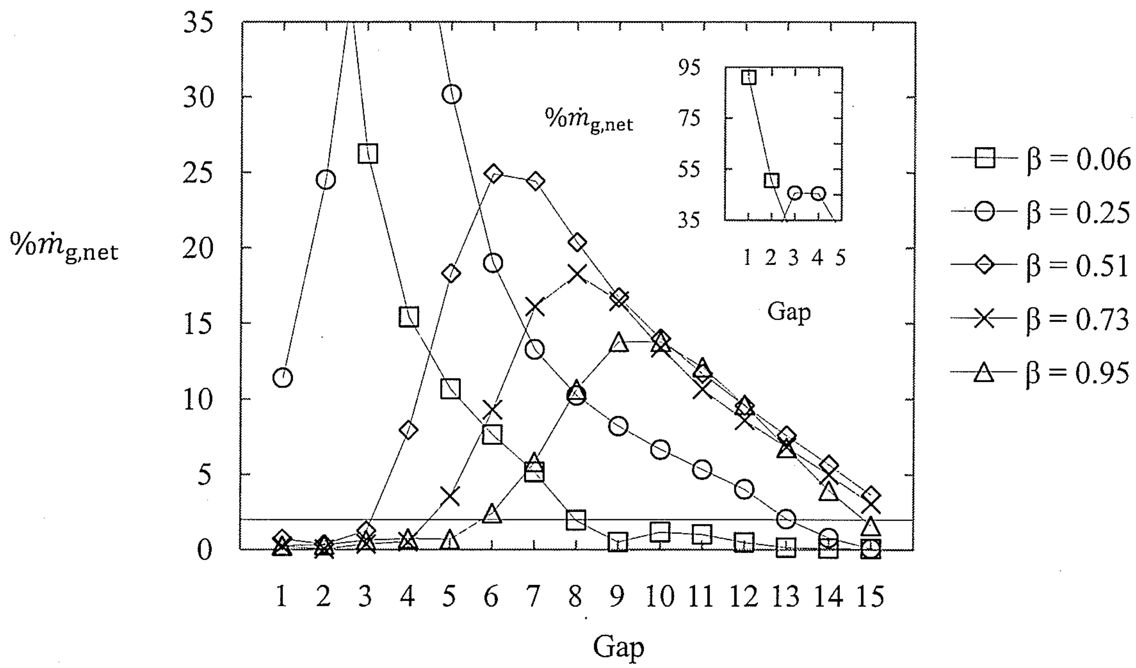

Figure 5-66: $\%\dot{m}_{g,net}$ for all tower gaps (Cases 37, 39, 41, 43, and 45)

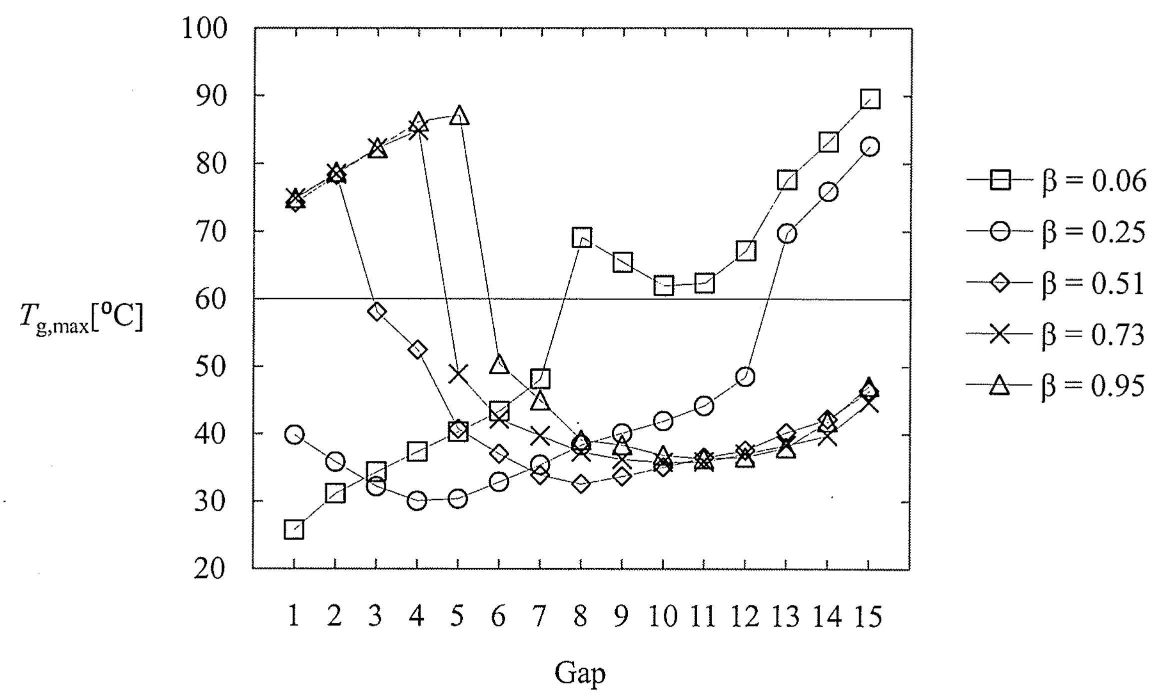

Figure 5-67: $T_{g,max}$ for all tower gaps (Cases 37, 39, 41, 43, and 45)

5.4.2.3: Summary of the Effect of Moving the Inlet Away from the Tower

A comparison of the effect of β on the high tower base inlet location (Cases 1, 5, 7, 9, and 11) and the high tower far inlet location (Cases 36, 38, 40, 42, and 44) is presented for $\sum\%\dot{m}_{g,net}$, $T_{t,av}$, and $T_{t,max}$ in Figures 5-68, 5-69, and 5-70, respectively. Moving the inlet away from the tower has a relatively small effect on $\sum\%\dot{m}_{g,net}$. The highest $\sum\%\dot{m}_{g,net}$ value for both inlet locations occurs at β = 0.25. For all values of β, $T_{t,av}$, and $T_{t,max}$ increase when the inlet is moved farther away. From the above discussion the following observation can be made for the high tower:

- There is no benefit in moving the inlet farther away from the tower when the tower is elevated high above the ground. Since θ is lower, the airflow is localized on the tower and there is more decay in the jet velocity since the inlet is farther from the tower.

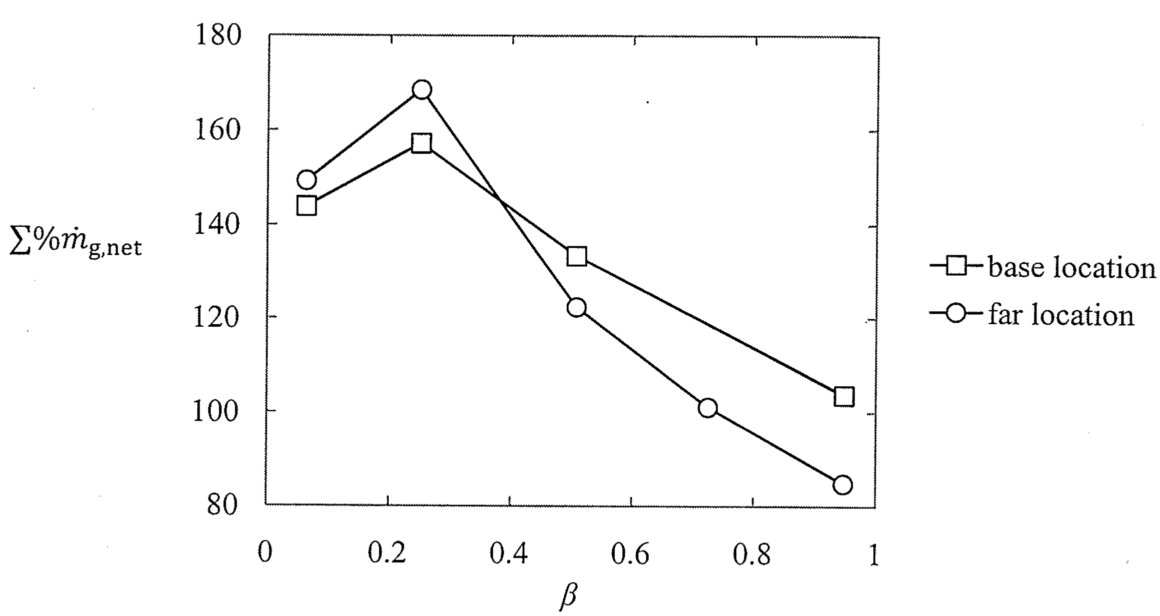

Figure 5-68: $\sum\%\dot{m}_{g,net}$ vs. β (Cases 1, 5, 7, 9, 11, 36, 38, 40, 42, and 44)

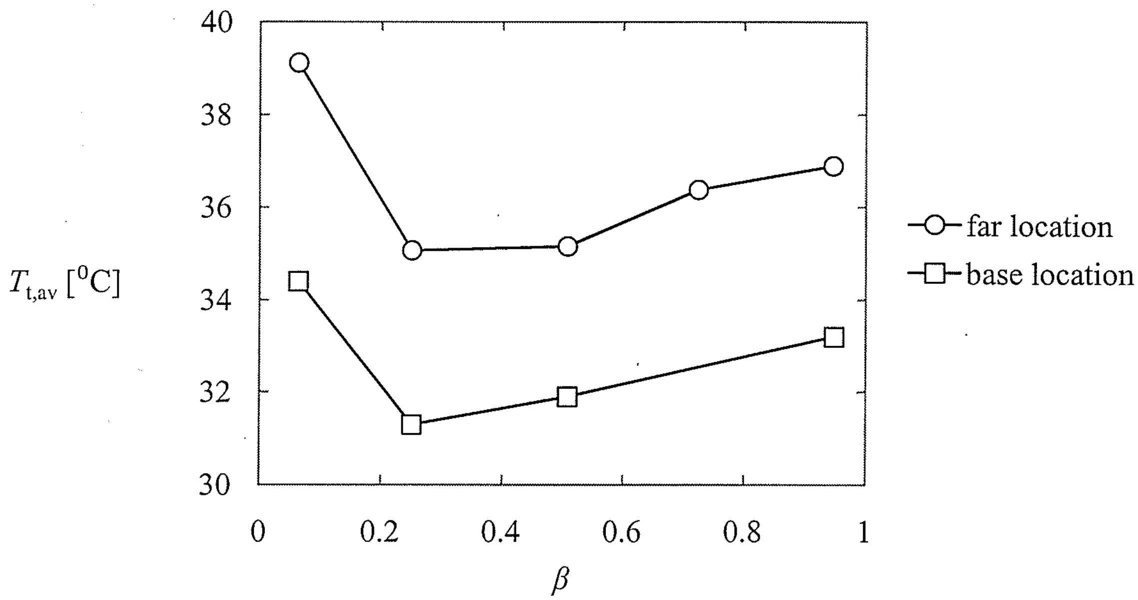

Figure 5-69: $T_{t,av}$ vs. β (Cases 1, 5, 7, 9, 11, 36, 38, 40, 42, and 44)

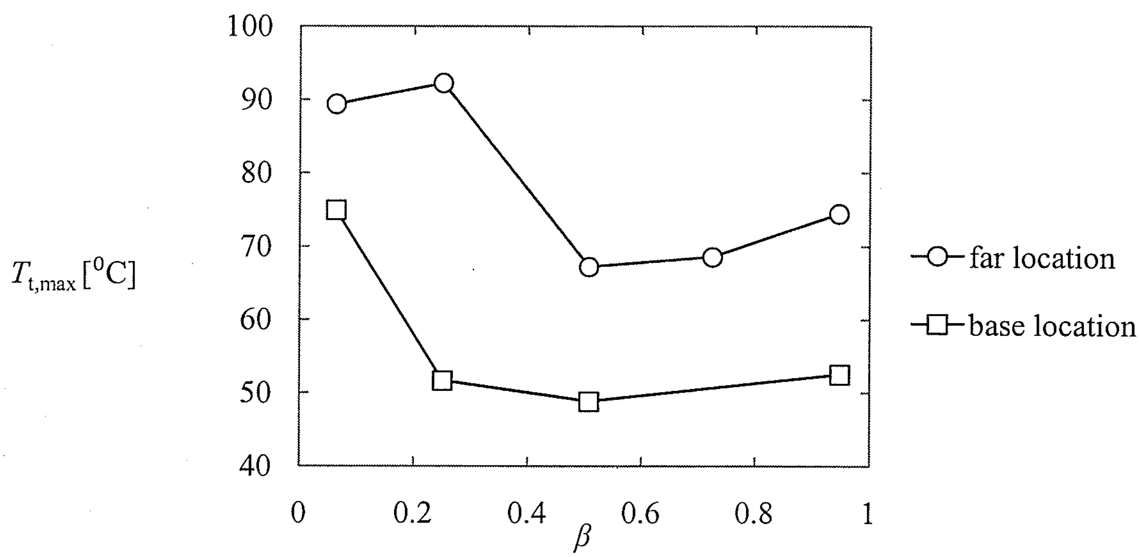

Figure 5-70: $T_{t,max}$ vs. β (Cases 1, 5, 7, 9, 11, 36, 38, 40, 42, and 44)

A comparison of the effect of β on the low tower base inlet location (Cases 2, 6, 8, 10, and 12) and the low tower far inlet location (Cases 39, 41, 43, 44, and 47) is presented for $\sum\%\dot{m}_{g,net}$, $T_{t,av}$, and $T_{t,max}$ in Figures 5-71, 5-72, and 5-73, respectively. Irrespective of the value of β, there is relatively little change in $\sum\%\dot{m}_{g,net}$ between the two inlet locations. The highest $\sum\%\dot{m}_{g,net}$ for both inlet locations occurs at $\beta = 0.25$.

Moving the inlet farther away from the tower slightly increases $T_{t,av}$ for all β values. The values of $T_{t,max}$ are slightly higher for the base inlet location for β in the range of 0.06 to 0.25; for β values in the range of 0.51 to 0.95, the base inlet location has slightly lower values for $T_{t,max}$. From the above discussion the following observation can be made for the low tower:

- Similar to the high tower cases, for the low tower there is no benefit to the ventilation system when the inlet is moved farther away from the tower.

The results from this section are summarized in Table 5-8.

Table 5-8: Summary of key results from Cases 36 to 45

Case	θ [deg]	β	Tower Type	$T_{t,max}$ [^oC]	No. of gaps with $T_{g,max}$ > 60 [^oC]	$T_{t,av}$ [^oC]	$\sum\%\dot{m}_{g,net}$
36	68.0	0.06	High Tower	89.4	4	39.1	149.3
38	73.6	0.25		92.2	2	35.1	168.5
40	77.9	0.51		67.2	3	35.2	122.4
42	80.1	0.73		68.6	3	36.4	101.1
44	81.6	0.95		74.5	3	36.9	84.8
37	43.7	0.06	Low Tower	89.6	8	42.9	212.0
39	62.0	0.25		82.5	2	35.3	226.8
41	72.3	0.51		78.3	2	35.0	167.1
43	76.6	0.73		84.8	4	39.1	112.3
45	79.3	0.95		87.1	5	41.1	83.2

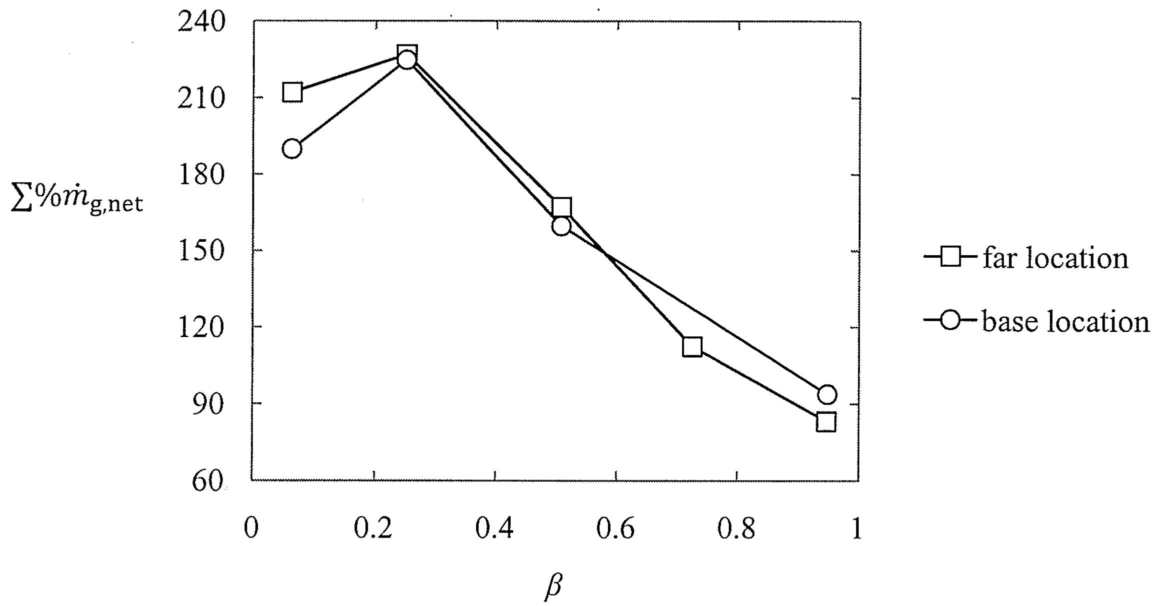

Figure 5-71: $\sum\%\dot{m}_{g,net}$ vs. β (Cases 2, 6, 8, 10, 12, 37, 39, 41, 43, and 45)

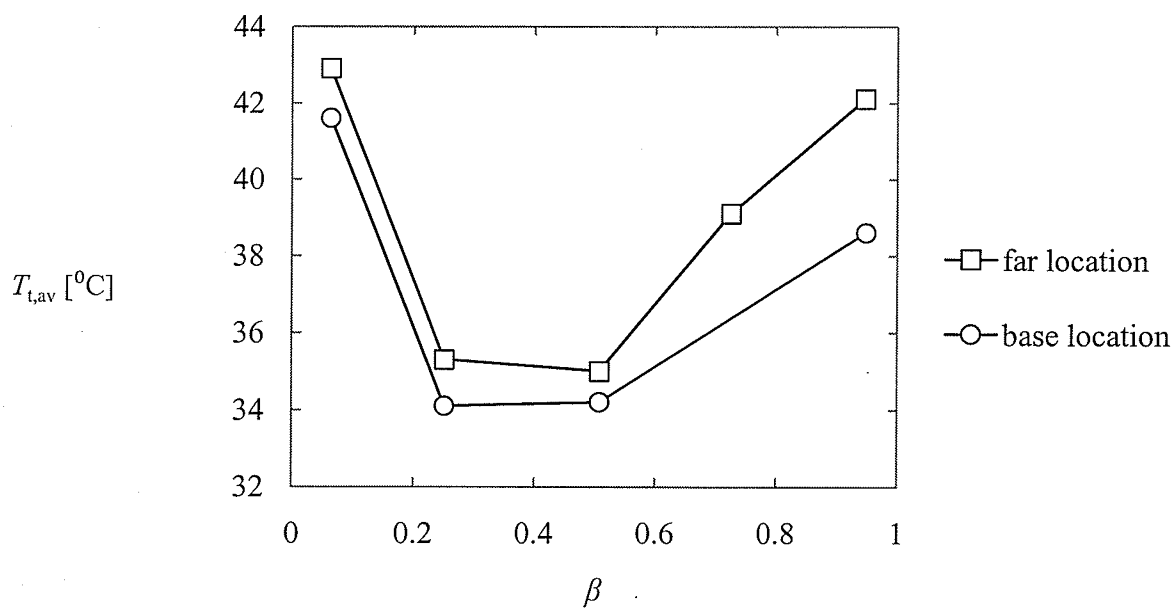

Figure 5-72: $T_{t,av}$ vs. β (Cases 2, 6, 8, 10, 12, 37, 39, 41, 43, and 45)

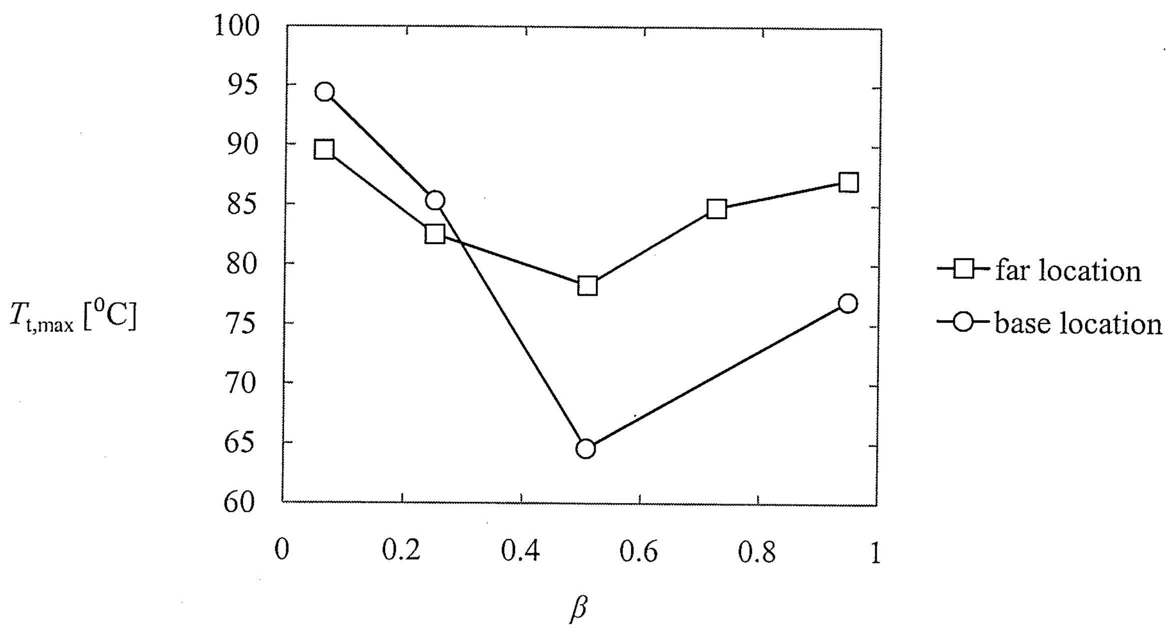

Figure 5-73: $T_{t,max}$ vs. β (Cases 2, 6, 8, 10, 12, 37, 39, 41, 43, and 45)

5.5: Correlation Between $T_{g,max}$ and $\%\dot{m}_{g,net}$

It has been observed that in many cases there is a notable pattern of dependence between $T_{g,max}$ and $\%\dot{m}_{g,net}$. For $\%\dot{m}_{g,net} < 2$, $T_{g,max}$ was above 60°C and had a weak dependence on $\%\dot{m}_{g,net}$. For $\%\dot{m}_{g,net} > 2$, $T_{g,max}$ was below 60°C in the vast majority of cases and there was a clear trend of decreasing $T_{g,max}$ with increasing $\%\dot{m}_{g,net}$. This trend is shown in Figure 5-74 with all data points for which $\%\dot{m}_{g,net} > 2$, corresponding to high and low towers, for all values of β, all inlet locations, and all inlet geometries.

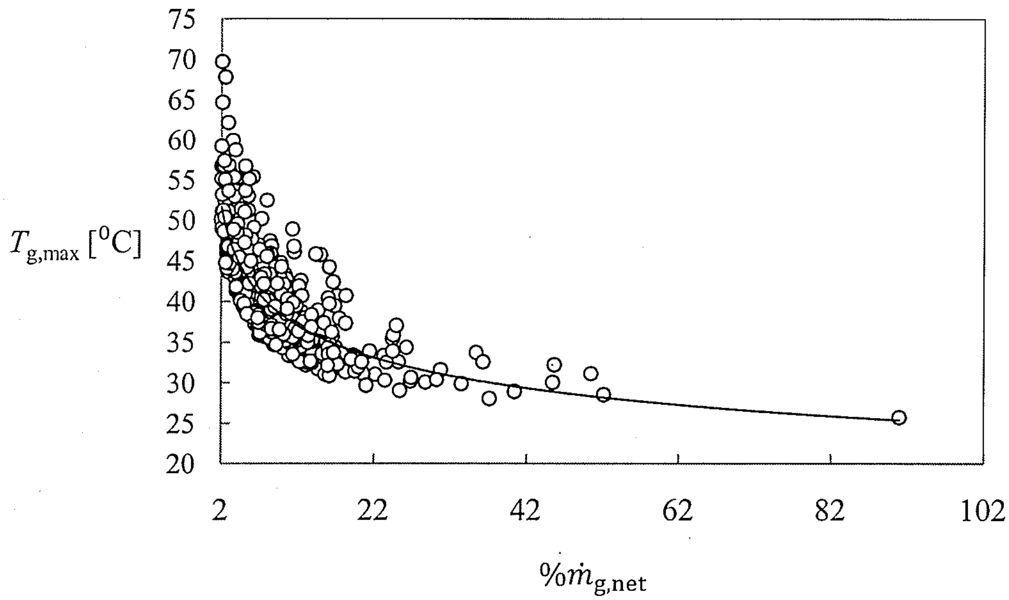

Figure 5-74: $T_{g,max}$ vs. $\%\dot{m}_{g,net}$ (all cases with $\%\dot{m}_{g,net} > 2$)

CHAPTER 6: CONCLUSIONS AND RECOMMENDATIONS

6.1: Conclusions

The ventilation cooling of DC/AC converter towers was numerically investigated in this thesis. The commercial CFD code, ANSYS CFX-11 was utilized to solve the governing equations. It was determined that the effectiveness of a ventilation design can be influenced by parameters, such as: the location of the inlet, inlet geometry, and the location on the tower that the jet is aimed at. The following conclusions can be drawn from the results of the present work:

- It was found that varying β can significantly affect the tower ventilation. The highest $\sum\%\dot{m}_{\mathrm{g,net}}$ occurred at $\beta = 0.25$ and changing β from this value reduced $\sum\%\dot{m}_{\mathrm{g,net}}$. This trend was valid for all cases tested. In a majority of the cases, it was found that the highest $\sum\%\dot{m}_{\mathrm{g,net}}$ value resulted in the lowest value for $T_{\mathrm{t,av}}$. When the inlet was shape 2 (0.5 size) and positioned at the base location, the lowest value for $T_{\mathrm{t,av}}$ occurred when $\beta = 0.51$. These trends were observed for both the high and low towers.

- The value of $\%\dot{m}_{\mathrm{g,net}}$ was found to affect the value of $T_{\mathrm{g,max}}$. For a significant majority of the cases simulated, when $\%\dot{m}_{\mathrm{g,net}}$ was above a threshold value of 2, $T_{\mathrm{g,max}}$ was reduced below 60°C. The streamlines entering a gap with a value of $\%\dot{m}_{\mathrm{g,net}}$ above 2 were found to completely penetrate the gap. When $\%\dot{m}_{\mathrm{g,net}}$ dropped below the threshold value of 2, $T_{\mathrm{g,max}}$ increased above 60°C. The streamlines entering a gap with a value of $\%\dot{m}_{\mathrm{g,net}}$ below 2 were found to only partially penetrate a gap. These trends were found to be valid for both the high and low towers.

- It was found that in general, reducing the size of the inlet increased $\sum\%\dot{m}_{\mathrm{g,net}}$ and reduced $T_{\mathrm{t,av}}$. When the inlet was reduced to half of the base inlet size, it was found that the inlet aspect ratio did not influence the ventilation. When the inlet size was further reduced to a quarter of the base size, it was determined that the inlet aspect ratio did affect the ventilation.

- When the base inlet conditions were simulated, it was found that for the high tower, irrespective of the value of β, Gaps 10 to 15 never received sufficient airflow. For the low tower, irrespective of the value of β, Gaps 12 to 15 never received sufficient airflow. These trends are the result of velocity decay in the jet. Since the low tower is closer to the ground, the jet experiences less velocity decay reaching the top tower gaps, relative to the high tower. It was found that for the high tower, the bottom tower gaps always received sufficient airflow from the jet. For the low tower, when the jet was aimed high the bottom gaps were missed by the jet.

- When the inlet was kept at the base location and its size was reduced to shape 2 (0.5 size), it was found that for the high tower, due to velocity decay in the jet, Gaps 13 to 15 never received sufficient airflow. For the low tower, the jet with inlet shape 2 can reach the top tower gaps. However, when the jet was aimed low the top gaps were missed and when the jet was aimed high, the bottom gaps were missed.

- When the inlet was kept at the base location and its size was further reduced to shape 3 (0.25 size), it was found that for the high tower, when β was at or above 0.25, all tower gaps received sufficient airflow. The same results could not be duplicated for the low tower. For the low tower, reducing the inlet size to shape 3 gave minimal improvement to the ventilation, relative to shape 2.

- For the low tower only, the inlet was moved closer to the tower and it was found that this improved the ventilation of the tower. At the close inlet location, it was found that shape 2 inlet (0.5 size) or shape 3 inlet (0.25 size) could sufficiently cool the entire tower. When the location of the inlet was moved away from the tower, it was found that this reduced the effectiveness of tower cooling for both the high and low towers.

6.2: Recommendations

In this section, recommendations will be made regarding modification to the air ventilation system in VH41 and VH42.

If no modifications are made to the size and location of the inlet, the following recommendation can be made regarding the angle of the inlet jet:

- For both valve halls, β should be set at 0.25. This corresponds to a θ of about 70° and 81° for VH41 and VH42, respectively. For both valve halls, Gaps 10 to 15 will receive insufficient airflow from the ventilation system and the temperatures within those gaps will be elevated. However, the aforementioned values of θ will be the best possible values for the current size and location of the inlets

If modifications are made to the size and location of the inlet, the following recommendations can be made:

- For VH41, the inlet should be moved closer to the tower (P_y = 2.39 [m]), the inlet size should be reduced to half of the base size (shape 2), and θ should be about 83°. This will result in all gaps receiving sufficient airflow, and $T_{g,max} \leq 60°C$ for all gaps.
- For VH42, the inlet should be kept at the base location, the inlet size should be reduced to quarter of the base size (shape 3), and θ should be about 81°. This will result in all gaps receiving sufficient airflow, and $T_{g,max} \leq 60°C$ for all gaps.

It is understood that the engineering implications (e.g. the power requirement of the ventilation system fan) of these recommendations will be taken into consideration.

REFERENCES

Arquis, E., Rady, M.A., and Nada, S.A., 2007, A numerical investigation and parametric study of cooling an array of multiple protruding heat sources by a laminar slot air jet, *International Journal of Heat and Fluid Flow*, vol. 28, pp. 787-805.

Berg, J.R., Soliman, H.M., and Ormiston, S.J., 2006, Prediction of the flow structure in a turbulent rectangular free jet, *International Communications in Heat and Mass Transfer,* vol. 53, pp. 249-272.

Berg, J.R., Soliman, H.M., and Ormiston, S.J., 2008a, Effective cooling of stacked heat-generating bodies in a large room: Comparison between floor and side-wall air injection, *International Journal of Thermal Science*, vol. 47, pp. 787-799.

Berg, J.R., Soliman, H.M., and Ormiston, S.J., 2008b, Turbulent mixed-convection cooling of stacked heat-generating bodies in a three-dimensional domain, *Numerical Heat Transfer Part A-Applications*, vol. 53, pp. 249-272.

Berg, J.R., 2006, Three- dimensional analysis of airflow and temperature in a thyristor valve hall, M.Sc. thesis, University of Manitoba, Canada.

Cheng, J. and Tsay, Y., 2009, Thermal interaction and chimney effects on natural convective cooling performance of heat generating blocks mounted on a board in a two-dimensional cabinet, *Numerical Heat Transfer, Part A-Applications*, vol. 55, pp. 866-879.

Chang-geng, L. and Jie-min, Z., 2007, Experimental and numerical simulation study of heat transfer due to confined impinging circular jet, *Chem. Eng. Technol.*, vol. 30, no. 10, pp. 1355-1361.

Desrayaud, G. and Fichera, A., 2003, On natural convective heat transfer in vertical channels with a single surface mounted heat-flux module, *Journal of Heat Transfer*, vol. 125, pp. 734-739.

Eiamsa-ard, S. and Promvonge, P., 2008, Numerical study on heat transfer of turbulent channel flow over periodic grooves, *International Communications in Heat and Mass Transfer*, vol. 35, pp. 844-852.

Elsaadawy, E., Mortazavi, H., and Hamed, M.S., Turbulent modeling of forced convection heat transfer in two-dimensional ribbed channels, *Journal of Electrical Packaging*, vol. 130, pp.1-17.

Grotjans, H. and Menter, F.R., 1998, Wall functions for general application CFD codes, in: *ECCOMAS 98 Proceedings of the Forth European Computational Fluid Dynamics Conference, Athens, Greece*, pp. 1112-1117.

Hofmann, H.M., Kaiser, R., Kind, M., and Martin, H., 2007, Calculations of steady and pulsating impinging jets-an assessment of 13 widely used turbulence models, *Numerical Heat Transfer, Part B-Fundamentals*, vol. 51, pp. 565-583.

Isman, M.K., Pulat, E., Etemoglu, A.B., and Can, M., 2008, Numerical investigation of turbulent impinging jet cooling of a constant heat flux surface, *Numerical Heat Transfer Part A-Applications*, vol. 54, pp. 1109-1132.

Koca, A., 2008, Numerical analysis of conjugate heat transfer in a partially open cavity with a vertical heat source, *International Communications in Heat and Mass Transfer*, vol. 35, pp. 1385-1395.

Launder, B.E. and Spalding, D.E., 1974, The numerical computation of turbulent flows, *Computational Methods in Applied Mechanics and Engineering*, vol. 3, pp. 269-289.

Lu, W.Z., Tam, C.M., Leung, A.Y.T., and Howarth, A.T., 2002, Numerical Investigation of Convection Heat Transfer in a Heated Room, *Numerical Heat Transfer Part A-Applications*, vol. 42, pp. 233-251.

Madhusudhana, G. and Narasimham, G.S.V.L., 2007, Laminar conjugate mixed convection in a vertical channel with heat generating components, *International Journal of Heat and Mass Transfer*, vol. 50, pp. 3561-3574.

Majumdar, P. and Deb, P., 2003, Computational analysis of turbulent fluid flow and heat transfer over an array of heated modules using turbulence models, *Numerical Heat Transfer Part A-Applications*, vol. 43, pp. 669-692.

Manitoba Hydro, 2002, Dorsey Converter Station, viewed 1 July 2009, http://www.hydro.mb.ca/our_facilities/cs_dorsey.pdf.

Merci, B., Vierendeel, J, Langhe, C.D., and Dick, E., 2002, Numerical simulation of heat transfer of turbulent impinging jets with two-equation turbulence models, *International Journal of Numerical Methods for Heat Transfer and Fluid Flow*, vol. 13, no. 1, pp. 110-132.

Muftuoglu, A. and Bilgen, E., Natural convection in an open square cavity with discrete heaters at their optimized positions, *International Journal of Thermal Sciences*, vol. 47, pp. 369-377.

Radhakrishnan, T.V., Verma, A.K., Balaji, C. and Venkateshan, S.P., 2007, An experimental and numerical investigation of mixed convection from a heat generating element in a ventilated cavity, *Experimental Thermal and Fluid Science*, vol. 32, pp. 502-520.

Ramezanpour, A., Mirzaee, I., Firth, D., and Shirvani, H., 2007, A numerical heat transfer study of slot jet impinging on an inclined plate, *International Journal of Numerical Methods for Heat and Fluid Flow*, vol. 17, no. 7, pp. 661-676.

Ramirez-Iraheta, O.A., Ormiston, and S.J., Soliman, H.M., 2006, Effective cooling of vertical heat-generating stacks in a cavity with openings, *Heat Mass Transfer*, vol. 42, pp. 398-410.

Ramirez-Iraheta, O.A., 2004, Passive and mixed-convection cooling of vertical stacks of heat-generating bodies in a square cavity with openings, M.Sc. thesis, University of Manitoba, Canada.

Wang, S.J. and Mujumdar, A.S., 2004, A comparative study of five low Reynolds number k-ε models for impingement heat transfer, *Applied Thermal Engineering*, vol. 25, pp. 31-44.

Yilmaz, T. and Fraser, S.M., 2007, Turbulent natural convection in a vertical parallel-plate channel with asymmetric heating, *International Journal of Heat and Mass Transfer*, vol. 50, pp. 2612-2623.

Zuckerman, N. and Lior, N., 2005, Impingement Heat Transfer: Correlations and Numerical Modeling, *Journal of Heat Transfer, Technology Review*, vol. 127, pp. 544-552.

APPENDIX A: COMPUTATIONAL MESHES

This appendix contains front, side, and bottom views of the inner and outer medium meshes used for the domains in VH41 and VH42.

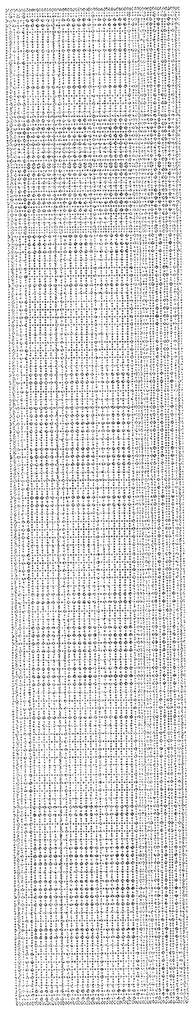

(c) Front view

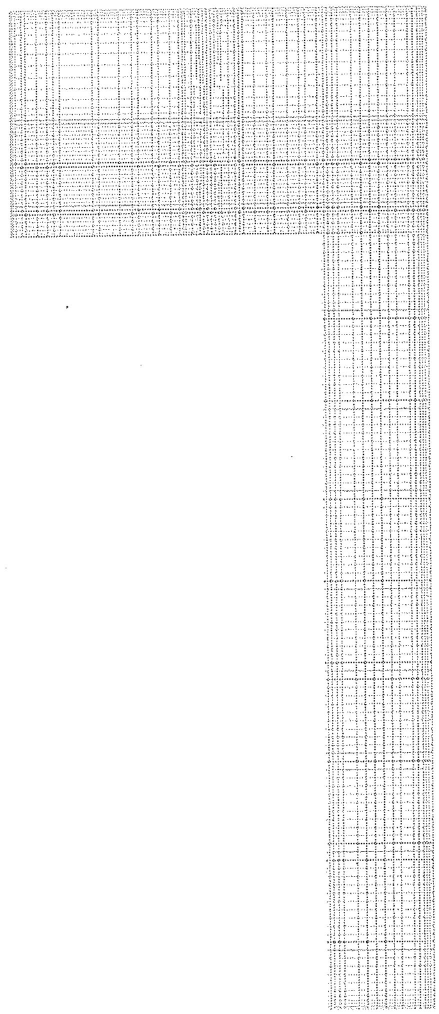

(b) Side view

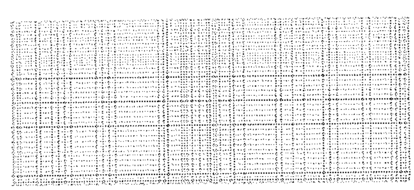

(a) Bottom view

Figure A-1: Medium outer mesh for VH41

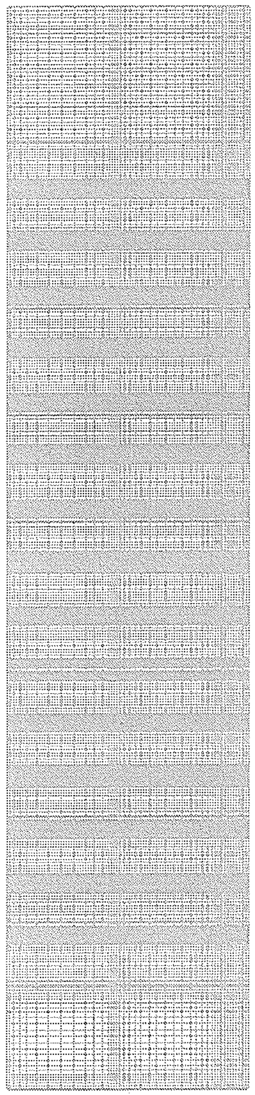

(a) Front view

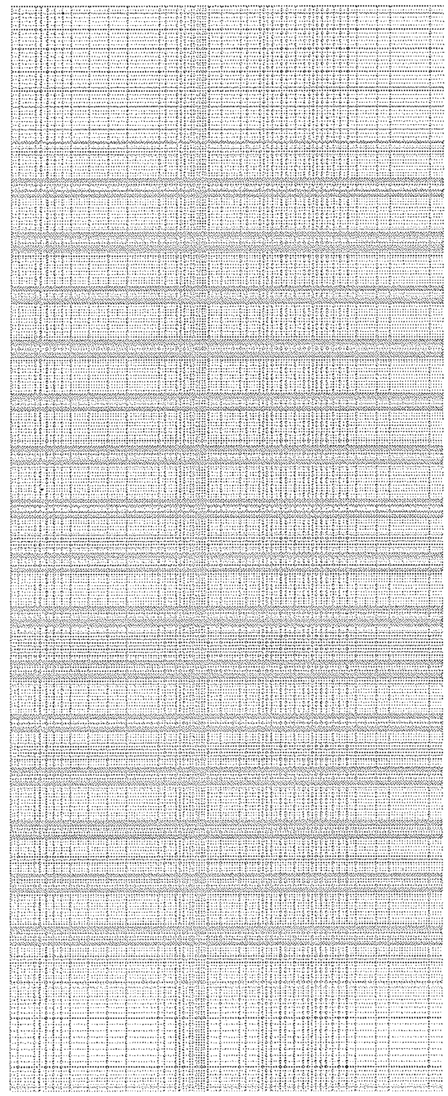

(b) Side view

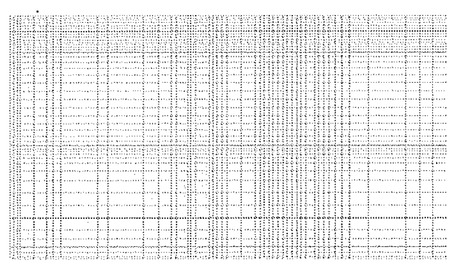

(c) Bottom view

Figure A-2: Medium inner mesh for VH41

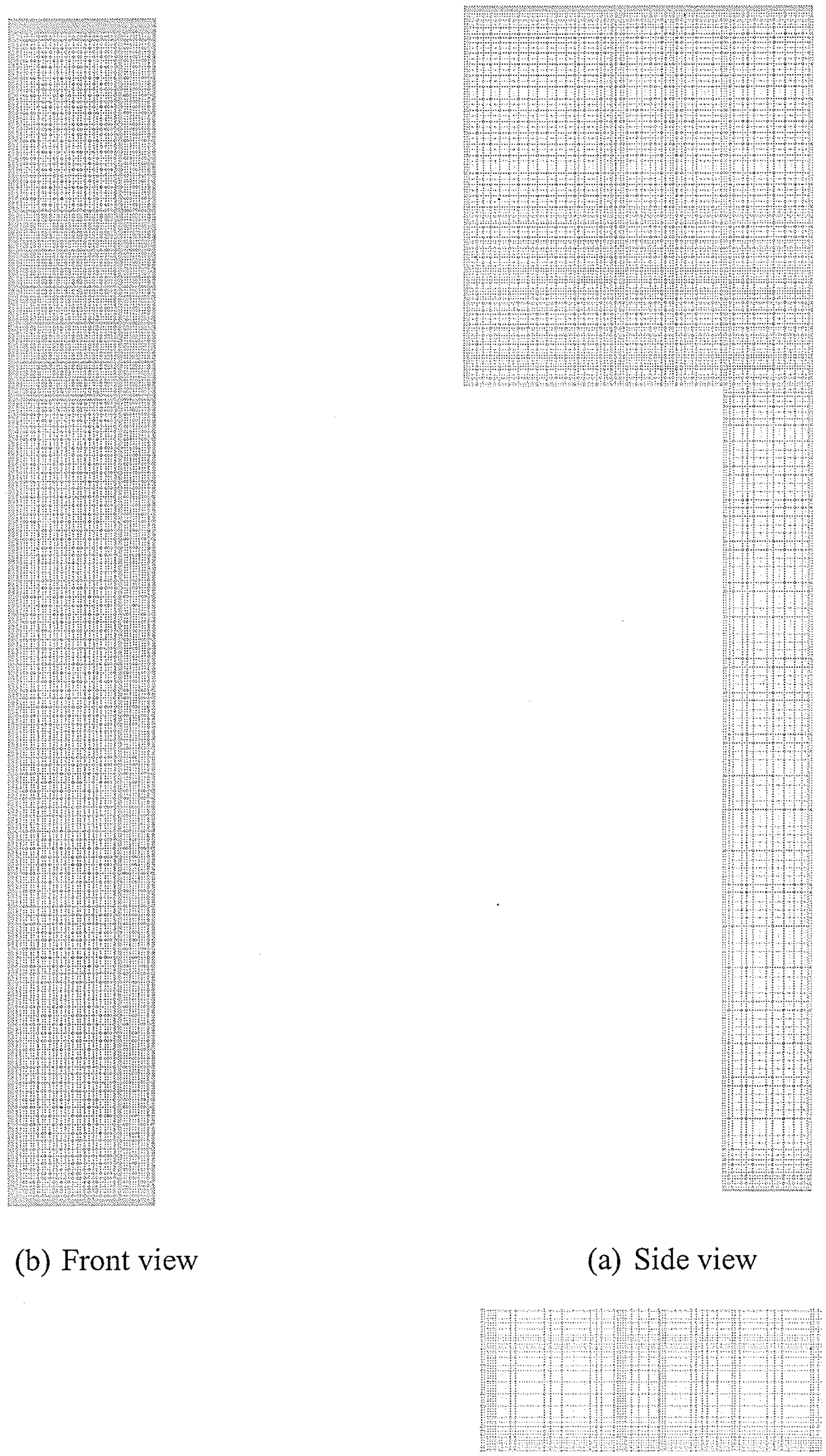

(b) Front view

(a) Side view

(c) Bottom view

Figure A-3: Medium outer mesh for VH42

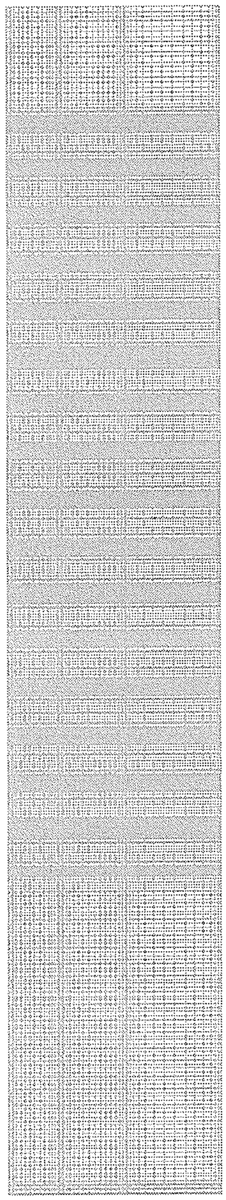

(c) Front view

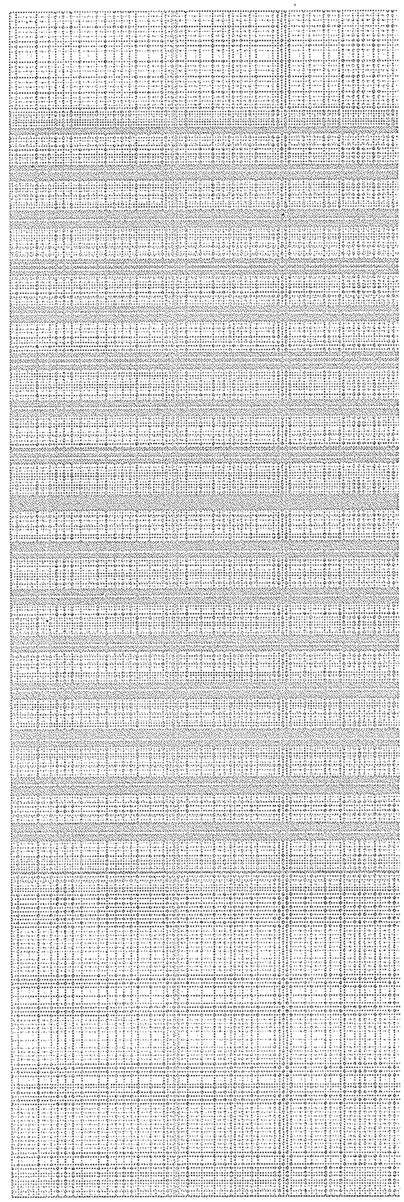

(a) Side view

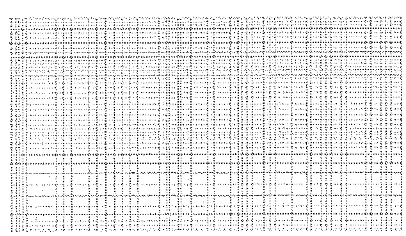

(b) Bottom view

Figure A-4: Medium inner mesh for VH42

APPENDIX B: CONVERGENCE OF A TYPICAL NUMERICAL RUN

This appendix shows the max residuals for mass, u, v, w, T, k, ε plotted against accumulated time step for Case 35.

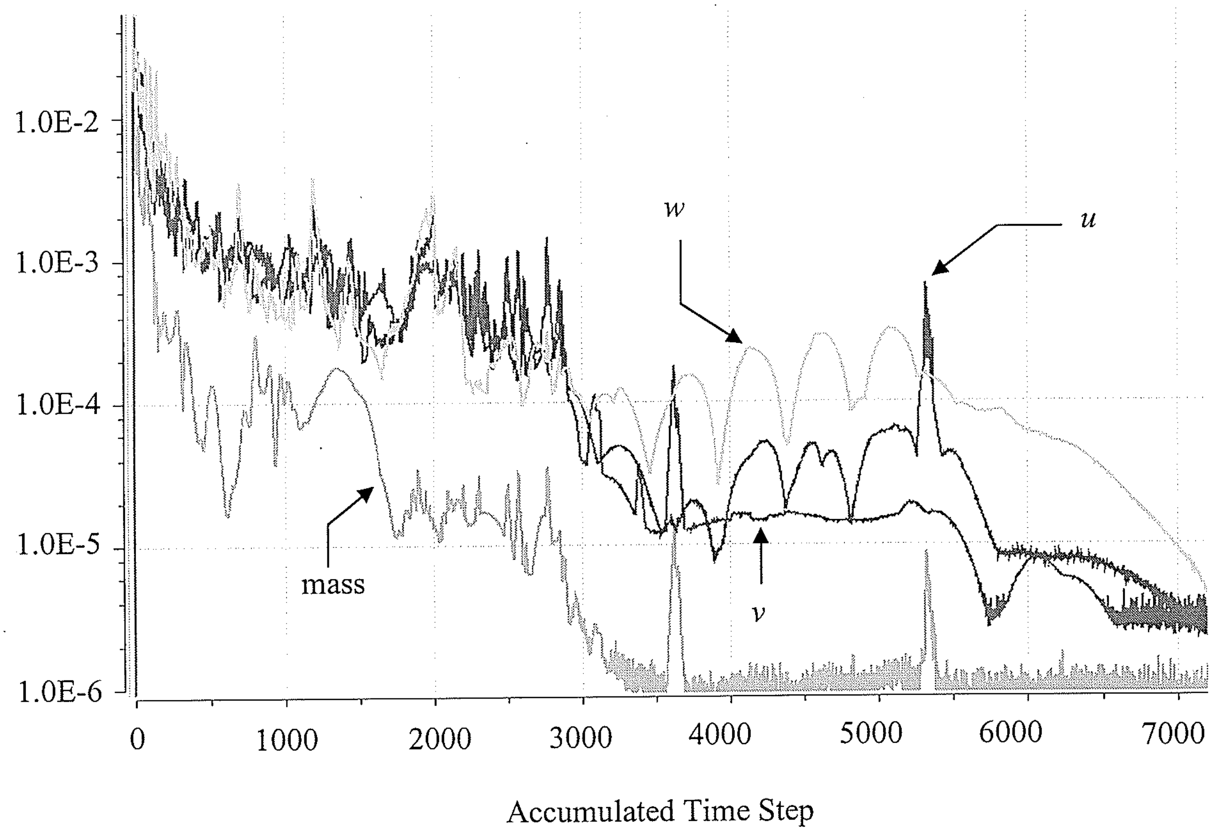

Figure B-1: Max residuals vs. accumulated time step for mass, u, v, and w for Case 35.

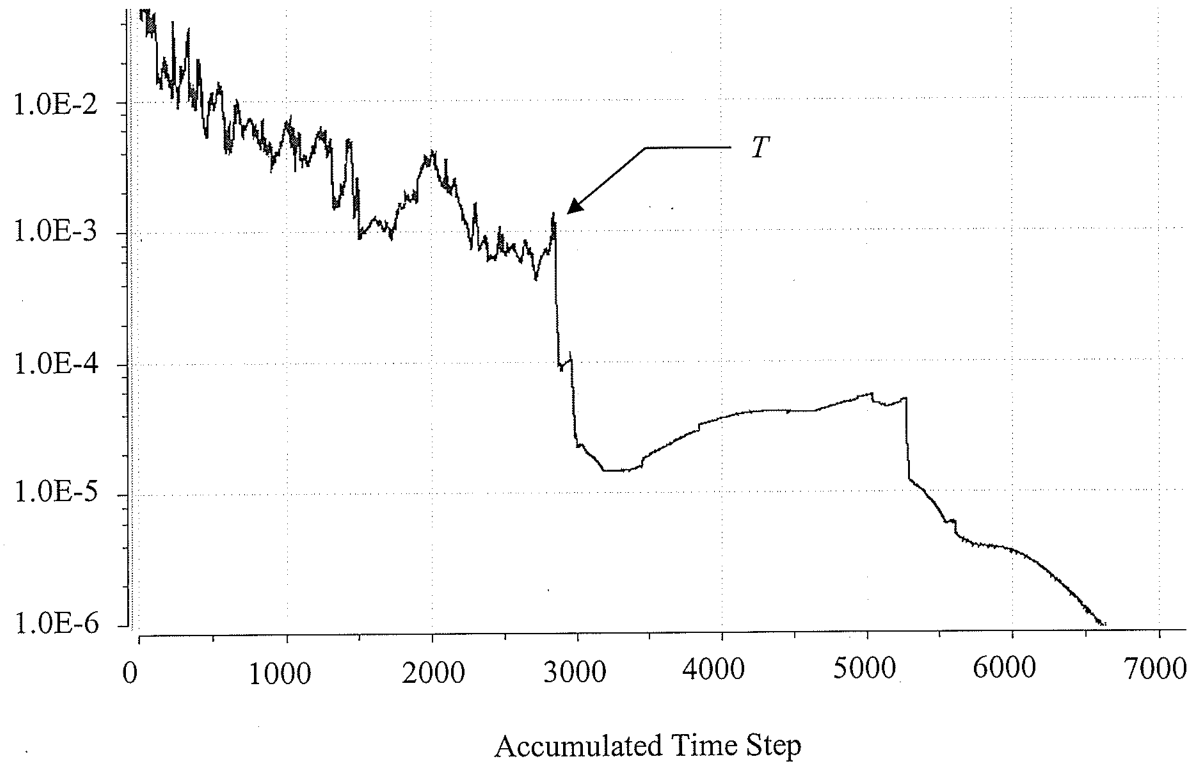

Figure B-2: Max residuals vs. accumulated time step for T for Case 35.

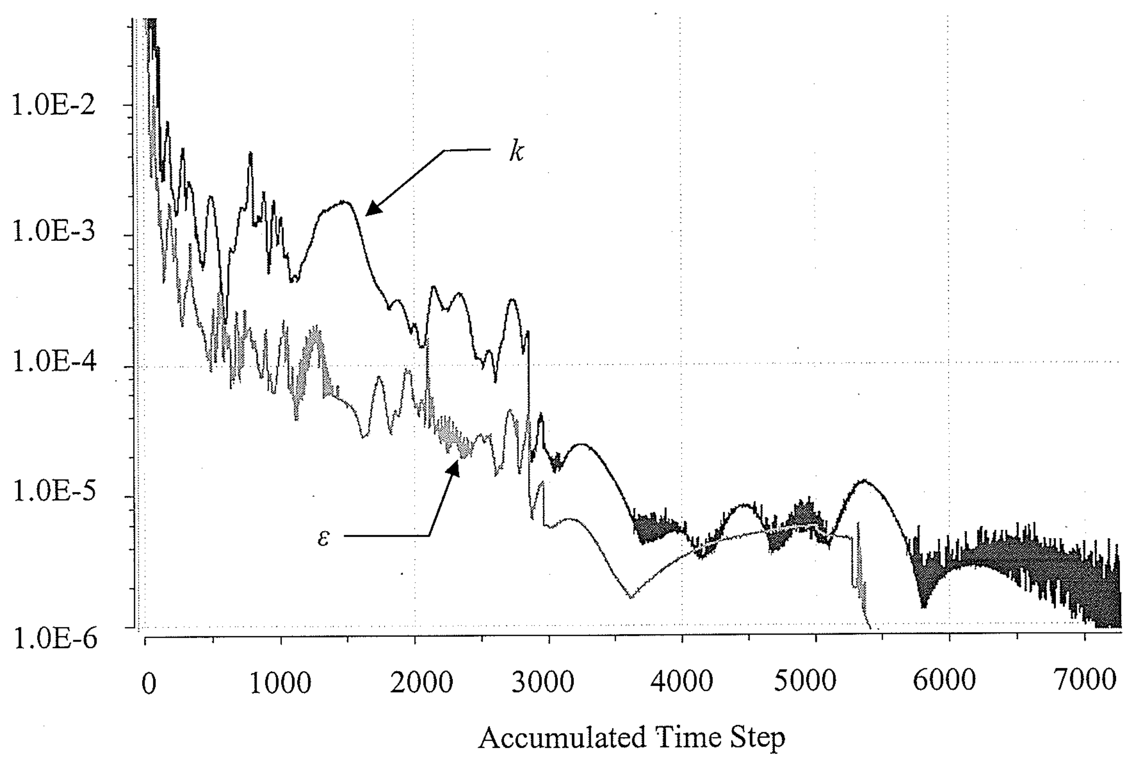

Figure B-3: Max residuals vs. accumulated time step for k and ε for Case 35.

APPENDIX C: EFFECT OF INLET SHAPE FOR A TOWER ELEVATION

This appendix contains plots of $\sum\%\dot{m}_{g,net}$, $T_{t,av}$, and $T_{t,max}$ vs. β for different inlet shapes. The results from the high a low towers are plotted on separate figures.

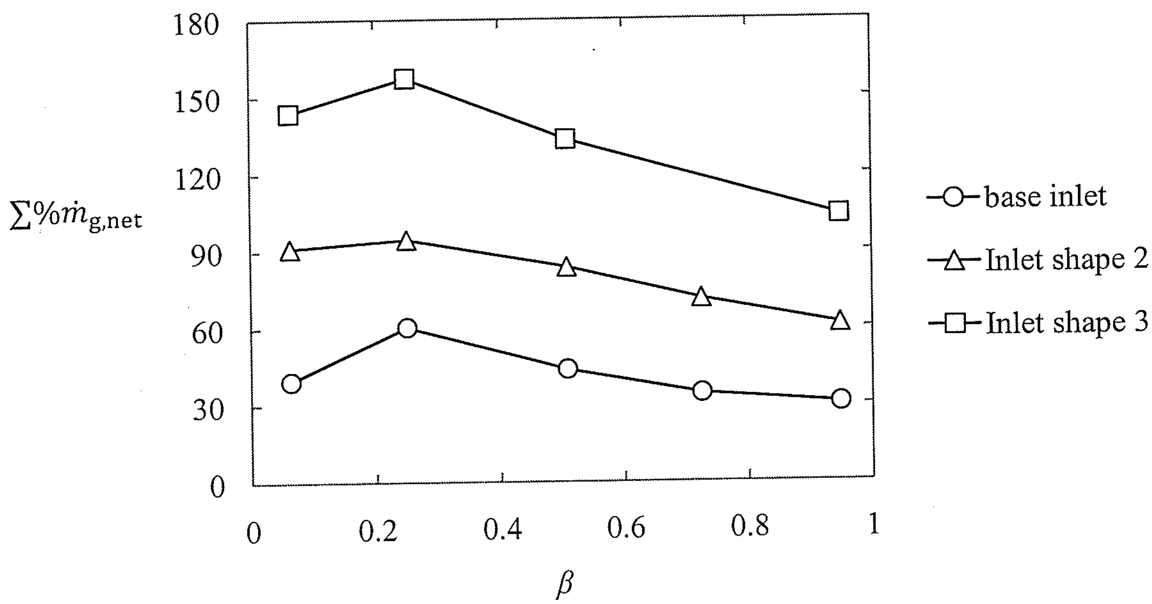

Figure C-1: $\sum\%\dot{m}_{g,net}$ vs. β for the high tower and different inlet shapes (Cases 1, 5, 7, 9, 11, 13, 15, 17, 19, 21, 23, 25, 27, and 29)

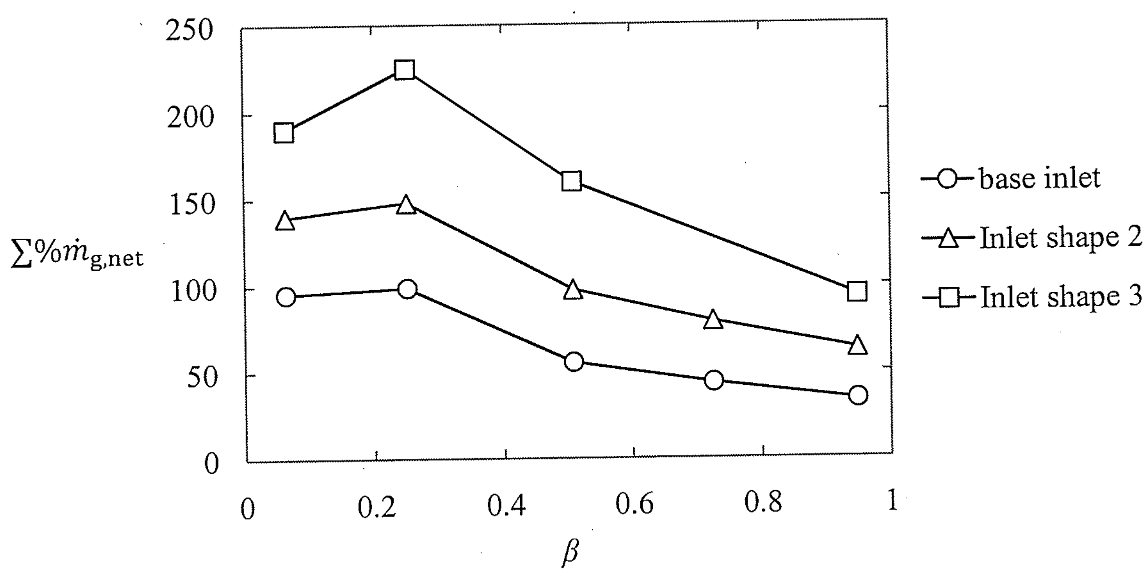

Figure C-2: $\sum\%\dot{m}_{g,net}$ vs. β for the low tower and different inlet shapes (Cases 2, 6, 8, 10, 12, 14, 16, 18, 20, 22, 24, 26, 28, and 30)

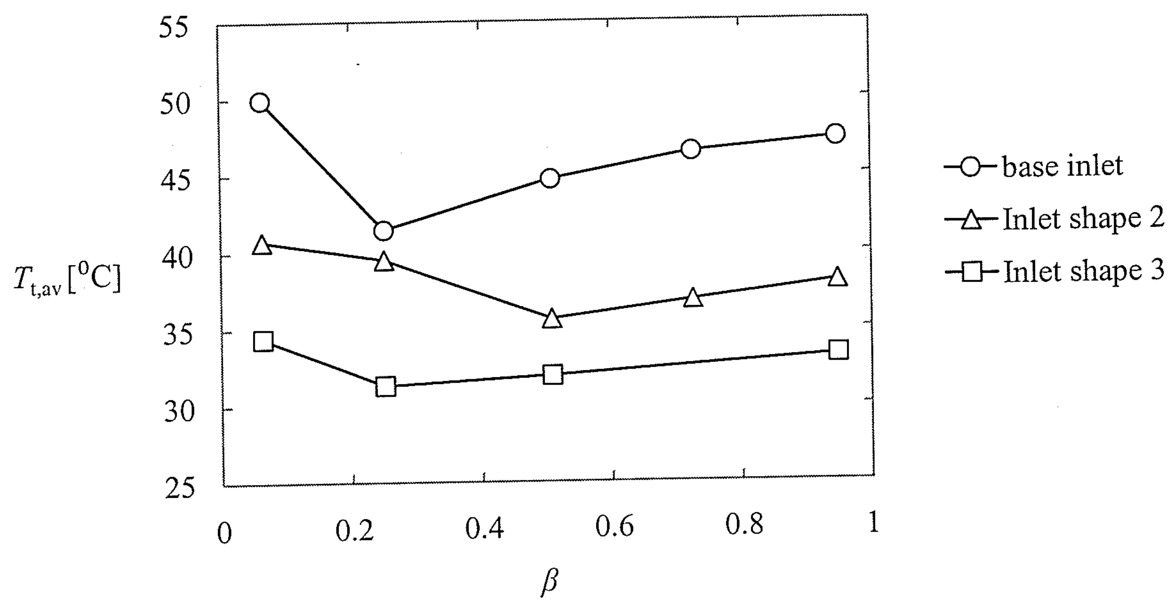

Figure C-3: $T_{t,av}$ vs. β for the high tower and different inlet shapes (Cases 1, 5, 7, 9, 11, 13, 15, 17, 19, 21, 23, 25, 27, and 29)

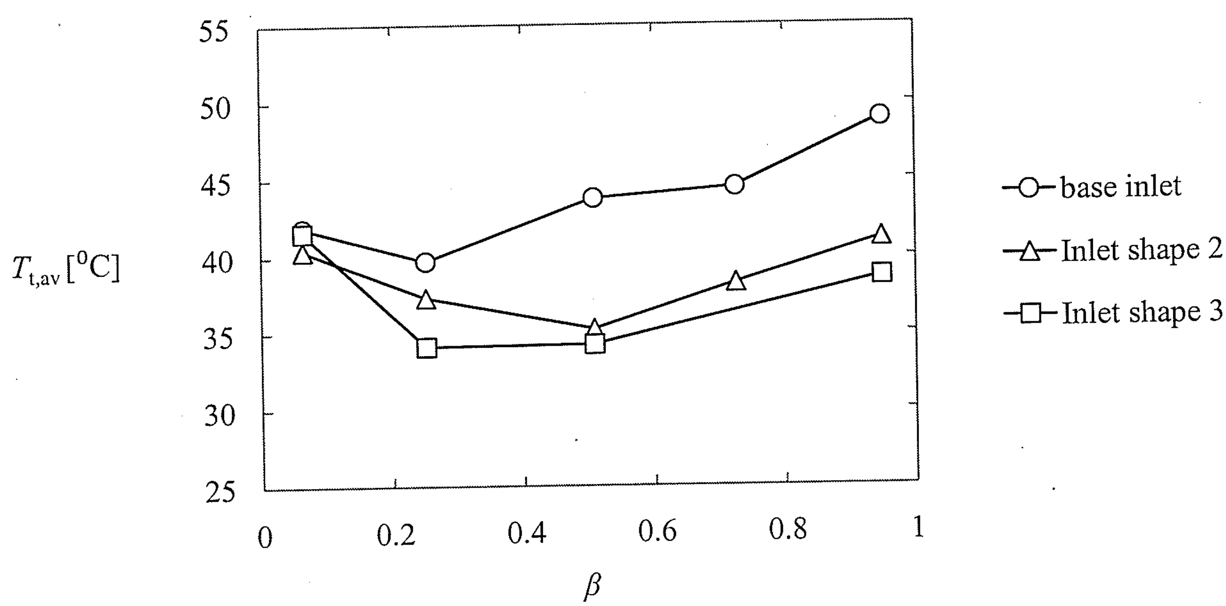

Figure C-4: $T_{t,av}$ vs. β for the low tower and different inlet shapes (Cases 2, 6, 8, 10, 12, 14, 16, 18, 20, 22, 24, 26, 28, and 30)

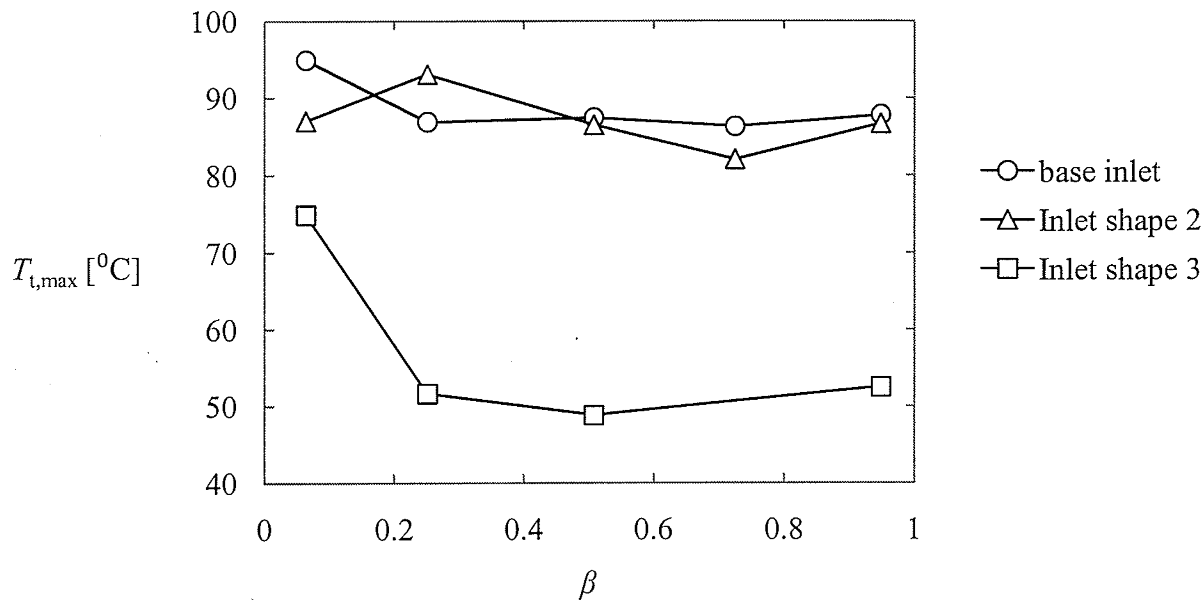

Figure C-5: $T_{t,max}$ vs. β for the high tower and different inlet shapes (Cases 1, 5, 7, 9, 11, 13, 15, 17, 19, 21, 23, 25, 27, and 29)

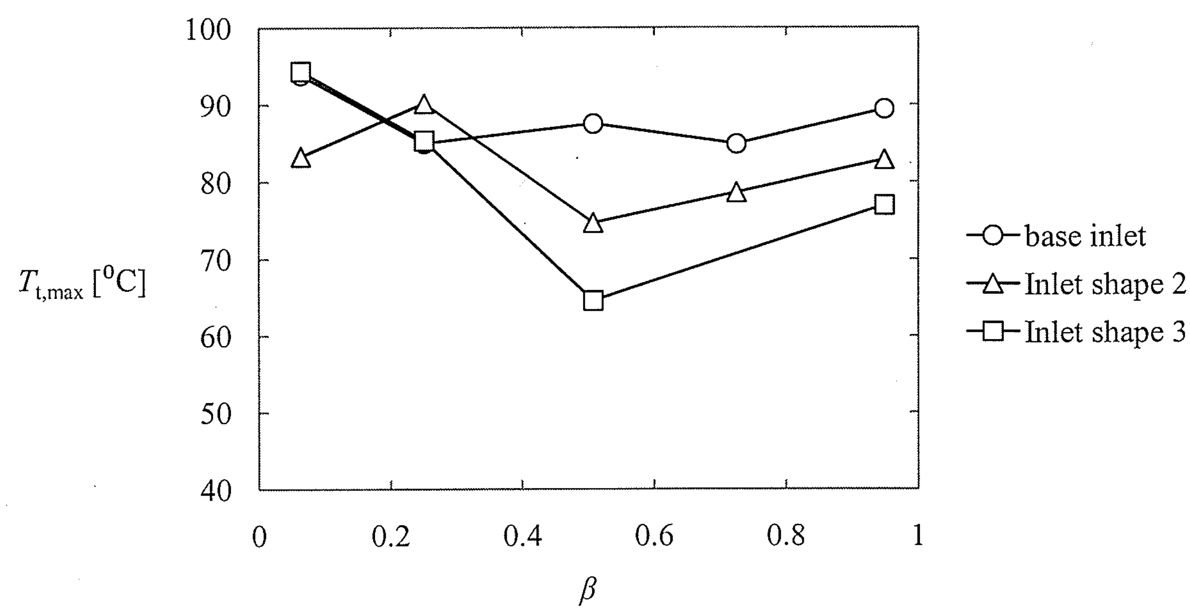

Figure C-6: $T_{t,max}$ vs. β for the low tower and different inlet shapes (Cases 2, 6, 8, 10, 12, 14, 16, 18, 20, 22, 24, 26, 28, and 30)